UNIVERSITY OF SALERNO

DEPARTMENT OF INDUSTIAL ENGINEERING

Ph. D. Thesis in Mechanical Engineering

XIV Cycle (2013-2015)

"TEST AND DEVELOPMENT OF A SOLAR-HYBRID VEHICLE PROTOTYPE AND TURBO-COMPRESSOR MODELS FOR AUTOMOTIVE ENGINES"

Ing. Massimo Naddeo

Supervisor

Ch.mo Prof. Gianfranco Rizzo

Coordinator

Ch.mo Prof. Vincenzo Sergi

Abstract

In last decade, Hybrid Electric Vehicles (HEV) have emerged as real alternatives to engine-driven vehicles, in order to reduce fuel consumption and emissions. However, their market share is still limited, as their impact on global fossil fuel demand and CO_2 production. In parallel, the possibility of upgrading conventional vehicles to HEV is gaining interest. A research work on the development of a kit for converting a conventional vehicle into a Through-The-Road (TTR) Hybrid Solar Vehicle (HSV), performed at the University of Salerno, is presented in this thesis. The prototype implementation through the installation of flexible solar cells, an additional Lithium-Ion battery and two electrically driven wheel-motors on a FIAT Grande Punto is described in detail. In the proposed vehicle, the control of in wheel motors is performed via a designed Vehicle Management Unit (VMU). In order to develop an effective and safe control strategy for in wheel-motors to be implemented on the VMU, a precise real-time knowledge of the Driver Intention is required. In particular, a set of mathematical models using data measured only by the OBD gate are developed (active gear detection, wheel torque estimation) and integrated into a fuzzy logic model. A study on the interaction between the driver and the modified vehicle system is carried out and used to evaluate the effects on drivability of the actuation chain delays due to the use of low frequency data and non-linear combination effect of different actuator interaction. The implemented control strategies are presented in terms of fuel and costs savings and, in particular, the management of regenerative braking is investigated to maximize its benefits and make the whole system work in safe conditions. Moreover, a methodology for predictive maintenance of vehicles based on telemetry technologies is defined in order to predict failure events and suggest the actions needed to avoid them for the user safety improvement., Finally, a study on turbo-compressor models is presented. Engine downsizing and super/turbocharging is currently, together with hybrid systems, the most followed trend in order to reduce CO_2 emissions and increase the powertrain efficiency. A key challenge for achieving the desired fuel economy benefits lies in optimizing the design and control of the engine boosting system, which requires the ability to rapidly sort different design options and technologies in simulation, evaluating their impact on engine performance and fuel consumption.

Abstract

Starting from the dimensional analysis theory for turbomachinery and a set of well-known control-oriented models for turbocharged engines simulation, a novel scalable model is proposed to predict the flow and efficiency maps of centrifugal compressors and radial inflow turbines as function of their key design parameters. The proposed approach is validated on a large database of compressors and turbines for automotive boosting applications, and examples are given to illustrate how the characteristic curves can be scaled with key design parameters.

Table of contents

Index of figures

X

Index of tables

CHAPTER 1

Introduction to hybrid vehicles

In a world where environment protection and energy saving are growing concerns, the development of electric vehicles (EV) and hybrid electric vehicles (HEV) has taken on an accelerated pace [1]. In particular, Hybrid Electric Vehicles (HEV) have emerged as one of the most effective and feasible alternatives to engine-driven vehicles, allowing significant reductions in fuel consumption and emissions [2]. Reducing greenhouse gas emissions from motor vehicles is a major challenge for climate policy, due to the significant fraction of total greenhouse gas (GHG) produced by the transportation sector [3] (Figure 1.1).

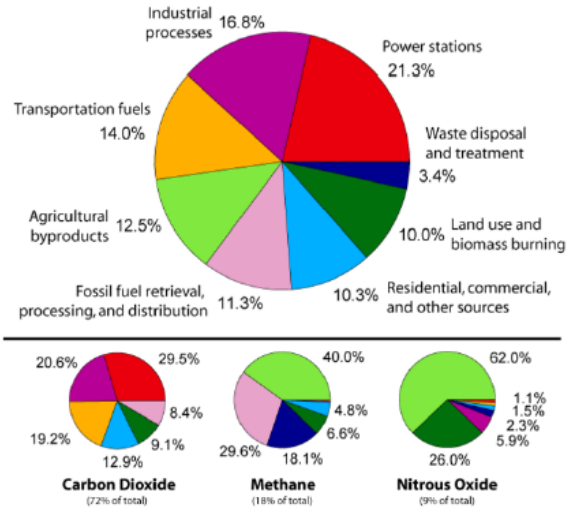

Figure 1.1- Annual Greenhouse Gas Emissions by sector

EU legislation adopted in 2009 mandatory emission reduction targets for new cars: the fleet average to be achieved by all new cars was 130 grams of CO2 per kilometer (g/km) by 2015 – with the target phased in from 2012 - and 95 g/km by 2020. The 2015 and 2020 targets represent reductions of 18% and 40% respectively compared with the 2007 fleet average of 158.7g/km [4]. Emission limits are set according to the mass of vehicle,

using a limit value curve. The curve is set in such a way that a fleet average of 130 grams of CO_2 per kilometer is achieved by 2015. The limit value curve means that heavier cars are allowed higher emissions than lighter cars while preserving the overall fleet average, thus vehicles with emissions above the limit value curve are still allowed, provided these are balanced by vehicles below the curve [4].

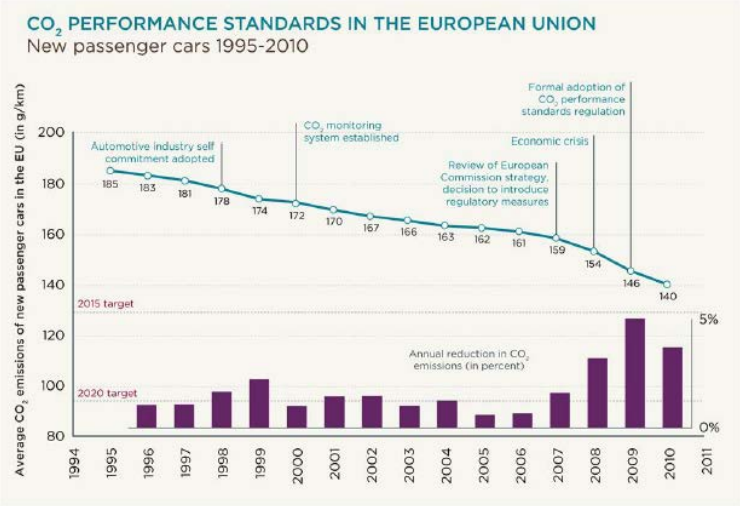

Figure 1.2 - CO_2 performance standards in European Union (1995-2011)

The EU fleet average target of 130g CO_2 per km has been phased in between 2012 and 2015. In 2012, an average of 65% of each manufacturers newly registered cars had to comply with the limit value curve set by the legislation. This raised to 75% in 2013, 80% in 2014, and 100% from 2015 onwards. Such regulations do not involve only environmental effects, but also come with significant direct economic impact for the automotive industry. In fact, if the average CO_2 emissions of a manufacturer fleet exceed its limit value in any year from 2012, the manufacturer has to pay an excess emissions premium for each car registered. This premium amounts to €5 for the first g/km above the limit, €15 for the second g/km, €25 for the third g/km, and €95 for each subsequent g/km. From 2019, the cost will be €95 from the first gram of exceedance onwards. Because of these reasons, HEVs market is slowly growing year by year.

1.1 Hybrid vehicles features

Hybrid-electric vehicles (HEVs) combine the benefits of gasoline engines and electric motors and can be configured to obtain different objectives, such as improved fuel economy, increased power, or additional auxiliary power for electronic devices and power tools. The electric energy storage system is usually an electrochemical battery, though supercapacitors may be used in some prototypes. One of the main motivations for developing HEVs is the possibility to combine the advantages of the purely electric vehicles, in particular zero local emissions, with the advantages of the ICE-based vehicles, namely high energy and power density. HEVs can profit from various possibilities for improving the fuel economy with respect to ICE-based vehicles.

Some of the advanced technologies typically used by hybrids include:

- **Regenerative Braking**: The electric motor applies resistance to the drivetrain causing the wheels to slow down. In return, the energy from the wheels turns the motor, which functions as a generator, converting energy normally wasted during coasting and braking into electricity, which is stored in a battery until needed by the electric motor.
- **Electric Motor Drive/Assist**: The electric motor provides additional power to assist the engine in accelerating, passing, or hill climbing. This allows a smaller, more efficient engine to be used. In some vehicles, the motor alone provides power for low-speed driving conditions where internal combustion engines are least efficient.
- **Automatic Start/Shutoff**: Automatically shuts off the engine when the vehicle comes to a stop and restarts it when the accelerator is pressed. This prevents wasted energy from idling.

These possible improvements are partially counteracted by the fact that HEVs are about 10–30% heavier than ICE-based vehicles.

1.2 HEVs background

The first hybrid electric vehicle dates back to 1899, developed by Ferdinand Porsche. The Lohner-Porsche Mixte used a gasoline engine to supply power to an electric motor that drove the car's front wheels.

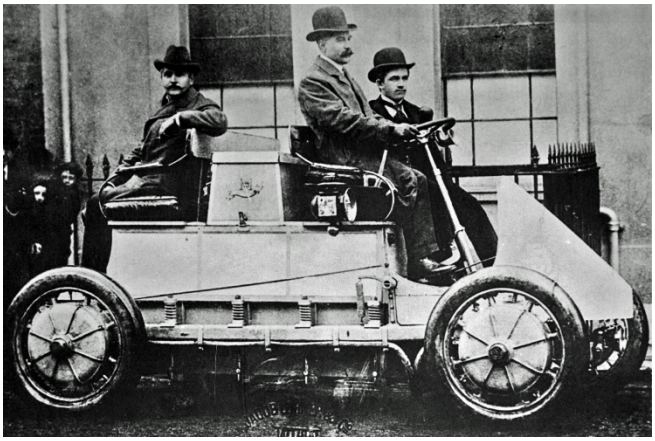

Figure 1.3 - First hybrid car by Ferdinand Porsche

The motivation for the development of an HEV was to overcome the limited range and the long recharge time of a pure electric vehicle [5]. Despite this early development, HEVs disappeared due to poor battery technology, cheap fuel and Ford's ability to produce gasoline-powered cars offering them at low prices. Moreover, significant improvement in the fuel economy of conventional powertrain was achieved by reducing vehicle weight, and improving the engine efficiency through controlling fueling, ignition and valve timing, etc. Hybrids soon became outdated, beginning a nearly 50-year period where they were merely an afterthought. In the 1960s, the United States congress introduced legislation that encouraged greater use of electric vehicles in an attempt to reduce air pollution and in order to further improve the energy efficiency of vehicle, researchers started look back to early HEVs for potential improvement. This renewed interest to HEVs gained momentum because of fuel price rising in the 1970s leading auto manufacturers to spent billions of dollars on research and development of hybrid technologies. A number of prototype hybrid test vehicles were built to experimentally validate the potentials of hybrid

powertrain. The hybrid test vehicle, ‘Mule’, from the California Institute of Technology [6], was built to meet the contemporary conventional vehicle standards in its performance, ergonomics and emission. Outstanding technical improvements were in the smooth power blending between two energy sources, turning engine on and off, and fuel savings that contributed to wards the hybrid technology advancement. In the late 1990s, a handful of all-electric vehicles were introduced, the GM EV1 and Toyota RAV-4 EV being two examples. These all-electric vehicles failed to attract widespread interest, and were soon dropped from production. In 1997, Toyota released the Prius in Japan as a viable alternative to gas powered vehicles. In the years since its United States introduction, the Prius has become synonymous with the term "hybrid." It is the most popular HEV ever produced, and auto manufacturers around the world have used its technology as a basis for countless other vehicles.

Figure 1.4 - First version of Toyota Prius released in 1997

More recently, research is being conducted on new potential combinations such as the pneumatic hybrid (compressed air & gasoline) [7] and solar hybrid [8], while, on the other hand, manufacturers like Honda released the Insight second-generation, and Chevrolet introduced the Volt. As discussed, increasing popularity and potential improvement indicate the promising future of hybrid vehicles, which warrant further research and development.

1.3 System configurations

Hybrid-electric vehicles are classified into two main types:

- **Parallel hybrid**: Both prime movers operate on the same drive shaft, thus they can power the vehicle individually or simultaneously.
- **Series hybrid**: The electric motor alone drives the vehicle. The electricity can be supplied either by a battery or by an engine-driven generator.

Additionally, certain new concepts have been introduced that cannot be adequately classified into any of the two basic types as Through The Road hybrid vehicles, for instance.

1.3.1. Series HEVs

Series hybrid propulsion systems utilize the internal combustion engine as an auxiliary power unit (APU) to extend the driving range of a purely electric vehicle. Using a generator, the engine output is converted into electricity that can either directly feed the motor or charge the battery (Figure 1.5). Regenerative braking is possible using the traction motor as a generator and storing the electricity in the battery. The engine operation is not related to the power requirements of the vehicle, thus the engine can be operated at a point with optimal efficiency and emissions. An added advantage may be the fact that the transmission does not require a clutch, i.e., the engine is never disengaged since it is mechanically decoupled from the drive axle. However, a series hybrid configuration needs three machines: one engine, one electric generator, and one electric traction motor. At least the traction motor has to be sized for the maximum power requirements of the vehicle. Thus, a series hybrid in principle offers the possibilities of reducing fuel consumption following the approach [9]. The overall tank-to-wheel efficiency for series hybrid vehicles is on a par with the values of vehicles powered by modern, fuel-efficient IC engines. The additional weight due to car body reinforcement, electric machines, battery, etc. may push the fuel consumption above the value of good ICE-based vehicles, however.

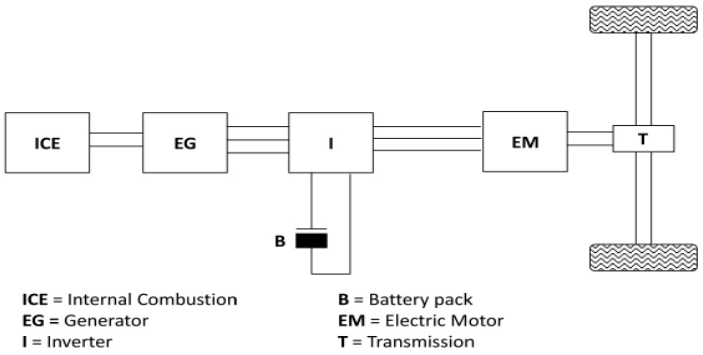

Figure 1.5 - Basic series hybrid configuration

1.3.2. Parallel HEVs

While series hybrid vehicles may be considered as purely electric vehicles with an additional ICE-based energy path, parallel hybrid vehicles are rather ICE-based vehicles with an additional electrical path (Figure 1.6). In parallel HEVs both the engine and the electric motor can supply the traction power either alone or in combination. This leaves an additional degree of freedom in fulfilling the power requirements of the vehicle, which can be used to optimize the power distribution between the two parallel paths. Typically, the engine can be turned off at idle [9] and the electric motor can be used to assist accelerations and, in general, high power demands. Both machines can therefore be sized for a fraction of the maximum power. Together with the fact that only two machines are needed, this is an advantage with respect to series hybrid vehicles. A disadvantage is the need for a clutch, since the engine is mechanically linked to the drive train. The electric motor can be utilized as a generator to charge the battery, being fed by regenerative braking or by the engine. Even though the additional weight still plays an important role, the system efficiency is increased if compared to an ICE-Based vehicle. Parallel hybrids are further classified according to the position of the electric machine with respect to the conventional drive train. In micro hybrids, the electric machine is typically belt-driven and mounted on the front of the engine, thus its speed is always rigidly linked to that of the engine. In pre-transmission parallel hybrids the electric machine is mounted between the engine and the gearbox. Again, the two speed levels are linked, thus this configuration is also called single-shaft. Depending on the number and the position of the clutches, various

functionalities can be achieved or not. In post-transmission or double-shaft parallel hybrids the electric machine is mounted downstream of the gearbox, thus the two speed levels are decoupled.

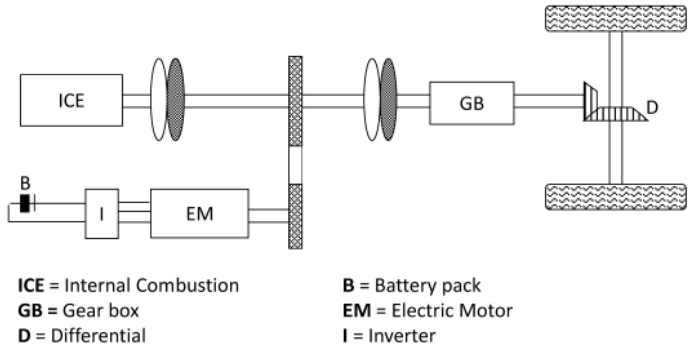

Figure 1.6 - Basic Parallel hybrid configuration

1.4 Solar hybrid vehicles

In recent times, a growing interest is deserved to solar hybrid vehicle because of the great amount of energy available from the sun. In principle, this kind of vehicles could have the same configuration of Parallel or Series hybrids integrating photovoltaic panels to charge traction battery or supply energy to vehicle auxiliary systems. The first solar car prototypes appeared in the '80s. They were single-seat vehicles, very light (the outer casing was made with special plastics able to guarantee the lightness of the structure without compromising strength) and extremely aerodynamic in order to reduce the air resistance. The entire outer surface was flat and covered by high-efficiency solar panels and their design was not very appealing. Anyway, powering a car with only solar energy is not a realistic solution because of limits in terms of power, size, cost and, above all, because of the total dependence on solar radiation: PV panels must always be exposed to sunshine and when it doesn’t happen the vehicle can be powered only by its battery with a limited autonomy. The most reasonable solution is than constituted by solar hybrid vehicles where PV panels operate as described above. Anyway, given the low efficiency of solar energy conversion

systems and the relatively small surface area available on the motor vehicle for PV panels installation, their output power is in the order of the hundreds of Watts, which compared to kWs available from ICE would lead to consider insignificant their contribution in the system energy management. Such a speech, however, is not correct considering the actual use, in urban areas, of cars consisting in small and short time displacements. In this case, the energy available from PV panels, while driving and particularly during parking, can constitute a major fraction (about 20-25%) of that required to meet the driving demand as shown in Table 1.1 - Energy impact of PV panels on motor vehicles Table 1.1.

Table 1.1 - Energy impact of PV panels on motor vehicles

	Power (kW)	Mean Power (kW)	Vehicle using time (h/day)	Energy (kWh/day)
Car	70	8	1	8
PV Panel	0,3	0,2	10	2
Ratio	0,004	0,025	10	0,25

Starting from 2005, the University of Salerno is a reference point as for solar hybrid vehicles. A prototype was developed and several studies have been carried out dealing with the development and validation of mathematical models for optimal design of hybrid-solar vehicles, the energy management systems and the vehicle's on-board control through a Rule-Based Control Strategy [10].

Figure 1.7 – Piaggio Porter solar hybrid vehicle prototype

CHAPTER 2

The HySolarKit project

Despite the recent commercial success of HEVs, their market share is still insufficient to produce a significant impact on energy consumption on a global basis and relevant investments on production plants would be needed in order to improve manufacturers' performance about their production rate. This fact could, of course, impair the global impact of these innovations on fuel consumption and CO_2 emissions, at least in a short-term scenario. Therefore, the possibility of upgrading conventional vehicles to hybrid vehicles, possibly PV assisted, is gaining increasing interest. Such a proposal has been recently formulated and patented at the University of Salerno (www.hysolarkit.com). The conversion of a conventional vehicle to a hybrid solar vehicle is obtained by installing flexible solar cells on vehicle bonnet and hoof, an additional battery (Lithium-Ion) and two electrically driven in-wheel motors on rear axle. In that way, the vehicle can operate in pure electric mode (when ICE is switched off or disconnected by the front wheels) or in hybrid mode (when the ICE drives the front wheels and the rear in-wheel motors operate in traction mode or in generation mode, corresponding to a positive or negative torque). The battery can be recharged both by rear wheels, when operating in generation mode or during braking and downhill, and by photovoltaic panels. Optionally, the battery could be recharged also by the grid, in Plug-In mode. A VMU receives data from OBD gate such as pedal position, vehicle speed, engine speed, manifold pressure and other variables, from battery (SOC estimation) and drives in-wheel motors by properly acting on the electric node EN (Figure 2.1). A display on the dashboard may advice the driver about the actual operation of the system.

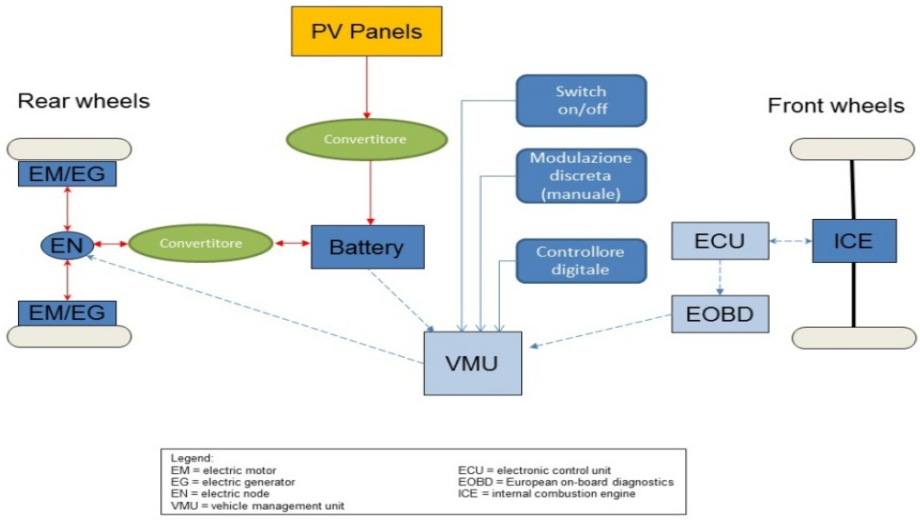

Figure 2.1 - Solar hybrid prototype operating scheme

2.1 HySolarKit advantages

The most relevant advantages of the kit for solar hybridization are CO_2 emissions and fuel consumption reduction. In fact, the performance of an internal combustion engine and its emissions are greatly influenced by operating conditions and the lower is the power required for a given rpm the worse they are. This happen during vehicle urban use characterized by low torque and speed. The objective of the kit control system is to move the thermal engine operating point (depending on the driving requirements) from a low to high efficiency condition by charging or discharging the battery depending on whether the delivered torque is higher or lower than useful one. Moreover, the in wheel motors provide assistance during acceleration depending on torque desired by driver and recover energy during braking recharging the battery which is connected to photovoltaic panels. The benefits in terms of fuel savings are lower than on a native hybrid, due to the constraints posed by the TTR structure, and by the absence of downsizing. On the other hand, the addition of the electric propulsion may offer further advantages:

- Enhancement of vehicle power and performance, in particular acceleration because of high starting torque from in wheel motors
- Increase in vehicle reliability, due to presence of two propulsion systems
- Better drivability, due to the possibility of exploiting advanced vehicle control schemes
- Possibility of collecting data on the actual engine and vehicle working points in order to develop models for predictive maintenance strategies

As for the payback time, it must be said that this aspect is closely linked to the cost of the technology needed to implement the kit (solar panels, batteries, in wheel motors, data acquisition system), which is sharply falling down in last years. Preliminary conservative studies show that, at worst, the payback time is around 5 years.

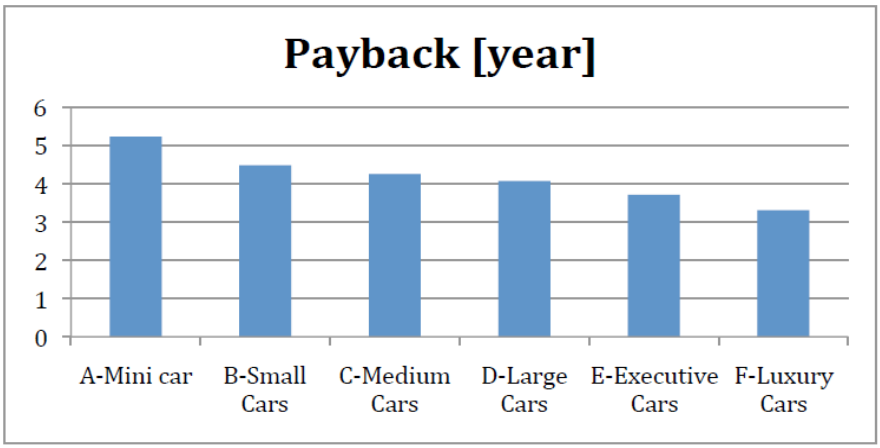

Figure 2.2 - Payback time for different vehicle class

Last but not least is the possibility of using HySolarKit by automobiles manufacturers and sell it to them. In such a way, they could align their production to the market without important modification to plants and significant cost savings gaining in competitiveness.

2.2 HySolarKit components overview

As quickly said previously, Kit hardware consists in:

- 2 in wheel motors installed on back axle
- A Li-ion Battery
- An OBD hardware interface to acquire data from OBD gate
- 2 PV panels installed on vehicle bonnet and roof
- An on board control system to elaborate input data and output control signals

These components are opportunely integrated in the vehicle as shown in Figure 2.3.

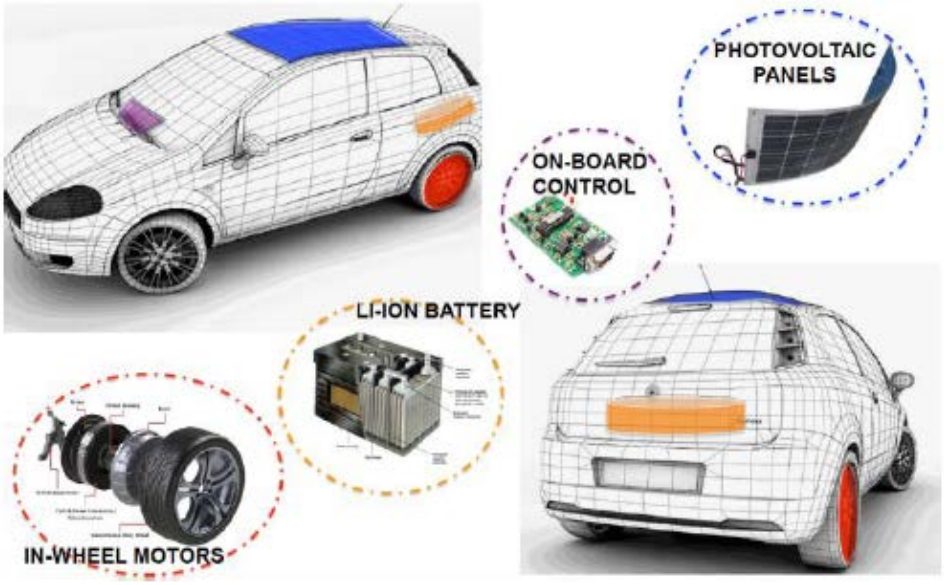

Figure 2.3 - Hybridization Kit - Vehicle integration

2.2.1. In wheel motors

One of the most interesting aspects of the solar hybridization kit is represented by the upgrade of vehicle power and the partial recovery of kinetic energy allowed by in wheel motors. The use of in wheel motors (IWM) allows to electrify the vehicle with no impact on mechanical

transmission. A significant amount of space is therefore saved in the vehicle, compared to other hybrid solutions where electric motor is placed out of vehicle chassis. A hub motor typically may be designed in three main configurations [11]. The least practical is an axial-flux motor, where stator windings are typically sandwiched between sets of magnets. The other two configurations are both radial designed with the motor magnets bonded to the rotor. In one of them, the rotor sits inside the stator, as in a conventional motor while, in the other one, the rotor sits outside the stator and rotates around it. A typical IWM scheme is shown in Figure 2.4.

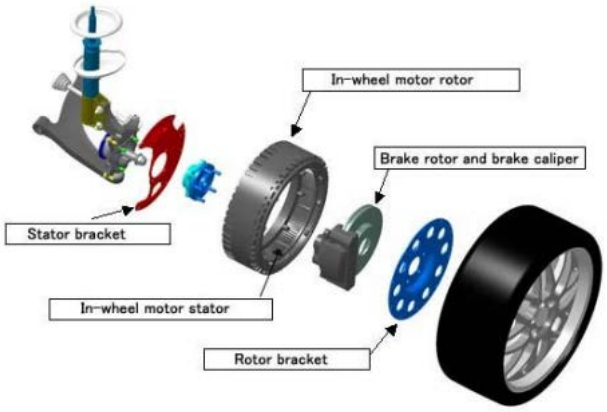

Figure 2.4 - General In wheel motor scheme

The application of hub motors in cars is still evolving, and no configuration has become standard. In wheel motors main problem is their high weight that may affect comfort and safety. The so-called "non-suspended" masses (i.e. in wheel motors and brakes) must be as light as possible compared to "suspended masses" that, actually, consist in the entire body of the car [12]. The addiction of IWM makes the normal vehicle a 4x4 traction one. Vehicle safety and stability can be enhanced by implementing an accurate electronic control of driving and braking torque, separately for each wheel. Moreover, a significant improvement in acceleration capability is achieved, thanks to the higher torque delivery at low rotation speed typical of electric motors (Figure 2.6). In order to develop the hybridization kit patented by University of Salerno, IWM produced by Kelly Controllers have been purchased on Chinese market.

Figure 2.5 - Kelly in wheel motor

Their features and characteristics are shown in Figure 2.6 and Table 2.1

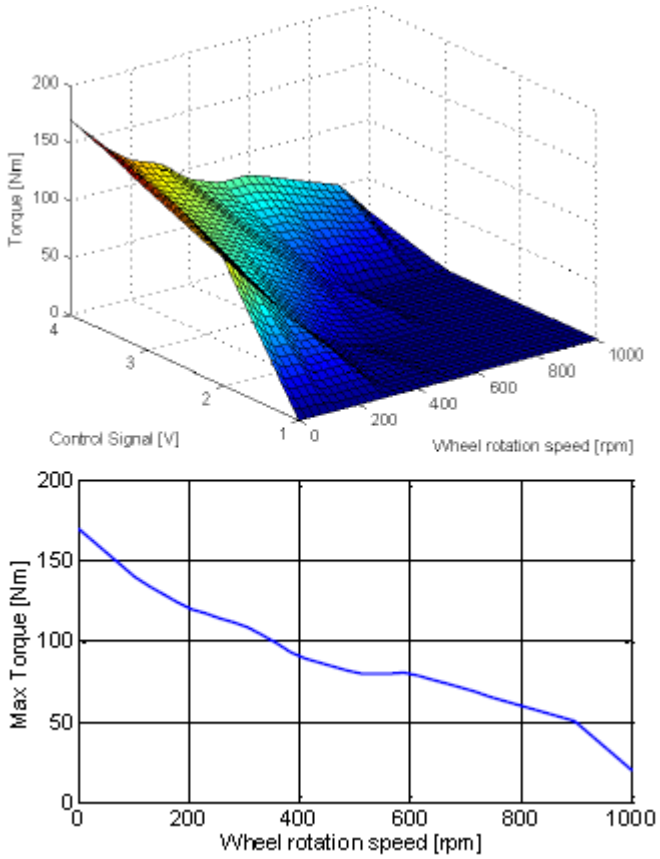

Figure 2.6 - In wheel motors maps

Table 2.1 - Single in wheel motor characteristics

Pick Power	7 [kW]
Pick Torque	150 [Nm]
Diameter-Width	303-107 [mm]
Max Speed	1500 [rpm]
Weight	20 [kg]

2.2.2. Lithium battery

A lithium-ion battery (Li-ion battery or LIB) is a member of a family of rechargeable battery types in which lithium ions move from the negative electrode to the positive electrode during discharge and back when charging. Li-ion batteries use an intercalated lithium compound as one electrode material, compared to the metallic lithium used in a non-rechargeable lithium battery. The electrolyte, which allows for ionic movement, and the two electrodes are the constituent components of a lithium-ion battery cell. Lithium-ion batteries are common in consumer electronics. They are one of the most popular types of rechargeable batteries for portable electronics, with a high energy density, small memory effect and only a slow loss of charge when not in use. Beyond consumer electronics, LIBs are also growing in popularity for military, battery electric vehicle and aerospace applications [13]. For example, lithium-ion batteries are becoming a common replacement for lead acid batteries for golf carts and utility vehicles and storage systems for hybrid and electric vehicles because of their high energy density. In accordance with recent progress on lithium-ion battery technology, increasing reliability and safety, and decreasing cost, it has been chosen to employ a Li-ion battery pack for the purpose of the prototype. The system has been designed and developed ad hoc, optimized for the hybridization kit operations. Although the initial scope of the project was to obtain a hybrid vehicle, the battery has been purposely oversized to be eventually adapted to plug-in operations. In fact, while most existing HEVs are equipped with batteries of about 1.5-2 kWh energy storage, our prototype features a 4 kWh battery pack, more aligned towards plug-in vehicles. The pack, installed in the trunk (in the spare-wheel compartment, Figure 2.7) consists of 30 cells,

operating within a voltage range of 83-117 V and maximum current of 150 A, with dimensions of 610 x 515 x 250 mm and mass of 65 kg. It is connected to a National Instruments NI 6212 bus-powered USB M series multifunction data acquisition (DAQ) module, which manages its operation and evaluates data such as voltage, current (for diagnostics and SOC estimation).

Figure 2.7 - Prototype Li-ion battery pack

It is worth noting that the battery pack has not been optimized yet, in terms of dimensions and weight, as Figure 2.7 shows, and it is expected that the final design could be up to 50% smaller and lighter than the current version.

2.2.3. The OBD standard and hardware interface

On-board diagnostics (OBD) is an automotive term referring to a vehicle's self-diagnostic and reporting capability. OBD systems give the vehicle owner or repair technician access to the status of the various vehicle subsystems. The amount of diagnostic information available via OBD has varied widely since its introduction in the early 1980s versions of on-board vehicle computers. Early versions of OBD would simply illuminate a malfunction indicator light or "idiot light" if a problem was detected but would not provide any information as to the nature of the problem. Modern OBD implementations use a standardized digital communications port to provide real-time data in addition to a standardized series of diagnostic

trouble codes, or DTCs, which allow one to rapidly identify and remedy malfunctions within the vehicle. OBD-II is an improvement over OBD-I in both capability and standardization. The OBD-II standard specifies the type of diagnostic connector and its pinout, the electrical signaling protocols available, and the messaging format. It also provides a candidate list of vehicle parameters to monitor along with how to encode the data for each. There is a pin in the connector that provides power for the scan tool from the vehicle battery, which eliminates the need to connect a scan tool to a power source separately. However, some technicians might still connect the scan tool to an auxiliary power source to protect data in the unusual event that a vehicle experiences a loss of electrical power due to a malfunction. Finally, the OBD-II standard provides an extensible list of DTCs. As result of this standardization, a single device can query the on-board computer(s) in any vehicle. This OBD-II came in two models OBD-IIA and OBD-IIB. OBD-II standardization was prompted by emissions requirements, and though only emission-related codes and data are required to be transmitted through it, most manufacturers have made the OBD-II Data Link Connector the only one in the vehicle through which all systems are diagnosed and programmed. OBD-II Diagnostic Trouble Codes are 4-digit, preceded by a letter: P for engine and transmission (powertrain), B for body, C for chassis, and U for network. In terms of data used for the development of the additional control system, the most important are:

- Vehicle rpm and speed
- Mass air flow and pressure
- Gas pedal position

These data are acquired through a standard hardware interface named ELM 327. This interface allows the communication between the OBD gate and the controller by a software developed in labview.

Figure 2.8 - ELM 327 hardware interface

2.2.4. Flexible solar panels

In last years, PV panels technology has significantly grown and, at the same time, its costs have decreased paving the way for the use of this technology in several application fields and automotive could represent one of these.

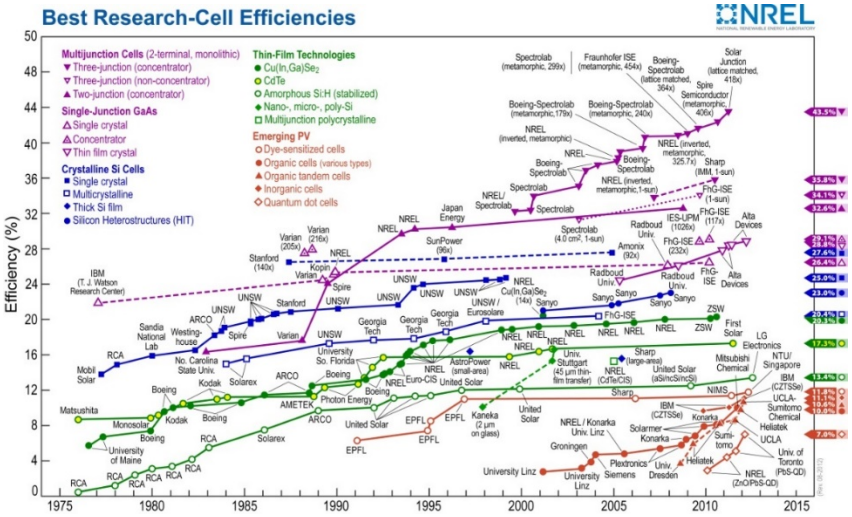

Figure 2.9 - PV panels efficiency evolution

Anyway, the most important limitation to the use of this technology for traction purpose is its low energy density and the relatively small surface area available for installation on the vehicle of the photovoltaic panels). Data related to the useful surfaces for the installation of photovoltaic panels on a Fiat Grande Punto are reported.

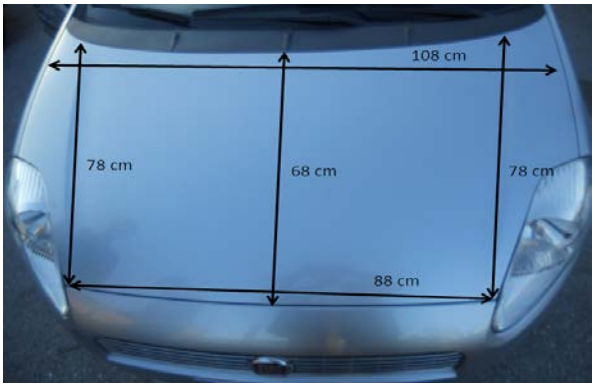

Figure 2.10 - Useful surface on prototype bonnet

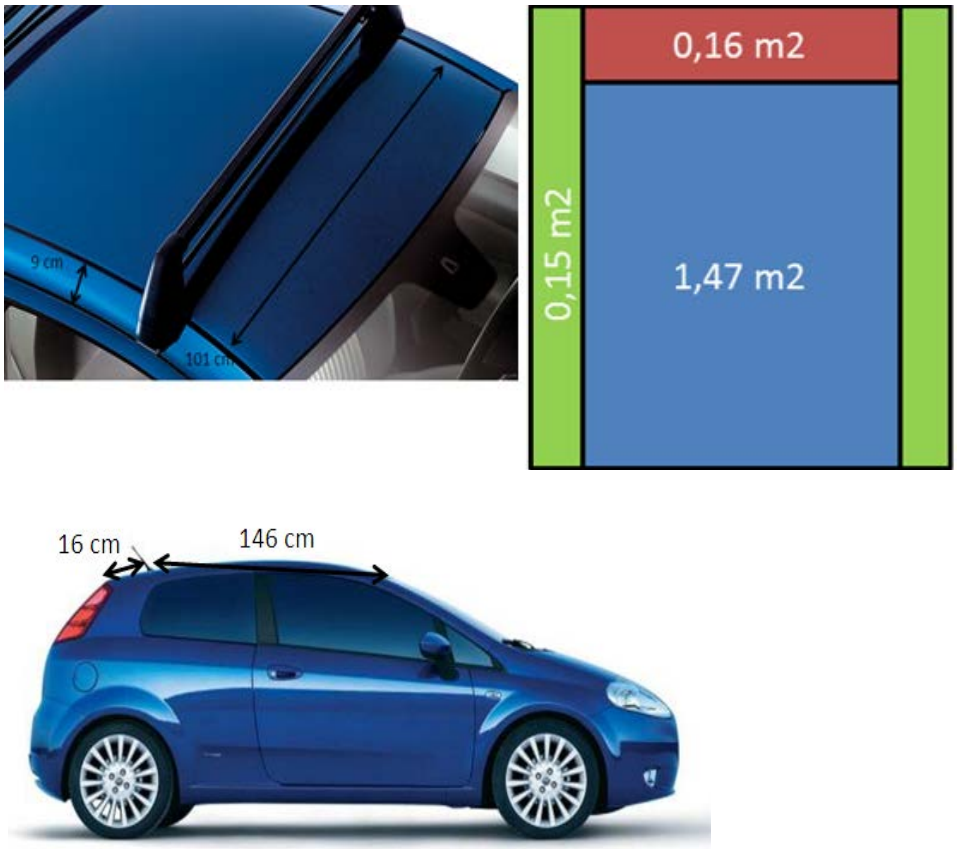

Figure 2.11 - Useful surface on prototype roof

Solar panels task is to recharge the battery in order to partially restore the energy used to supply power to in wheel motors. However, PV panels recharging rate is slow compared to discharging one, but the advantage lies in the fact that the battery can also be recharged during parking phases that, for a city car, are the most relevant part of the time justifying their installation and use. This hypothesis becomes even more reasonable taking into account the average use of a car, which, for over 35% of Europeans, is limited to displacements of less than 10 km requiring a relatively low amount of energy comparable to energy available from PV panels. On the prototype developed by University of Salerno high-efficiency (18%) single-crystal silicon HF65 panel have been installed on the vehicle roof and hood, for a total of about 270W of installed power. In particular, each panel measures 1370x344 mm and weighs 1.2 kg.

They were supplied by the Italian company Enecom,

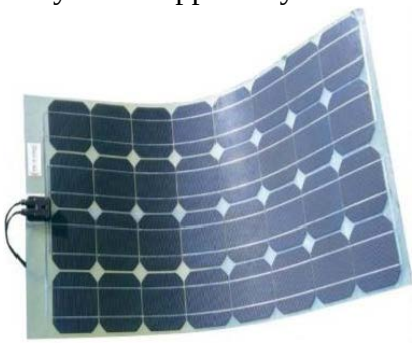

Figure 2.12 - Enecom PV panels

2.2.5. On board control system

The on board control system is constituted by:

- A Notebook
- 1 NI-USB 6212

These two elements will be substituted in the final version of the prototype by a microcontroller that will be able to accomplish either computational part (Notebook) or management of input-output signals (NI-USB 6212).
The NI USB-6212 is a bus-powered USB M Series multifunction DAQ module optimized for superior accuracy at fast sampling rates. It offers 16 analog inputs; 400 kS/s sampling rate; two analog outputs; 32 digital I/O lines; four programmable input ranges (±0.2 V to ±10 V) per channel; digital triggering; and two counter/timers. The USB-6212 is designed specifically for mobile or space-constrained applications. Plug-and-play installation minimizes configuration and setup time, and direct screw-terminal connectivity keeps costs down and simplifies signal connections. This product does not require external power. The USB-6212 also features new NI Signal Streaming technology, which gives you DMA-like bidirectional high-speed streaming of data across the USB bus. For more information about NI Signal Streaming technology, view the Resources tab. Each module features an OEM version. Check the Resources tab or use the left navigation to get pricing and technical information. Moreover, NI-DAQmx driver and measurement services software provides easy-to-use configuration and programming interfaces with features such as the DAQ Assistant to help reduce development time.

CHAPTER 3

The prototype implementation

The prototype complete implementation has been realized at the University of Salerno and can be divided in two different parts:

- Hardware implementation
- Software implementation

3.1 Hardware implementation

The hardware implementation deals with the installation of kit components on the Fiat Grande Punto in order to obtain the vehicle hybridization. It is important to point out how these operations have to take into account some very important aspects as:

- Keep the inside of the vehicle comfortable and safety for the driver and any passenger
- Consider components size and their possible allocation in the vehicle
- Isolate installed components from vibration due to irregularity of the road

3.1.1. IWM installation

The most important aspect for the safety of the system is the installation of the IWM in place of conventional wheels on the back axle. Back wheels have been completely removed and, unfortunately, the mechanical braking system on the back axle with them. Anyway, this problem and its solution will be object of the following chapter. Once this operation was completed, it has been necessary to take some measurement in order to understand if modifications to the wheels support plates on the back axle were needed in order to house IWM hub. At this purpose, the support plate central hole width has been increased of 3 mm.

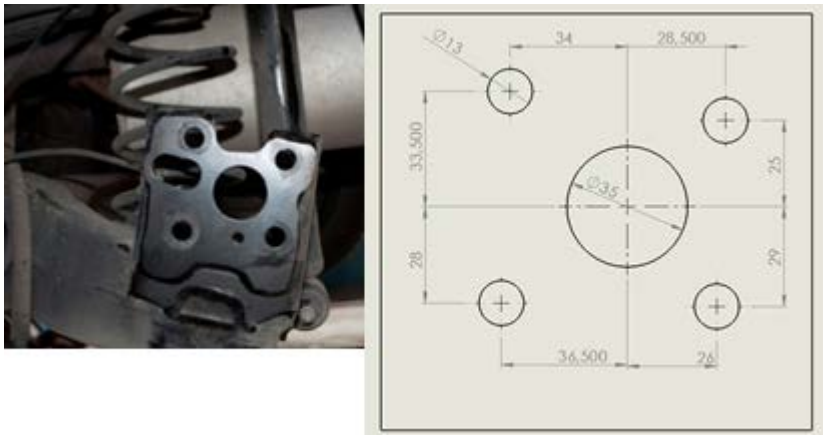

Figure 3.1 - Back axle support plate picture and dimensions

The fixing system of the IWM to the axle plate is constituted by another plate to be bolted to the first one and a hallow cylinder which houses the IWM hub and stuck it by a spline key. These two elements are welded each other to obtain a single element as shown in Figure 3.2.

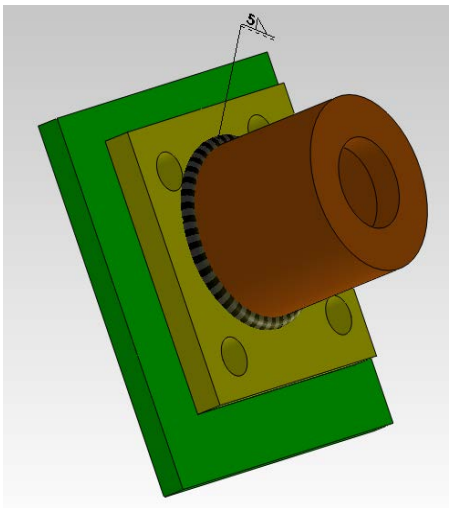

Figure 3.2 - Designed fixing system

The system has been opportunely designed considering forces and torque applied to the back axle and several simulation have been carried out in order to test its reliability. The software used for the simulation is Ansys and the model based approach is defined by FEM analysis. Further details

are reported in [14]. The complete system overview constituted by IWM, back axle support plate and designed fixing system is reported in Figure 3.3, while the installation result on the prototype is shown in Figure 3.4.

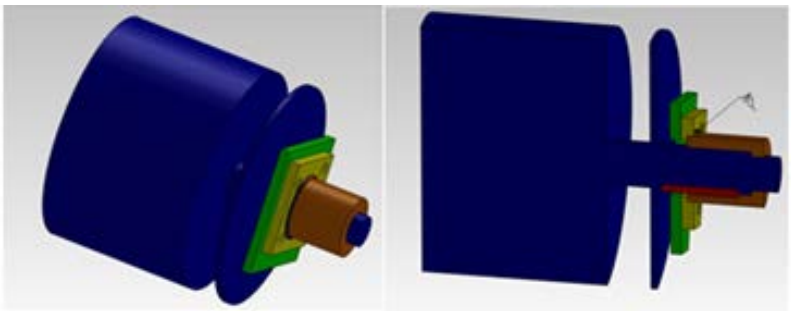

Figure 3.3 Fixing system model overview

Figure 3.4 - IWM Prototype installation result

3.1.2. Battery pack installation

The battery pack, as the majority of the kit components, has been placed in the vehicle hood. In order to reduce vibration, a damping material has been interposed between the battery pack and the hood ground, which has been opportunely reinforced with some plywood. On the battery top, fixed to it by two iron plate, the IWM drivers have been placed. Cables coming from IMW arrive in the vehicle hood through two holes in the vehicle chassis

and have been bolted on IWM drivers connected to the battery by a standard connector and a 7mm diameter width cables in order to sustain currents up to 150 Ampere.

Figure 3.5 – Battery pack, IWM drivers and control system arrangement in vehicle hood

In this case, safety plays a crucial role and the user need to be protected from possible overcurrent and software failure. In order to avoid overcurrent problems, two contactor, one for each driver, have been installed in the battery pack circuit. A contactor is an electrically controlled switch used for switching an electrical power circuit, similar to a relay except with higher current ratings [15]. A contactor is controlled by a circuit, which has a much lower power level than the switched circuit. In that way, if current is higher than 150 Ampere the battery shut off protecting IWM from damage.

Figure 3.6 - Installed battery pack contactor

On the other hand, in case of software failure, battery could supply power to IWM although driver does not request it. Because of this reason, an emergency button has been placed in the vehicle cockpit so that battery can be switched off when driver desire it; it has been placed close to gearshift in a simply accessible position as shown in Figure 3.7.

Figure 3.7 - Emergency button placement

3.1.3. PV panels installation

PV panels installed on the prototype are flexible and very light. These characteristics have led to a very simple solution in terms of prototype development. In fact, they have been fixed on vehicle bonnet and roof using a special double-sided tape very resistant to high temperature. In order to improve tape-fixing power, pv panels have been pressed for 72 hours on it.

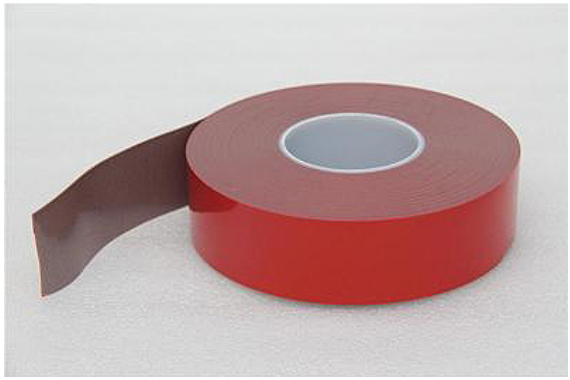

Figure 3.8 - Double sided tape

The vehicle hood also houses the elements to connect pv panels to the

battery pack. In particular, these elements are:

- The inverter for the MPPT
- An auxiliary buffer battery
- A Voltage booster

The inverter for the MPPT connects pv panels to the auxiliary battery. The Maximum Power Point Tracking (MPPT) is a technique that charge controllers use for wind turbines and photovoltaic solar systems to maximize power output. Photovoltaic cells have a complex relationship between their operating environment and the maximum power they can produce. For any given set of operational conditions, cells have a single operating point where the values of the current (I) and Voltage (V) of the cell result in a maximum power output [16]. These values correspond to a particular load resistance, which is equal to V/I as specified by Ohm's Law. The power P is given by P=V*I. A photovoltaic cell, for the majority of its useful curve, acts as a constant current source. However, at a photovoltaic cell's MPP region, its curve has an approximately inverse exponential relationship between current and voltage. From basic circuit theory, the power delivered from or to a device is optimized where the derivative (graphically, the slope) dI/dV of the I-V curve is equal and opposite the I/V ratio (where dP/dV=0). This is known as the maximum power point (MPP) and the inverter objective is to make pv panels work in that particular point.

Figure 3.9 - Inverter for the MPPT

The buffer battery has a low capacity (6 Ah) and works at 24 Volts. The last component before the main battery pack is a booster that rises voltage from 24 V (buffer battery voltage) to 96 V (main battery voltage) making the whole system work.

Figure 3.10 – PV panels installed on Fiat Grande Punto

3.1.4. Controller installation and system wiring

Part of the controller (NI-USB 6212) has been placed in vehicle hood fixed on the top of battery in the same way of the drivers. It is connected to the battery to read information about voltage, current, state of charge (SOC) and switch it on or off. On the other hand, it is connected to IWM drivers to modulate control signal and make the IWM work during braking or propulsion phases. Moreover, The NI-USB 6212 communicates with a Notebook through a shielded USB cable. The Notebook (placed in the vehicle cockpit) takes data from OBD as described in section 2.2.5 and makes the control software run. In order to perform its duties, NI-USB 6212 need to be power supplied. At this purpose, power is taken from vehicle

12V lead acid battery as shown in Figure 3.11.

Figure 3.11 - 12V battery wiring for power supply

The whole system has been completely wired as safe as possible. In particular, Cables coming from bonnet (PV bonnet panel, battery power supplier) and vehicle cockpit (OBD connector, Shielded USB, emergency button) arrive to vehicle hood through vehicle chassis being covered by an isolating material (look at Figure 3.12).

Figure 3.12 - system wiring

On the other hand, roof pv panels cables arrive to vehicle hood through taillight. In this way, hardware prototype implementation is definitively completed.

3.2 Software implementation

The software for system control has been developed in Labview (Laboratory Virtual Instrument Engineering Workbench). It is a very useful software for data acquisition, electronic instruments management, signal processing and analysis. The programming environment is called "G programming language", since it is based on block diagrams that can be linked each other to obtain the whole software. The practical benefit of the graphical approach is that it puts more focus on data and the operations being performed on that data, and abstracts much of the administrative complexity of computer programming such as memory allocation and language syntax. G code can be related to flow charts and other familiar visual representations of processes resulting very intuitive and easy to learn. On the other hand, expert programmers can also take advantage of the productivity gains by working at a higher level of abstraction while still employing advanced programming practices such as object-oriented design, encapsulation, and code profiling. In addition, a set of library functions can be recalled and used during the software development. They include commonly used functions (arithmetic and statistical functions, string manipulation functions etc.), but also special functions for data acquisition and signal processing. A software coded in Labview is called Virtual Instrument (VI).
A VI is composed of three fundamental parts:

- The front panel
- The block diagram
- Icons / Connectors

The Front Panel represents the software/user interface while the block diagram contains the code in the form of block diagram and consists of "nodes", which are processing elements, "links" that combine nodes and allow information exchange. Last, icons and connectors are the single elements defining the VI itself.

3.2.1. The user interface

The user interface is very basic ad it is designed to simplify at most the user operations. It is constituted by five virtual buttons, two monitors to visualize battery voltage and current, the IWM control signal modulator

and a stop button as reported in Figure 3.13.

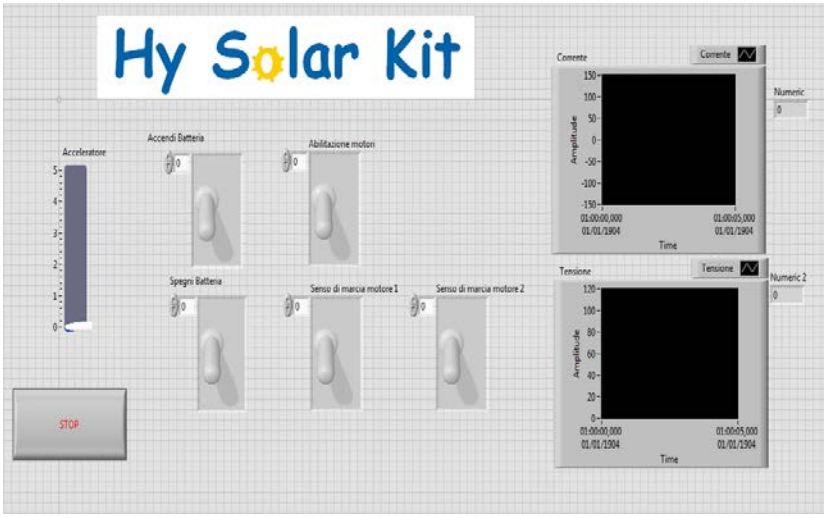

Figure 3.13 - Software front panel

In particular, the front panel allows the user to:

1. Switch on/off the battery pack
2. Enable/disable electric motors
3. Invert IWM rotation
4. Monitor battery current and voltage
5. Modulate IWM control signal

As for IWM control signal modulation, two options are possible; in fact, it can be manually modulated by the user or, more reasonable, it is defined by the control strategy implemented on the vehicle. Moreover, it is important to appropriately define IWM rotation in such a way it is opposite respectively so that the vehicle can run without any problems.

The user interface has been improved by time; in particular, the estimation of battery SOC, electric power output, PV panels power input, visualization of several data acquired and leds for hybrid, pure electric or conventional vehicle working state definition have been implemented. This new interface, which does not substitute the first one, but works with it, is reported in Figure 3.14.

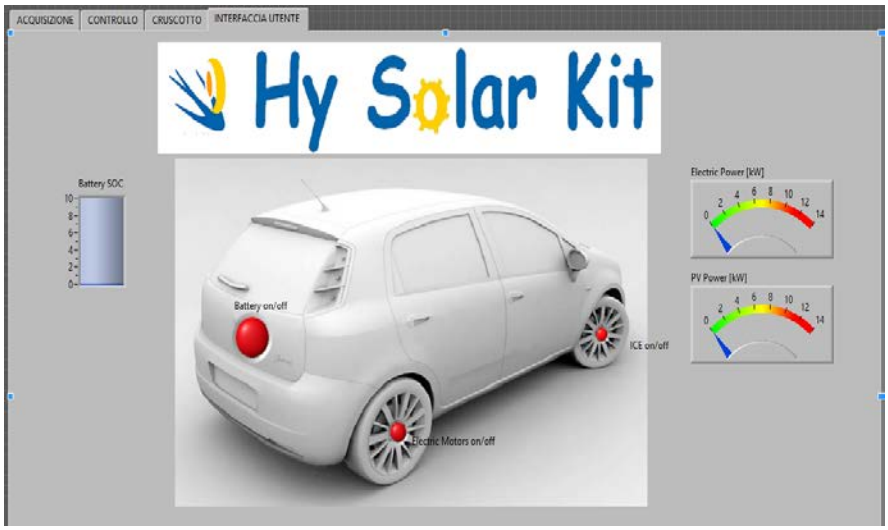

Figure 3.14 – User interface upgrade

3.2.2. The block diagram

The software development is carried out in the block diagram. The communication with NI-USB 6212 is obtained through a software tool named DAQ-Assistant which has to be opportunely set depending on channel input/out characteristics.

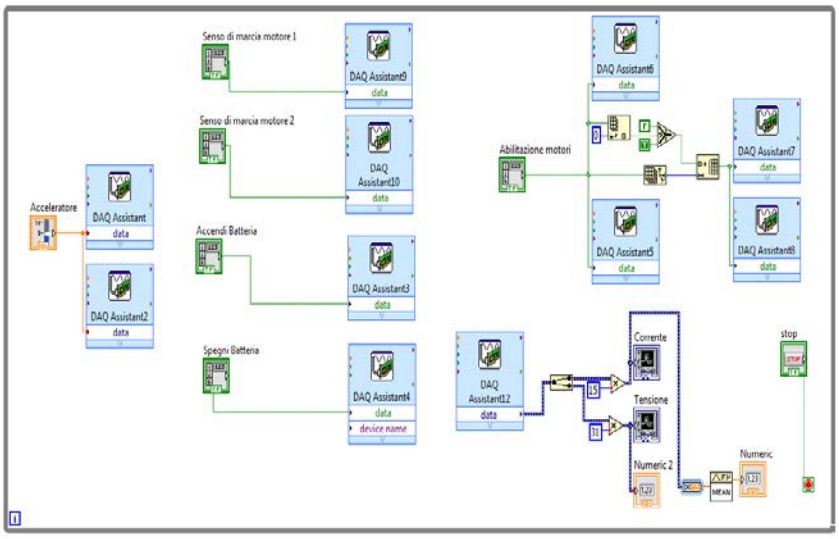

Figure 3.15 - Software block diagram

The IWM signal modulation has been set as an analogical signal and its value ranges from 0 to 5 V. This is the only analogical signal output while the other ones are digital output. Details on DAQ- Assistant configuration are reported in Figure 3.16.

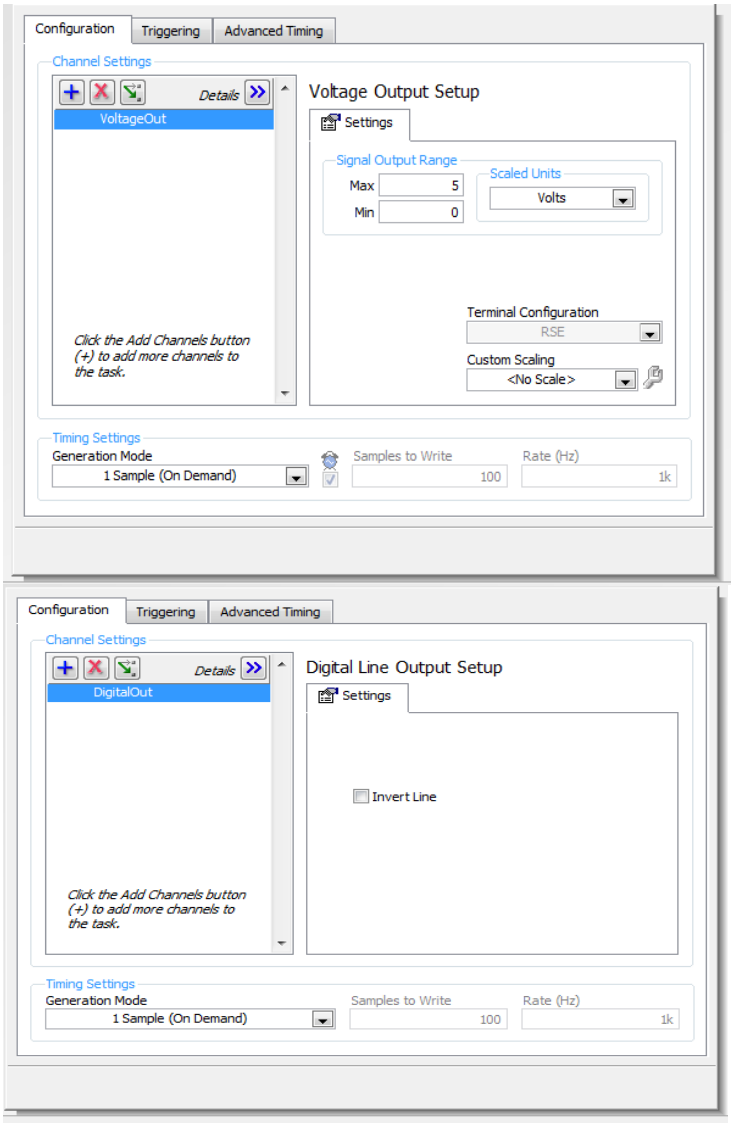

Figure 3.16 - Analogical and digital DAQ -Assistant configuration

The communication with NI-USB 6212 described above can't be

carried out until data acquired by OBD gate are not processed and the output signal are defined by the control strategy. The development of the control strategy has been carried out in Matlab, and its integration in labview has been obtained through a function named Matlab-script. The "MathScript Node" offers an intuitive means of combining graphical and textual code within LabVIEW. Using "MathScript Nodes", you can enter .m file script text directly or import it from a text file. It is possible to define named inputs and outputs on the MathScript Node border to specify the data to transfer between the graphical LabVIEW environment and the textual MathScript code. Moreover, it is possible to associate .m file script variables with LabVIEW graphical programming, by wiring node inputs and outputs and transfer data between .m file scripts with the graphical LabVIEW programming. Part of these operations are reported in Figure 3.17.

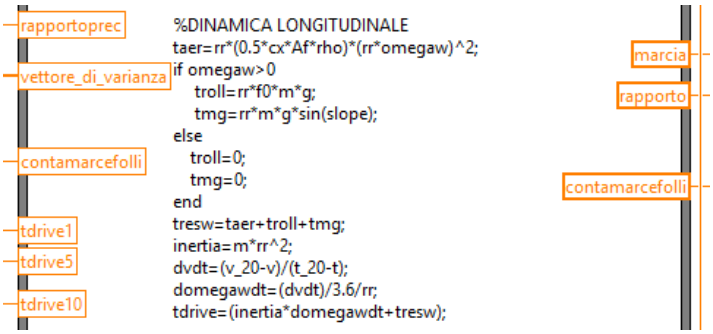

Figure 3.17 - Control strategy excerpt

The entire code is then closed in a "While Loop" which is represented by the black frame in Figure 3.15. This is necessary since data acquisition and their processing have to be carried out continuously until the stop button is pushed. At this point, OBD-labview communication interface for data acquisition (developed by Autoconsulting S.a.s), IWM-battery-NI-USB communication interface for signal input/output and control strategies implementation in Matlab-script for vehicle management define the entire structure of the control system for conventional vehicle hybridization.

CHAPTER 4

Driver’s intention analysis

In order to understand when and how to distribute power deriving from electric wheel motors it is important to certainly establish the driver's intention to avoid undesired driving situations which could even cause accidents. At this purpose, a very interesting and useful information may be, for instance, the power at the wheel and therefore the wheel torque at a certain instant of time which allows to distinguish traction phases (positive driving torque) from braking ones (negative torque) and those in which the vehicle doesn’t move (no torque). Anyway, this is just a single variable that can be taken into account from vehicle control system that elaborate much more data. As previously mentioned, the vehicle management is realized through a Vehicle Management Unit (VMU) that takes data from the OBD port, available in all modern cars. The reason of this choice is to develop a kit that does not require any modifications to the original ECU and does not interfere with its operation. The control strategies implementable on this hybridized vehicle are different from those implementable on a full hybrid vehicle, since the choice of designing a control system parallel to the original ECU poses some specific limitations in terms of driving requirements and drivability. In fact, when the driver steps on the accelerator in the hybridized vehicle, so demanding higher vehicle power, an increase in the engine power will necessarily result; on the contrary, in a ‘native’ HEV the increase in vehicle power could be achieved even by reducing the engine power and, in parallel, by increasing the electric motor power. Similarly, in the hybridized vehicle a reduction in engine power will be always achieved when the driver releases gas pedal. It has to be remarked that the above limitations could be overcome if a Drive By Wire system would be adopted to decouple accelerator pedal from the original ECU. In this case, however, a more invasive modification to vehicle hardware would be required. Consequently, the achievement of a given level of power splitting between thermal and electric motor can be obtained by inducing the driver to modulate the pedal position until the desired vehicle power would be reached. In other words, the driver will act

as the vehicle is running downhill. On the contrary, the hybridized vehicle can operate in recharging mode when the in-wheel motors absorb part of the power generated by the engine: in this case, the driver will act on the pedal as the vehicle would run uphill. A study of driver/vehicle interactions has been carried out to develop implementable approaches for this kind of vehicle. In this context, the accurate real-time knowledge of the "Driver's Intention" plays a fundamental role in order to allow an effective and safe control of the wheel-motors. Actual driving condition is defined by the position of gas pedal, brake pedal and, in cars with manual transmission, gear position and clutch pedal. In the proposed hybridized car, it is assumed that all the information on Driver Intention would be achieved by processing in real-time the data acquired via the OBD port. In this way, the adoption of additional sensors on the vehicle (i.e. gas, brake and clutch pedal, gear position) could be avoided. This would reduce the cost of the kit, and makes it possible the same configuration to work on different cars. Since brake and clutch pedal position and active gear are not directly measured, they can be valued by processing the other variables and, in particular, gas pedal position, vehicle speed and engine speed. Braking torque can be computed by real time solution of the longitudinal model, starting vehicle speed and acceleration. The objectives of the OBD data processing are therefore the following ones:

- Detect if the gear is engaged or not and identifying the active gear, including the conditions of null or changing gear.
- Detect if the driver is going to upshift or downshift, since different actions to the wheel motors would be required.
- Estimate the vehicle torque and the engine torque; in particular, detect if a braking torque is needed to the wheel motors.
- Define the rules to drive wheel motors.

4.1 Longitudinal vehicle dynamics

The control of longitudinal vehicle motion has been pursued at many different levels by researchers and automotive manufacturers. Common systems involving longitudinal control available on today's passenger cars include cruise control, anti-lock brake systems and traction control systems

[17]. The vehicle dynamic is influenced by longitudinal tire forces, aerodynamic drag forces, rolling resistance forces and gravitational forces. Consider a vehicle moving on an inclined road as shown in Figure 4.1.

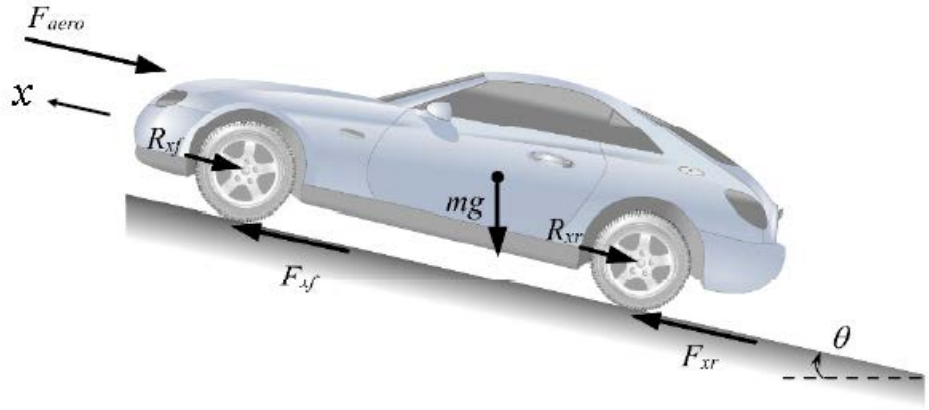

Figure 4.1 - Longitudinal forces acting on a vehicle in motion

Where:
F_{xf} is the longitudinal tire force at the front tires
F_{xr} is the longitudinal tire force at the rear tires aero
F_{aero} is the equivalent longitudinal aerodynamic drag force
R_{xf} is the force due to rolling resistance at the front tires xr
R_{xr} is the force due to rolling resistance at the rear tires
M is the mass of the vehicle
ϑ is the angle of inclination of the road on which the vehicle is traveling

The propulsion system produces mechanical energy that is assumed to be momentarily stored in the vehicle. The driving resistances are assumed to drain energy from this reservoir. The energy in the vehicle is stored:

- In the form of kinetic energy when the vehicle is accelerated.
- In the form of potential energy when the vehicle reaches higher altitudes.

A simplified longitudinal vehicle model is developed under the following hypotheses [18]:

- The drag force is considered acting on vehicle center of gravity.
- Vehicle inertia accounts for both vehicle mass (m) and rotational inertia of ICE, EM/EG and wheels, through the term M_{eff}

- The elasticity effects in the mechanical transmission are neglected.

According to these assumptions, and considering vehicle speed v, the power at wheels (P_{wheel}) can be modeled as follows:

$$P_{wheel} = P_{aero} + P_{roll} + P_{mg} + P_{inertia} \tag{4.1}$$

Where [18]:

$$\begin{aligned} P_{aero} &= 0.5\rho C_x A v^3 \\ P_{roll} &= mgvC_r \cos\vartheta \\ P_{mg} &= mgv \sin\vartheta \\ P_{inertia} &= M_{eff}\frac{dv}{dt}v \end{aligned} \tag{4.2}$$

The aerodynamic drag coefficient C_x may be obtained from coast down tests [19]on the vehicle [19] or provided by vehicle manufacturer.
The knowledge of power at wheel from OBD data through longitudinal dynamic, according the model described above, is extremely important in terms of driver's intention analysis; in fact, as previously mentioned, this information define driver's power request. Depending on it, it is possible to make IWM work in traction mode (positive power requested) or as regenerative brakes (negative power requested) charging the battery.

4.2 Active gear detection

Another important aspect to define driver's intention, but also ICE working points from longitudinal dynamic to fuel consumption and emissions estimation, is the active gear detection. At this purpose, a model has been developed and validated. In order to develop and validate the model, some sets of data acquired with a FIAT Grande Punto in batch mode have been used.

4.2.1. Active gear detection algorithm definition

As a preliminary step for control applications, the transmission ratios of the active vehicle should be known. These ratios could be calculated from the

previous knowledge of wheel radius and transmission ratios at gears and differential, provided by the car manufacturer. Anyway, these values could be identified on the real vehicle, both to take into account possible variations with respect to the theoretical values (i.e. due to effective wheel radius, or to different wheels), and to facilitate the application of the hybridization tool on different cars. To identify the active gear, the ratio R between the rotational speed of vehicle wheel and of the engine rotational speed has been defined and analyzed:

$$R = \frac{\omega_w}{\omega_e} = \frac{60v}{3.6r_w 2\pi \cdot rpm} \tag{4.3}$$

Where r_w is the wheel radius. This ratio assumes some precise values when a gear is active, that can be calculated by the knowledge of the transmission ratios at the gear and at the differential:

$$\bar{R}_i = \frac{1}{\tau_i \tau_d} \qquad i = 1, n_{gears} \tag{4.4}$$

In Figure 4.2 values computed for R are plotted in blue, while red lines represent the theoretical values corresponding to the five gears of the car. These gears refer to the experimental driving cycle whose speed is shown in Figure 4.4. Because of mechanical effects (Backlash, vibrations and elasticity effects in the transmission and in wheel radius) and of the limited resolution of vehicle speed in OBD data, where only integer values are used, the value of R, as defined, is not the same during active gear phases, exhibiting several oscillation respect to a mean value for each gear (Figure 4.3). Although in most of the driving time the blue line stays over the red lines, so correctly detecting the active gear, there are many points where the active gear is not detected.

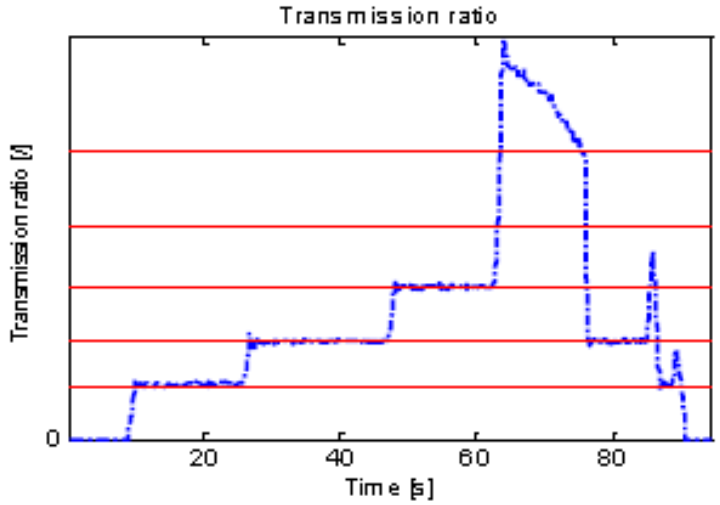

Figure 4.2 - Actual and reference values of transmission ratio R on a real driving cycle

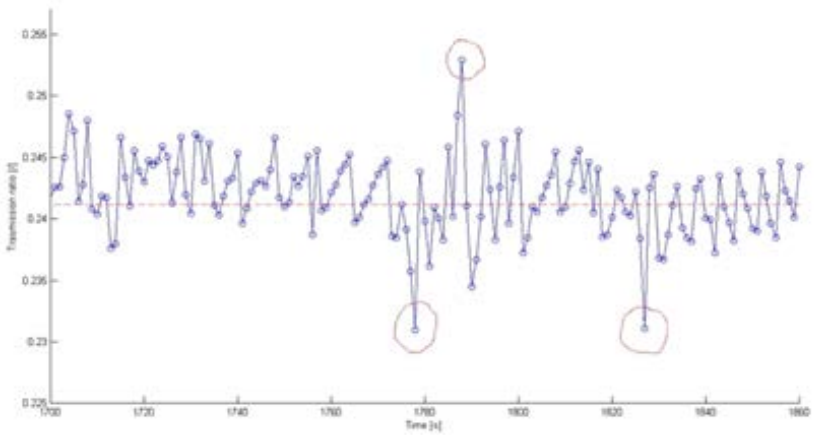

Figure 4.3 - Zoom of actual and reference values of transmission ratio R

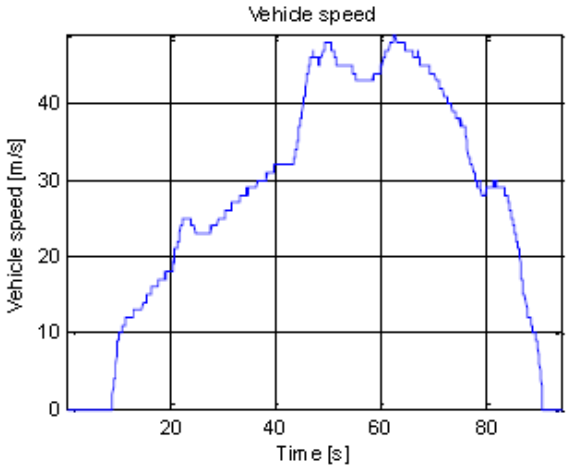

Figure 4.4 - Vehicle speed for an experimental driving cycle

Of course, this discretization effect of the order of 1/V is almost negligible at high vehicle speed, but becomes very significant when vehicle is running with first gear (Figure 4.5).

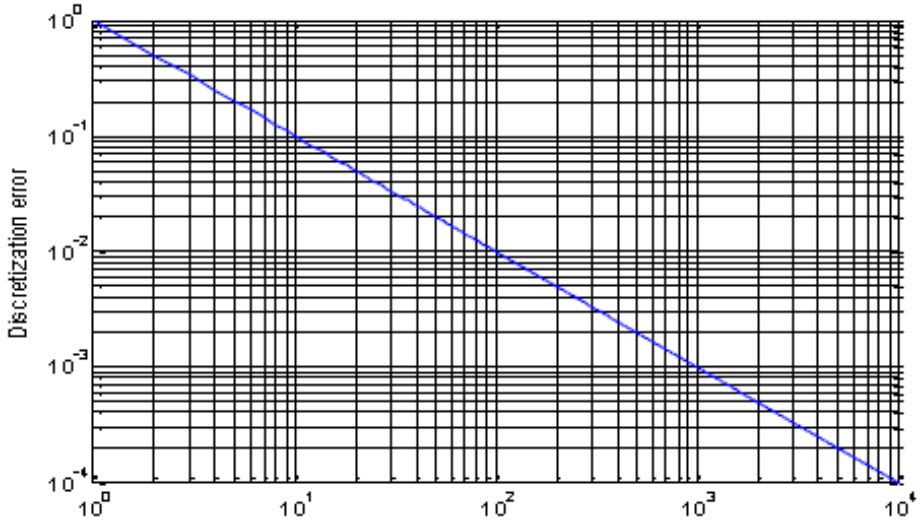

Figure 4.5- Discretization error for an integer number vs variable value

Moving averages and digital filtering has been used to process vehicle speed data, to remove the effects of discretization. Reference values of vehicle speed have been obtained with Infinite Impulse Response (IIR) backward zero-phase filtering (filtfilt), in batch mode (use of future data also). Good agreement with reference value has been found by use of filter

function (use of present and past data only). In order to precisely identify the transmission ratios, in the first phase of data acquisition a frequency analysis of R values is therefore performed, assuming that all the gear ratios are used. The identified values are then taken as reference to detect the active gear in the following part of the driving test.
A model to detect current gear has been then developed and tested in real-time on a FIAT Punto. The flow chart is presented in Figure 4.7. The gear detection algorithm is based on the comparison of measured transmission ratio with the values corresponding to the five gears, considering a variable error range:

$$|R - R_i| \leq \frac{2}{v} + 0.005 \qquad i = 1, n_{gears}$$

The algorithm has been tested over different real-world cycles made on the FIAT Grande Punto prototype. The simulation results have shown that the model has allowed a rather precise detection of the active gear over driving cycles, while some additional uncertainty remains in particular conditions, such as the engagement of first gear at low speed.

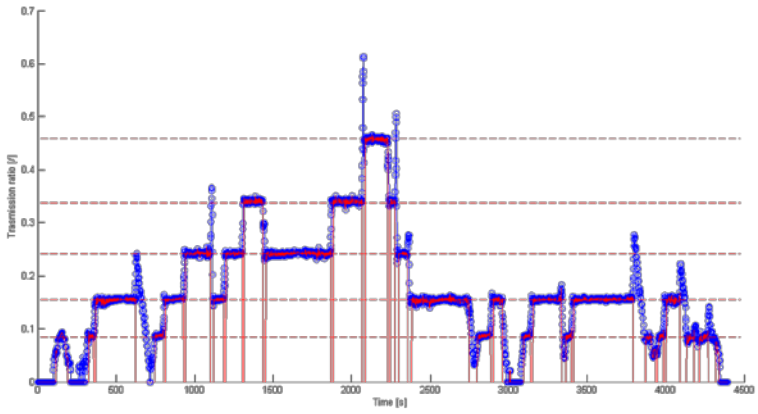

Figure 4.6 - Actual transmission ratio (blue) and identification of active gear (red)

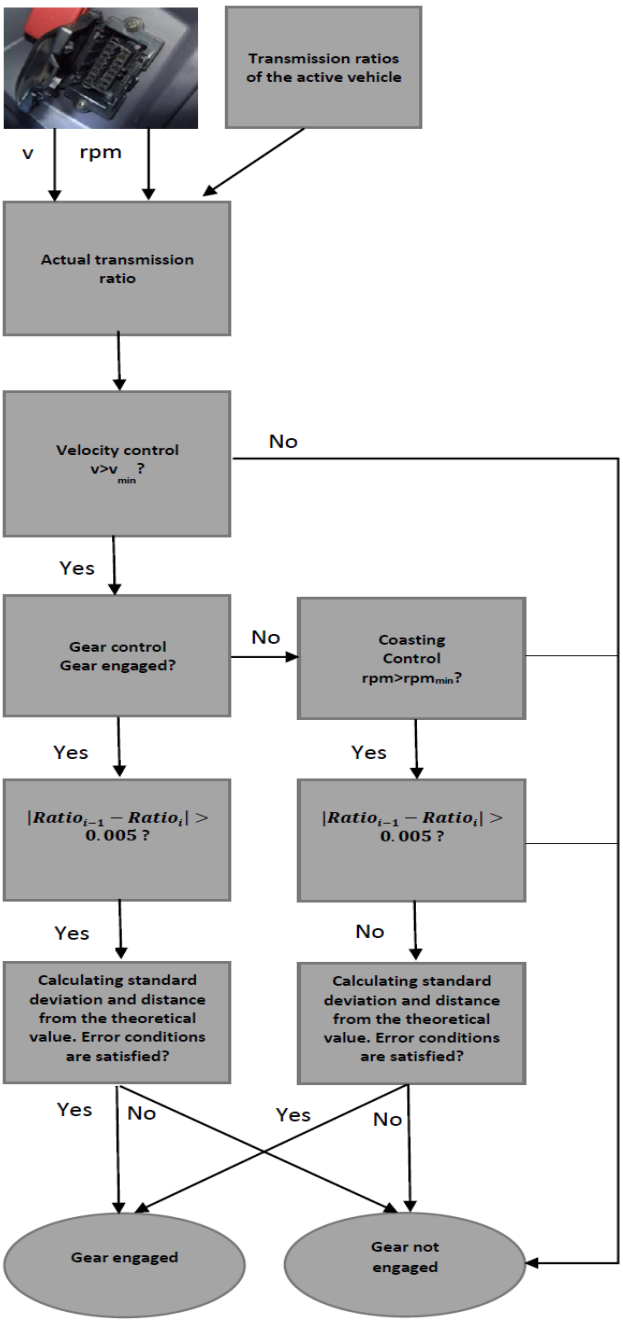

Figure 4.7 - Flow chart of the algorithm for active gear detection

4.2.2. Algorithm validation

In order to validate the algorithm, an on road test has been carried out. A digital video camera has been posed over the gearstick to compare the recorded time of gear shift with that computed by the algorithm.

Figure 4.8 - View of the camera on the gear

The knowledge of the reference time for gearshift would allow to optimize the algorithm, analyzing the contribution of each sub-model and identifying their optimal parameters. A comparison between the video and the computed gearshift at the same time has confirmed that the algorithm is quite correct in detecting gear shifting. Moreover, the computational time of the model is compatible with time constraints posed by real-time data acquisition and control. In order to evaluate the difference in time between video and algorithm gearshift, they have been plotted in Figure 4.9 and compared to the bisector line: the agreement between data results very high.

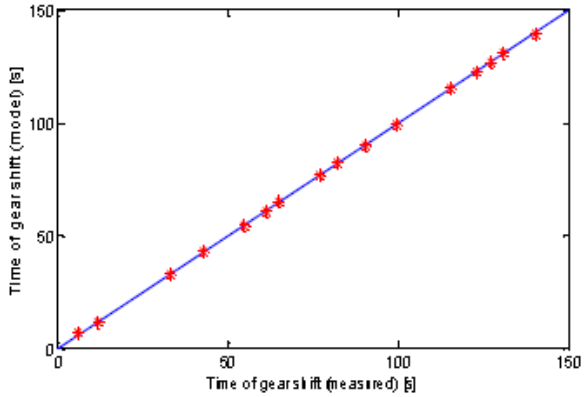

Figure 4.9 - Time of gearshift from the video vs time of gearshift from algorithm

The model validation has been obtained defining a relative error as:

$$e = \frac{Tg_v - Tg_a}{Tg_v} \quad (4.5)$$

Where Tg_v is the time of each gear shift on the video and Tg_a is the time of the same gearshift from the algorithm. The max error is 0,158 % and it has been obtained from a standing start condition in the engagement of first gear at low speeds. Moreover, has been calculated the 2-norm error and its value is 0.1596. The presence of a residual error is expected, since the gear is engaged after the actual release of the clutch, and, at that time, the value of the measured transmission ratio is still oscillating. In fact, without considering the first gearshift, the max error decreases to 0.0126 % and the 2-norm to 0.0194. In order to carry out a further study of mathematical matters of this analysis, it is possible to define two different function. One of this function, g*(t), describes the gear measured index deduced by the video; the other one, g(t), describes the gear measured index by the model. These two functions define the error function ε(t):

$$\varepsilon(t) = [g^*(t) - g(t)]^2 \quad (4.6)$$

In the function g(t) there are some parameters that influence model capability of predict the current gear and that can be optimized by minimizing ε(t) integral using matlab function as FMINCON that find minimum of constrained nonlinear multivariable function.

4.3 Driver's intention rules definition

The active gear detection represent an important additional variable to identify the Driver's Intention on a vehicle with manual gearbox. The algorithm has been integrated with the longitudinal dynamic model into a fuzzy set of rules, to define the best torque delivery for rear IWM. Fuzzy logic is a form of many-valued logic in which the truth values of variables may be any real number between 0 and 1, considered to be "fuzzy". By contrast, in Boolean logic, the truth values of variables may only be 0 or 1,

often called "crisp" values. Fuzzy logic has been extended to handle the concept of partial truth, where the truth value may range between completely true and completely false [20]. Furthermore, when linguistic variables are used, these degrees may be managed by specific (membership) functions [21]. Fuzzy control has been used also in automotive applications, particularly to model driver behavior [22], and it has been used to carry out the driver's intention analysis object of this paragraph.

4.3.1. The fuzzy controller

The HSK prototype employs a Matlab fuzzy model to detect driver's intention with the objective of deciding when it is convenient and safe to activate the rear in-wheel motors to have a positive, negative or null torque. The model has been integrated within the Vehicle Management Unit that determine the Power Split ratio between front and rear wheels. Some specific aspects related to the choice of Power Split ratio will be discussed in the following chapters where the results of simulation studies performed with a longitudinal vehicle model will be presented.
The input considered for the fuzzy set of rules are the variables computed starting from vehicle speed, engine speed and pedal position, acquired from OBD port. Starting from these data, other variables are computed by using the model presented in previous paragraphs (active gear, null gear) and by the vehicle longitudinal model (vehicle torque, engine torque and speed). The output is a positive, negative (braking torque) or null torque to be delivered by the in-wheel motors. Some details on the construction of the fuzzy set of rules (Figure 4.10) are given in the following:

- There are only two membership functions for the first input that are two discrete values, 1 or 0, respectively indicating if the vehicle is or not in gear
- For the second input it is necessary to know if the pedal is pushed or not: in this case the undefined pedal position is due to some casual event, i.e. the pedal is touched accidentally; for this input not equidistant triangular-shaped membership functions have been defined
- Considering the third and the forth input, that are respectively engine and vehicle torque, three functions have been realized corresponding to negative, positive and no torque: in the first two

cases there are trapezoidal-shaped membership functions, while in the last case a triangular-shaped membership function is used to obtain a smoother control around the situation of no torque

- For the last input, the speed, other three trapezoidal-shaped membership functions are used
- Finally, equidistant triangular-shaped membership functions have been defined for the output variable

		OUTPUT: In-wheel motors torque					
		Braking torque (-1)				No torque (0)	Torque (1)
INPUT 1: Gear	Null gear				✓	✓	
	In gear		✓	✓			✓
INPUT 2: Pedal	OFF	✓	✓		✓		
	ON			✓		✓	✓
INPUT 3: Engine torque	Negative			✓			
	No torque						✓
	Positive						✓
INPUT 4: Vehicle torque	Negative	✓	✓				
	No torque						
	Positive				✓		
INPUT 5: Vehicle speed	Low						
	Mean	✓			✓		
	High	✓			✓		

Figure 4.10 - Fuzzy logic rules

Membership function of inputs and output are shown in Figure 4.11-48. The fuzzy inference process is based on the Mamdani method assuming the Fuzzy logical operator 'AND' (i.e. minimum operator). For the defuzzification the center of gravity method has been applied [23]. An example of how the fuzzy controller interprets driver's behavior is the following: in case that the vehicle is in gear, the pedal is on, the engine torque is not negative (positive or no torque), in-wheel motors supply torque. This behavior is reflected by the rules implemented in a mathematical model realized in Matlab.

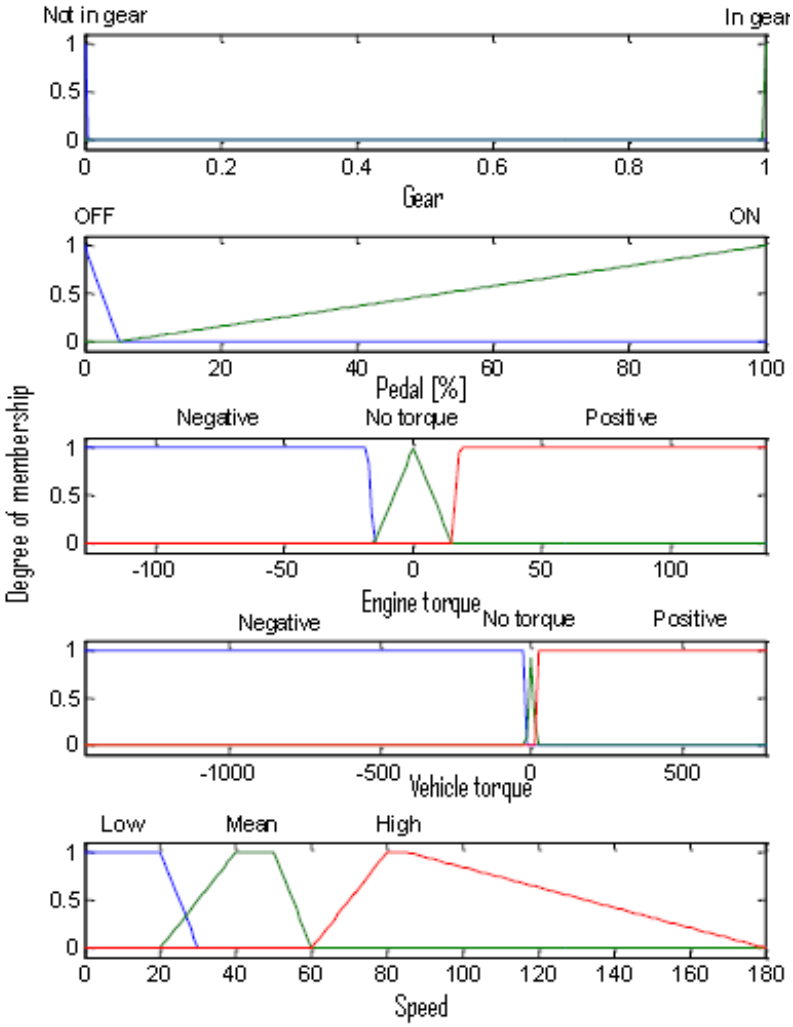

Figure 4.11 - Membership function for controller input

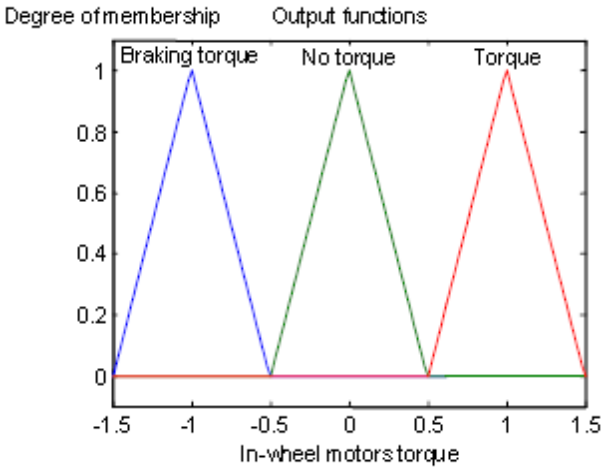

Figure 4.12 - Membership function for controller output

4.3.2. Fuzzy controller results

The model has been validated in off-line mode starting from data measured by the OBD port on a FIAT Grande Punto. Since vehicle speed, in km/h, was available as an integer number, resulting in a significant discretization error at low speed, speed data have been filtered with a zero-phase filter. Typical results are shown in , for a driving cycle in urban conditions, up to 50 km/h. The fifth graph represents engine torque, computed in case that all vehicle power was delivered by front wheels, as in the conventional vehicle. The last two graphs represent the output of the models that are the detected active gear and the output of Driver Intention model. It can be observed that the decision of delivering positive, negative or null torque at rear wheels are consistent with the detected active gear and with pedal position, presented in third graph. The calculation time necessary for this driving cycle (155 seconds) is 2.5 seconds with a pc Intel(R) Core(TM) i7 CPU 920 @2.67GHz, 8183 MB RAM. It seems therefore compatible with its use for real-time applications.

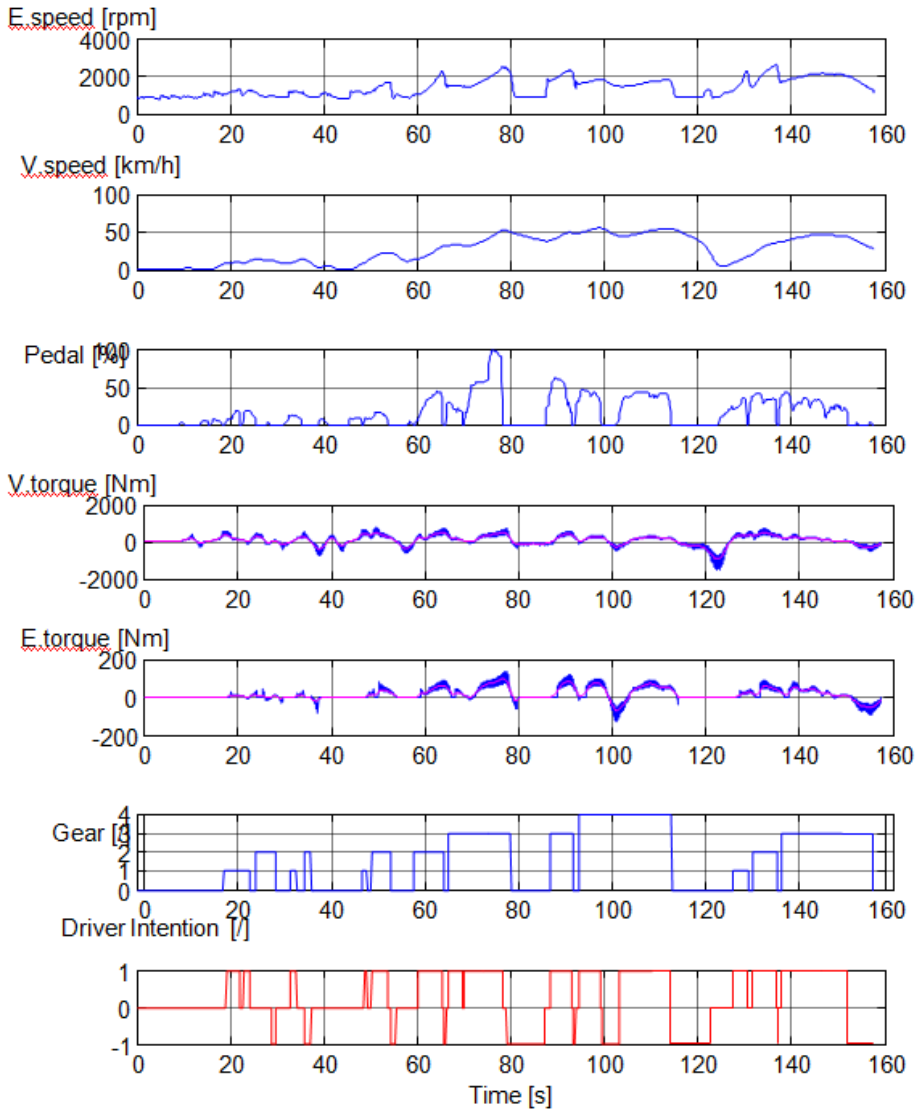

Figure 4.13 - Main experimental results

A first release of the fuzzy control system to detect driver's intention has been implemented in a LabVIEW/Matlab integrated software and tested on the road, on the FIAT Grande Punto with HSK installed. Preliminary tests, performed at limited vehicle speed (below 50 km/h), have shown a regular operation of the main control loop testing the vehicle both in hybrid mode and in electric mode (with engine off and null gear).

4.4 Driver-vehicle interaction

The driver's intention analysis aims to define what is the driver power request; however, even more important is to understand if and how the vehicle satisfies driver's expectations. Because of this reason, a study on driver-vehicle interaction has been carried out.

4.4.1. Model simulation

The presented model simulates interaction between the driver and the car, assuming the power split is constant and equal to 0.5. Vehicle dynamics and driver response are simulated using a longitudinal vehicle model implemented in MATLAB/Simulink and described in 4.1. The simulation requires the driver to achieve a driving cycle ECE-EUDC.

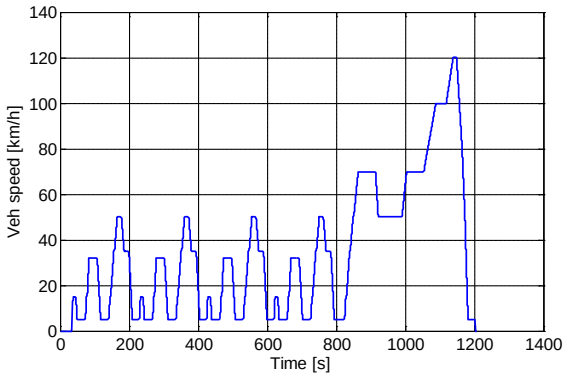

Figure 4.14 - ECE-EUDC cycle

The main sub-models are:

- Internal combustion engine
- In wheel motors ·
- Transmission (driveline): describes the dynamics from the engine to the wheels
- The driver behavior

In particular, the driver is modeled using a PID controller (with zero derivative part) that, considering the difference between realized and the desired speed, generates a power request that will be pulling from either ICE or IWM, or a braking request (obtained through the IWM and the

braking system). The interaction between driver and vehicle can be also implemented by using fuzzy logic or a combination of both [22][24].

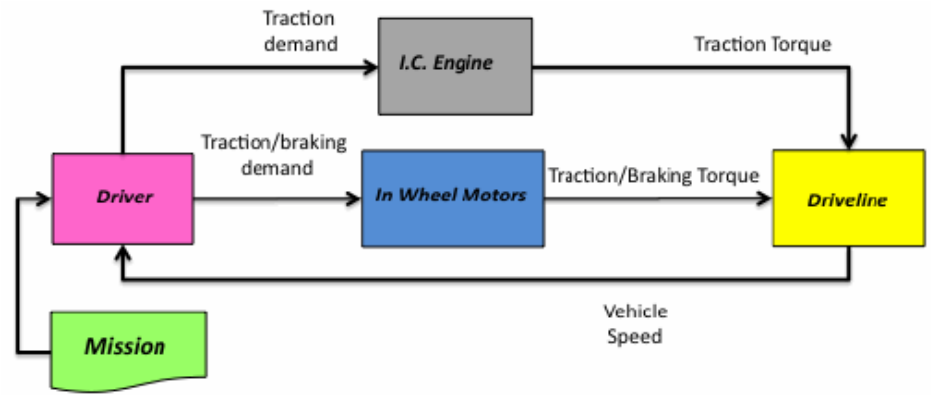

Figure 4.15 - Main sub-models of the simulation model

The model is powered by a hybrid approach: while the transmission is implemented through a dynamic system with one degree of freedom (ignoring the stages of engagement and disengagement of the clutch), the two propulsion systems are represented with black-box data models from the synthesis of experimental data obtained in stationary conditions (maps of torque and efficiency for ICE and IWM). In this way, it is possible to reduce computational time.

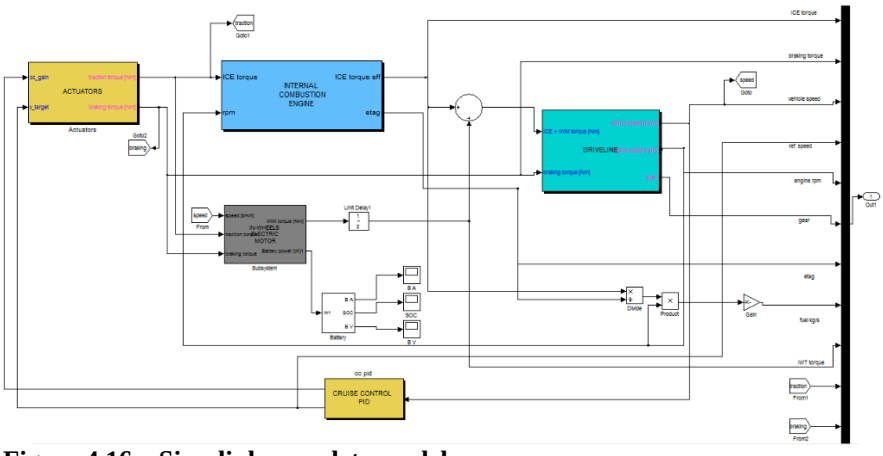

Figure 4.16 – Simulink complete model

4.4.2. The actuation delays

The model described above is based on the assumption that the whole system is able to respond instantly. Therefore, in order to obtain better results closer to reality, they have been introduced into the model some actuation delays and studied their effects on the output of simulations (in particular on the ability of the driver to follow the speed profile imposed). The first delay is inserted downstream of the PID controller in order to take into account the time the vehicle control needs to read the information about the engine (via OBD port) and battery, and then perform calculations necessary to the control strategy.

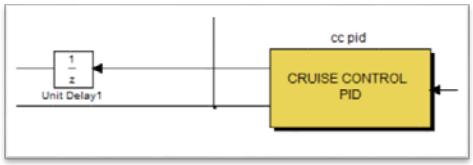

Figure 4.17 - Simulink VMU delay

The second delay, however, is placed immediately after the IWM, since it is due to electrical and mechanical response of IWM.

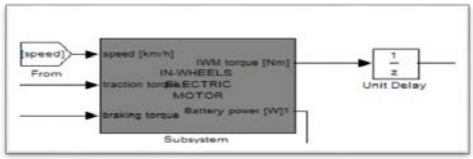

Figure 4.18 - Simulink IWM delay

While the delay of the VMU is on the order of 0.1 seconds (since the reading frequency of OBD port is 10 Hz), IWM delay amounts to approximately 0.01 seconds. In a first moment, the effects of the two delays are calculated separately; their combination results have been calculated as well afterwards. The main factor that has been analyzed is the effect that delays have on the ability of the driver to follow the required speed profile. In order to pursue this goal, a parameter, the irregularity index of Guide (IIG), has been defined and calculated through the following formula, corresponding to observed data set variance:

$$IIG = \frac{\sum_1^n (V_r - V)^2}{n} \tag{4.7}$$

In particular, V is the achieved speed, V_r the desired speed and n the number of collected data. Evidently, the more the IIG increases, the more the driver fails to realize the profile of the reference speed, increasing the differences between V and V_r. As the error is intrinsic to the control system itself, even in the absence of delays, the irregularity index delays is not null. Therefore, to understand the effects of delay, IIG is compared to its value in ideal conditions without system delay (IIG * = 0.2584), i.e. it computes the difference ΔIIG = IIG-IIG *. The simulations have been carried out for increasing values of delay starting from 0.01 up to a maximum value of 3.

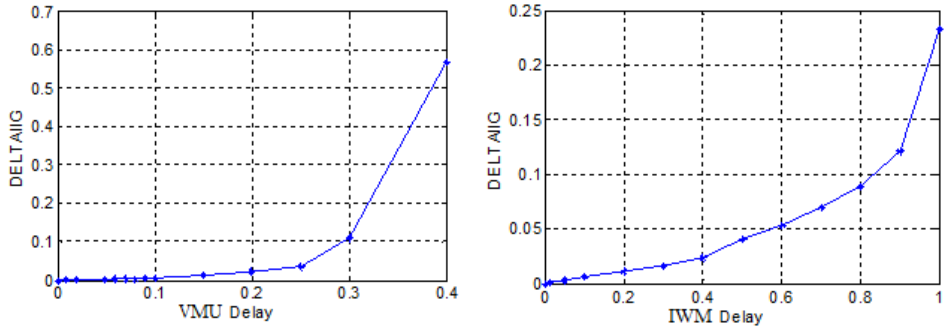

Figure 4.19 - ΔIIG trend for VMU and IWM delays

From the graphics of ΔIIG it is possible to point out that the situation is almost the same for VMU delay until approximately 0.1 value, ΔIIG grows very quickly afterwards. As well as for the ΔIIG, it is possible to observe what happens to torque and pedal gradually increasing the delay:

- Pedal oscillations increasing in frequency and magnitude by time: driver needs to press gas pedal (or brake) more often because vehicle doesn't not respond to his commands immediately;
- ICE torque values higher time by time.

The effect of IWM delay has a negative effect on the regularity of the guide also in this case. Looking at Figure 4.19, the behavior is almost constant until approximately 0.3 value afterwards there is a rapid growth of the ΔIIG: in fact, for a delay of 0.3 seconds the driver is still able to follow enforced speed profile very well. The effect on torque and gas pedal is similar to the previous delay: on one hand, it is possible to reach torque increasingly higher for the ICE, on the other hand gas pedal stroke becomes longer. Although the same phenomena occur, increasing the two delays, VMU delay produces these negative effects much faster than the other one

and therefore it is more critical for the system. What needs to be determined is whether the combination of the two delays produces effects that are an overlap of those or if there is an amplification/reduction behavior. To better understand how the effects combine, the value of IIG has been calculated for several different pairs of delays. At purpose, look at Table 4.1 in which the IIG corresponding to 0.3 delays for VMU and 0.5 for IWM is placed in the intersection of the two boxes (VMU-related delays are represented in red, the others in blue).

Table 4.1 - IIG for combination of IWM/VMU delays

IWM/VMU	0	0,01	0,02	0,05	0,08	0,1	0,3	0,5	0,8	1
0	0,2584	0,2589	0,2595	0,2613	0,2634	0,2650	0,3671	32,0620	73,3933	45,4403
0,01	0,2585	0,2590	0,2596	0,2614	0,2635	0,2652	0,3713	26,0870	71,8870	53,1424
0,05	0,2593	0,2598	0,2604	0,2620	0,2649	0,2662	0,3995	2,8409	23,5116	44,8061
0,1	0,2608	0,2652	0,2619	0,2619	0,2670	0,2677	0,4267	2,5618	61,3566	48,0665
0,2	0,2651	0,2658	0,2664	0,2688	0,2726	0,2740	0,5487	2,8412	22,4498	40,2184
0,3	0,2704	0,2713	0,2723	0,2757	0,2828	0,2845	0,5982	4,1883	72,7450	46,4080
0,4	0,2793	0,2806	0,2820	0,2869	0,2934	0,2990	0,6147	3,6274	22,3830	47,3374
0,5	0,2962	0,2978	0,2995	0,3050	0,3137	0,3169	0,7927	4,0749	62,8145	40,9592
0,6	0,3080	0,3100	0,3122	0,3196	0,3320	0,3373	0,6895	4,0010	64,7245	49,5000
0,7	0,3263	0,3291	0,3321	0,3356	0,3452	0,3433	0,6274	3,8905	24,4414	50,3556
0,8	0,3455	0,3489	0,3524	0,3649	0,3740	0,3865	0,6954	4,9261	23,4488	95,1279
0,9	0,3768	0,3811	0,3858	0,3937	0,4231	0,4299	0,7595	4,0401	26,4247	51,4609
1	0,4897	0,4976	0,5060	0,5371	0,5718	0,5917	0,9540	3,3165	18,2315	48,7930
2	1,8003	1,8217	1,8421	1,9111	1,9895	2,0450	2,3951	5,5330	19,3086	42,0664
3	5,1734	5,1785	5,1833	5,6027	5,6328	5,5959	5,6229	10,1233	33,6402	57,1500

This value should be compared with the sum of the indices corresponding to each delay when it is present alone. A reduction behavior is mainly observed resulting benefits on driving: delays tend to offset each other. In particular, for realistic values of two delays 0.1 (VMU) and 0.01 (IWM), it emerges that the irregularity index is 0.2652 (bold and underlined value), lower than the sum of the indices obtained with VMU delay alone (0.2650) and IWM delay alone (0.2585) (bold values). It correspond to a very low value of the irregularity index with respect to the ideal situation with no

delays (IIG=0.2584, ΔIIG = 0.0068). This result is also consistent with the indications of on road tests, which have evidenced the absence of critical issues related to drivability in various driving conditions and with different drivers for the currently adopted hardware and software solutions on the hybridization system. It can be also observed that when VMU delay is 0.5 or higher, very high values of IIG are found at zero or low values of IWM delay, while the irregularity tends to reduce when IWM delay is higher. This result can be explained considering that when delay of VMU increases the driver is forced to press the pedal more often and more deeply, and this cause high vehicle speed irregularity particularly if IWM reacts promptly to the driver commands, while this effect tend to reduce if also IWM react with some delay.

4.4.3. Model results

A study on the effects of the actuation delays has been performed in order to check the drivability degradation due to different design and control solutions. The simulation with a forward longitudinal vehicle dynamic model, including driver behavior, has pointed out the effects played by the delays of actuation in the main control loop, related to the frequency of data acquisition from OBD or from CAN bus, and by the delays associated to electrical and mechanical response of the in wheel motors. It has been evidenced that these delays have little effects on drivability until 0.2 s, and that the delay on VMU is more critical. The study of combined effects has also shown that delays tend to offset each other, and that for realistic values of the delays the increase in the irregularity index with respect to the ideal case is very limited. Extensive road tests have evidenced the absence of critical issues in terms of drivability for the currently used hardware, so confirming the outcomes of the simulation model.

CHAPTER 5

Control strategies: models and results

As formerly discussed, the motivation behind HEV control system development is that significant fuel saving can be achieved by optimally utilizing the efficiencies of engine and electric motor, whose variations are large across the operating ranges. Formulating the control algorithm for determining the fuel efficient power split between two energy sources is referred to as the supervisory control or energy management problem. In this chapter, after a quick literature review of control strategies, the vehicle model is described and the results in terms of optimal control (Dynamic Programming) and implemented control strategies are shown.

5.1 Literature review

Early research into hybrid powertrains focused on the development of mechanisms for combining two power sources. In [25], a mechanical rotating linkage between parallel running engine and electric motor that operates in a fixed speed ratio was proposed in attempt to reduce emission of atmospheric pollutants. With the development of electronics in the 1980s, microcomputers were introduced for controlling the power distribution and blending between engine and motor [26]. Together with the development of hardware, various control strategies have been proposed. The primary objective of the strategy is minimizing the fuel consumption subject to the charge sustainability of the battery. Earlier approaches utilized intuitive knowledge on engine, motor and battery efficiencies [27][28]. More complex HEV control strategies proposed from mid 1990s can be largely classified into rule-based and model-based approaches, where the latter approaches involved control-oriented vehicle modelling and the implementation of control theories to further exploit potential fuel savings available.

5.1.1. Rule-Based Control strategies

Studies on the rule-based control strategies are an active research area since the mid 1990s. The scope includes a simple set of switching logic control for battery recharge [29] to more complex set of rules [30] that utilize the high low-speed torque characteristic of the electric motor. These rule-based approaches rely on the heuristic knowledge on the vehicle components. Among rule-based control strategies the most important are:

- Heuristic Boolean rules strategies
- Fuzzy rules strategies

Due to its simple control structure and easy implementation, research on Boolean control has continued until very recently. In [31], the authors derive mathematical expressions for the upper and lower bounds on the engine torque within which the engine runs most efficiently as functions of charging and discharging motor efficiencies. The electric motor, which is the auxiliary power source in this case, is driven such that it forces the engine operating point to lie inside the specified envelope. This method of forcing the engine to operate near the peak efficiency region is referred to as load-levelling in [32]. Boolean rules are simple and easy to implement due to low storage and low computation requirements. However, the algorithm is based on the minimal knowledge on the vehicle components and dynamics, therefore it does not fully utilize the potential of hybrid powertrain.

As for fuzzy logic control, it involves the process of putting input and output variables into linguistic variables. This process is called fuzzification and an example of fuzzy logic use has been given for driver's intention analysis in 4.3. However, in that case, the objective was only to decide if IWM had to be activated without taking into account the global energy management optimization which means power split definition according to defined objective function. Early FLC development for an HEV focused on exploiting the efficiency characteristics of the vehicle components. In [33] a FCL based on the efficiency map of the engine is designed. The controller forces the engine to operate near the peak efficiency region to achieve better fuel economy. Three inputs are fed into the controller, which are: driver's command at the pedal, desired motor torque based on the engine efficiency characteristic, and the battery SOC. The inputs are then used to determine the changes in the accelerator command which drive engine to produce greater or lesser torque than the

driver's command, and the motor torque that makes up for the rest of the power demand to be either used to propel or to generate electricity. Similar work is performed in [34] by considering the efficiency characteristics of engine, motor and battery in constructing fuzzy rules. Other FLC have been developed taking into account traffic information and road profile [35], anyway, as more aspects of vehicle and traffic are considered in the FLC design, the number of variables and connecting rules grow, inducing difficulty in tuning parameters. Although different tuning methods heve been proposed such as in [36], carefully tuned FLC is not easily transferable to another vehicle, which is a major drawback of a rule-based control technique.

5.1.2. Model-Based Control strategies

Model-based techniques involve the control-oriented vehicle modelling and the application of control theories to either numerically or analytically solve the torque split commands that minimize the fuel cost criteria.
Among model-based control strategies the most important are:

- Real-time control strategies
- Predictive control strategies
- Dynamic Programming (discussed in 5.3)

Recent model-based approaches focus on the problem of real time applicability of the algorithm by approximating the complete optimal problem solved by a DP approach. One approach that improves practicality is estimating the equivalent fuel consumption of the battery at all points in time and consequently allowing the fuel and electrical energy to be combined in a single cost, which is given by:

$$J_{total}(k(t), \tau_e(t)) = J_e(k(t), \tau_e(t)) + J_{eq}(k(t), \tau_e(t)) \qquad (5.1)$$

where $J_{total}(\cdot)$, $J_e(\cdot)$ and $J_{eq}(\cdot)$ are the total cost, the cost of using engine, and the fuel equivalent cost of electric usage respectively, which are evaluated by the choice of gear ratio, k, and engine torque, τ_e. This cost is then minimized instantaneously at each operating point using the Equivalent Consumption Minimization Strategy (ECMS) [37]. The ability of ECMS to cope with unforeseen future driving behavior has been further improved in [38]. In this work the authors introduce the time-varying weighting factor named equivalence factor, s(t), to account for the future charging /

discharging behavior of the electrical energy, which is reflected in the cost function in the following form:

$$J_{ECMS} = \Delta E_f(t,u) + s(t)\Delta E_e(t,u) \tag{5.2}$$

where $E_f(\cdot)$ and $E_e(\cdot)$ are fuel and electric energy usage respectively.
The ECMS is computationally feasible to apply online but has a weakness in reflecting the fuel-electric dependency at each operating point of engine and motor because it assumes the linear equivalency of the fuel and electric energy obtained by averaging over the whole known drive cycle. Without some level of feed-forward information, the lack of accurate equivalence factor limits the direct applicability of the technique.
The ECMS is alike in a sense that minimizes the Hamiltonian/cost function at each instance in time, while the equivalence factor/costate act as the weighting factor between the engine and motor, and are associated with the battery state of charge boundary conditions. Anyway, in real driving condition, future torque demands and information on the end of a trip cannot be known in advance, hence the equivalence factor which brings the state of charge of battery to the desired level at the end is also unknown. With development of vehicular telemetry devices, researchers have started to look into utilizing the traffic information obtainable from telemetry in HEV torque split control. With telemetry, the ECMS is further improved to suit real-time implementation by introducing prediction algorithm. An adaptive estimator of equivalence factor is added to the ECMS framework, resulting in the ECMS derivatives named Adaptive ECMS (A-ECMS) [39]. Telemetry information may also be utilized in control by providing road topographical profile. In [40], a predictive reference signal generator for the battery state of charge is devised. The use of telemetry is not only limited to previewing of road topography and average speed information along the route, but also it can potentially be used to provide the driving condition ahead so that the future torque demands can be estimated. Within previewed horizon of information, the finite horizon optimal control problem can be solved. The cost function is reformulated to:

$$J_{MPC} = \int_0^T \dot{m}_f dt \tag{5.3}$$

The sliding window of traffic preview allows the finite horizon optimal problem to be repetitively solved, of which the control structure is known as the Receding Horizon Control (RHC) or Model Predictive Control (MPC) [41]. Typically, within each horizon, optimization techniques such as DP and Non linear Programming are used to solve for the optimal control sequence. The use of MPC in HEV control is not only limited to the application with telemetry to provide prediction horizon. It is also used in applications such as the tracking of optimal operating line (OOL) of an engine, in order to improve fuel economy [42]. The OOL is expressed as the predicted state trajectory to follow over a finite horizon. However, in this work, the battery state of charge is not considered.

5.2 Vehicle model

Dynamic programming and model based control strategies implementation, in order to study the hybridized system control and energy optimization, need the definition of the vehicle model. There are two main types of vehicle simulation models, forward/backward simulation model. The two models differ in the path the simulation is taken. In the forward simulation model, the driver model computes the throttle/brake command to follow the specified drive cycle. The power management controller then determines the torque split between engine and motor. The combined torque produced from two sources drives the powertrain, resulting velocity and acceleration of the vehicle which match the reference drive cycle.
The backward simulation model, is obtained by inverting the chain of causality of the forward model. Starting from the drive cycle to follow, the speed and torque relationships are calculated through the powertrain components reversely. With specific required torque and speed at the engine and motor, the fuel consumption and the changes in the battery SOC are computed. Backward-facing models employ quasistatic vehicle model, i.e. individual vehicle component models are based on the steady-state operating condition. Hence, backward-facing models are computationally lighter than differential equations based dynamics models, and also allows simulation with larger time step. However, it has limitations in reflecting the transient dynamics of the vehicle [43]. Since real-time implementability of the controller is one of the aims of this research, a backward model has

been developed. It is slightly different from a conventional parallel hybrid vehicle model because of the TTR structure of the hybridize vehicle.

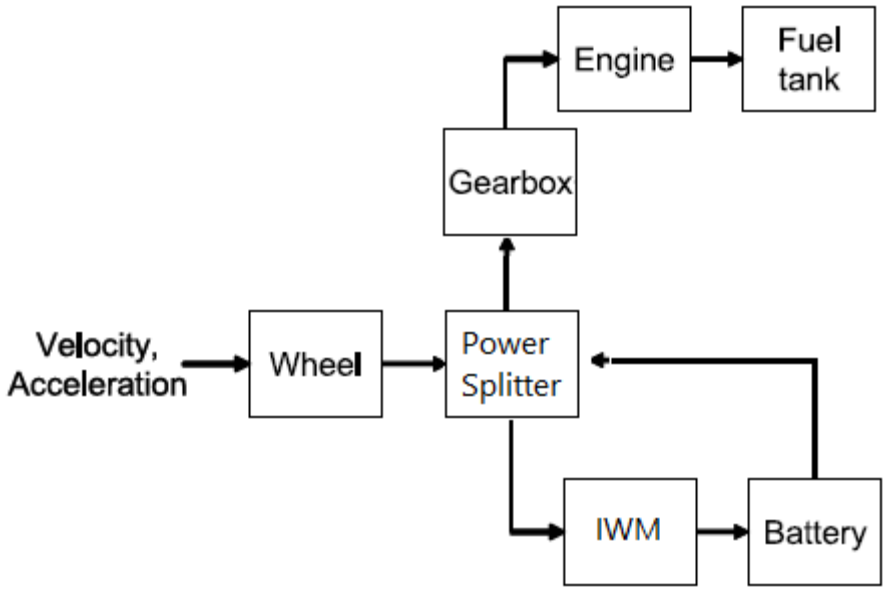

Figure 5.1 - Backward model for the hybridized vehicle

In Figure 5.1, Velocity and acceleration directly come from OBD gate while, in the wheel box, longitudinal dynamic model described in 4.1 is implemented.

5.2.1. Power splitter

The Power splitter is the component which blends the power from engine and electric IWM to produce a combined power output in a TTR parallel HEV. The control strategy is implemented in it. The following relationship holds between input and output variables:

$$\tau_{in} = \tau_t = 2\tau_{IWM} + \tau_{gearbox}$$
$$\omega_{in} = \omega_{out} \quad (5.4)$$

where τ_t is the total combined torque. It is possible to define the power split ratio according to:

$$PS = u = \frac{P_{el}}{P_{tot}} \quad (5.5)$$

Based on the value of u, the mode of operation of an HEV is divided into the following four:

- u = 0, pure thermal mode
- 0 < u < 1, discharging mode
- u = 1, pure electric mode
- u < 0, recharging mode

5.2.2. Gearbox model

Five-speed manual gearbox is considered. Relationship between the input and output speed of the gearbox is given by:

$$\omega_{in} = R\omega_{out} \tag{5.6}$$

where R is the gear ratio defined in 4.2.1, ω_{in} is speed at wheels and ω_{out} is engine speed. The following power relationship holds between input and output power where η_g is the efficiency of the gearbox:

$$\tau_{in}\omega_{in} = \eta_g\tau_{out}\omega_{out} \tag{5.7}$$

where τ_{in} and τ_{out} are the input and output torques of the gearbox respectively. Output speed of the gearbox is proportional to the speed of wheels through the fixed gearing at the final drive.

5.2.3. Internal combustion engine model

With engine torque and speed requested from power splitter, the fuel consumption rate is determined by the following equation:

$$\dot{m}_f = \frac{\tau_e\omega_e}{\eta_e H_i} \tag{5.8}$$

where H_l is the lower heating value of fuel. 42.6kJ/g is used for petrol in this work. Thermodynamic efficiency of an engine, η_e, is represented by a static map indexed by engine speed and torque determined experimentally through steady-state dynamometer testing. Fuel consumption for a given set of torque and speed is calculated by interpolating data points. An example of the engine efficiency contour plot is shown Figure 5.2 - Steady state engine efficiency map.

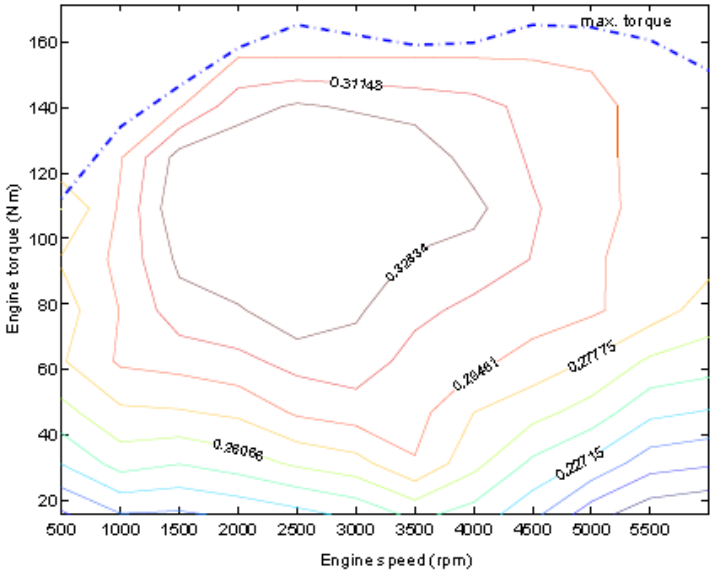

Figure 5.2 - Steady state engine efficiency map

5.2.4. IWM model

An electric motor in an HEV acts as an auxiliary powering device. During charging or braking, the motor is used as generator to produce electricity either from excess engine torque produced or by recuperating kinetic energy of the moving vehicle. Relationship between electric power at the input and output side of the motor is:

$$P_{in} = \frac{P_{out}}{\eta_m} \tag{5.9}$$

where η_m is the electrical energy efficiency.
As in the case of engine, steady state motor efficiency is obtained through dynamometer testing and is stored in a map. Figure 3.5 is an example of efficiency contour plot. Dotted line is the maximum torque enveloping, showing the motor can produce high torques at low operating speed.

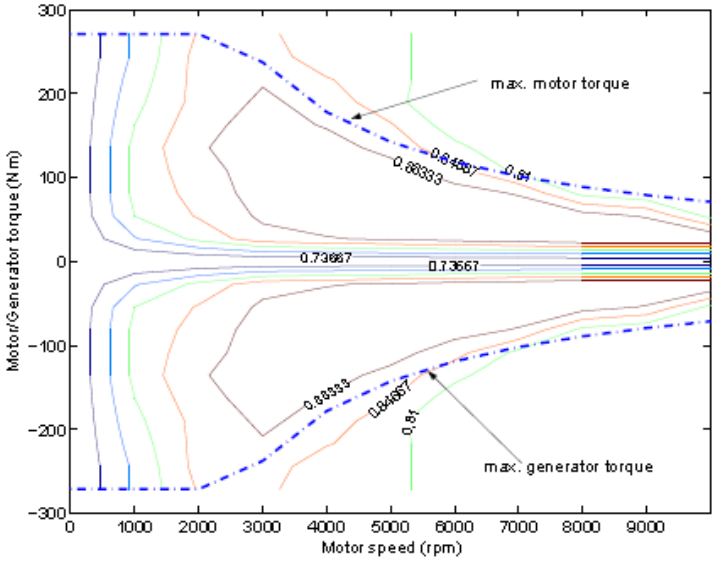

Figure 5.3 - Steady state IWM efficiency map

5.2.5. Battery model

Batteries typically used in hybrid vehicles are either lead-acid, Nikel Metal Hydride (NiMH) or Lithium ion battery. The quasistatic model for all types of battery is based on the equivalent circuit model in Figure 5.4

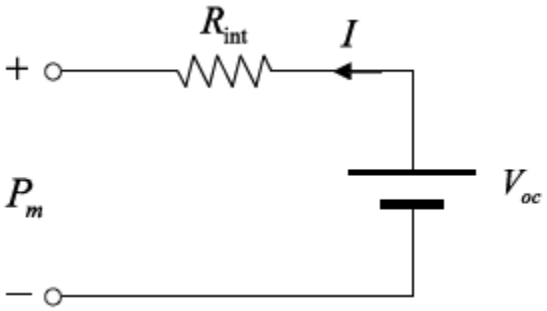

Figure 5.4 - Equivalent circuit of the battery

Power withdrawn from the battery, P_b is calculated by:

$$P_b = P_m + I^2 R_{int} \tag{5.10}$$

where I is the current and R_{int} is the internal resistance and P_m is the power

required by the motor. Internal resistance of a battery is stored in a look-up table indexed by the battery SOC. Figure 3.7 is an example of R_{int} variation with battery state of charge. Within a typical desired operating range of 0.5 to 0.7, R_{int} variation is minimal

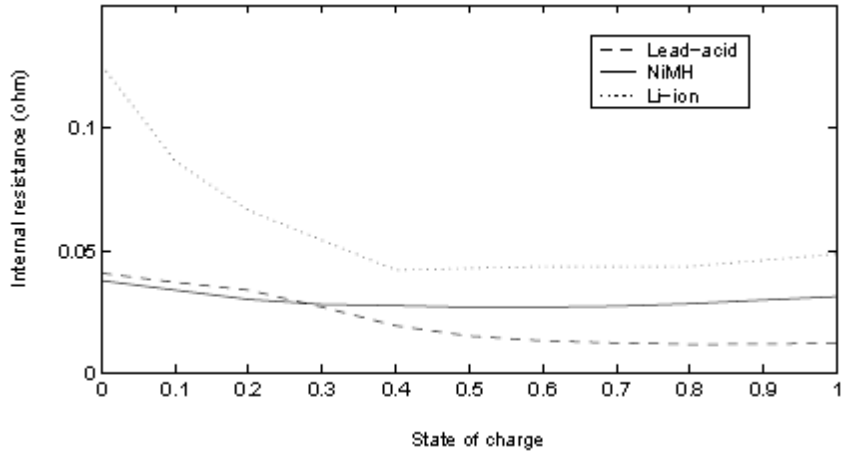

Figure 5.5 - Internal resistance variation with SOC for different batteries type

Current is calculated by:

$$I = \frac{V_{oc} - \sqrt{V_{oc}^2 - 4R_{int}P_b}}{2R_{int}} \tag{5.11}$$

where V_{oc} is the open circuit voltage of the battery, which also varies with the battery state of charge. With current withdrawn from the battery for a duration of 1 second, state of charge, q, is calculated discretely as the following:

$$q(i+1) = \frac{C_{max} - \left[\left(1 - q(i)\right)C_{max} + \frac{I}{3600}\right]}{C_{max}} \tag{5.12}$$

where C_{max} is the maximum battery capacity in Ah.

5.3 Dynamic Programming

Vehicle model defined, it has been possible to apply Dynamic Programming theory [44] [45] for the hybridized vehicle. The benefit of dynamic programming compared to standard optimal control theory is its ability to handle multiple complex constraints on both states and inputs and its low computational burden. The main drawback of the dynamic programming approach is that all disturbances (in the case of deterministic dynamic programming), or at least their stochastic properties (in the case of stochastic dynamic programming) have to be known a priori. Therefore, dynamic programming is often not a useful method for the design of real-time control systems. Only in those cases where the disturbances (or their stochastic properties) are known at the outset, deterministic (or stochastic) dynamic programming can be used in real-time control applications. Nevertheless, dynamic programming is a very useful tool since it can be used to provide an optimal performance benchmark. In the design of a causal real-time controller, this benchmark can then be used to assess the quality of the found controller. Moreover, in some cases the optimal non-realizable solution provides insights in how the suboptimal but realizable control system should be designed.

5.3.1. Dynamic programming implementation results

The main objective of this implementation is to define a benchmark solution, and assess the level of optimality of on-board implementable control strategies with respect to the optimal solution, achievable without constraints in terms of computational time and availability of information. The algorithm has been implemented in Matlab® and employs the optimization function realized by Olle Sundstrom and Lino Guzzella [46]. Please refer to [46] for mathematical formulation of DP algorithm and its implementation. In the analyzed case the cost function is fuel consumption, the state variable is the state of charge SOC, and the control variable is the power split PS: this model will be integrated within the vehicle management unit, which would also determine the power ratio between front wheels (from engine) and the total power demand:

$$PS = \frac{P_{el}}{P_{tot}} \tag{5.13}$$

The main objective is to minimize fuel consumption by acting on the PS, thus determining the SOC, whose initial and final values are fixed (SOCf=SOCi for HEV operation, SOCf>SOCi for PEV operation). To validate the results a simplistic simulator has been developed, employing equations of the vehicle longitudinal dynamics, maps of efficiency of the internal combustion engine and electric motors. The simulator does not have a control module, thus PS is an input. Sample analysis have been performed to assess:

- The benefits of optimized PS(t) vs. constant PS
- The implications on fuel economy of different restrictions on PS

Sample results (driving cycle ECE-EUDC) are shown in Table 5.1.

Table 5.1 - DP sample results (*solutions do not respect the condition SOCi=SOCf)

Scenario	Fuel economy [km/l]
ICE (Diesel) no HSK	20.41
HSK - DP	22.47
HSK – DP with constrained PS (<0.5)	21.33
HSK – DP with PS = 0.5*	40.10
HSK – DP with constrained PS (<0.3)	21.27
HSK – DP with PS = 0.3*	28.78

The results of the hybrid vehicles have been compared with their respective conventional vehicles (CV), and an average fuel economy improvement of up to 10% is obtained. It is worth noting that such results do not take into account the energy contribution provided by the photovoltaic panels. It has been considered possible to adapt this optimization strategy to the prototype due to the data processing time: for a driving cycle of 1200s the optimization is performed in about 50s with a pc Intel(R) Core(TM) i7 CPU 920 @2.67GHz, 8183 MB RAM. The results listed in the above table will serve as benchmark to optimize the logic rules to be embedded in the fuzzy-controller.

5.4 Implemented control strategy

Optimal control strategy has not been implemented yet on prototype control system because of its complexity; anyway, referring to [47], it is possible to note how a constant PS may be an interesting initial condition to make the whole system work. In particular, for small power vehicle, the best PS value is 0.5 as shown in Figure 5.6.

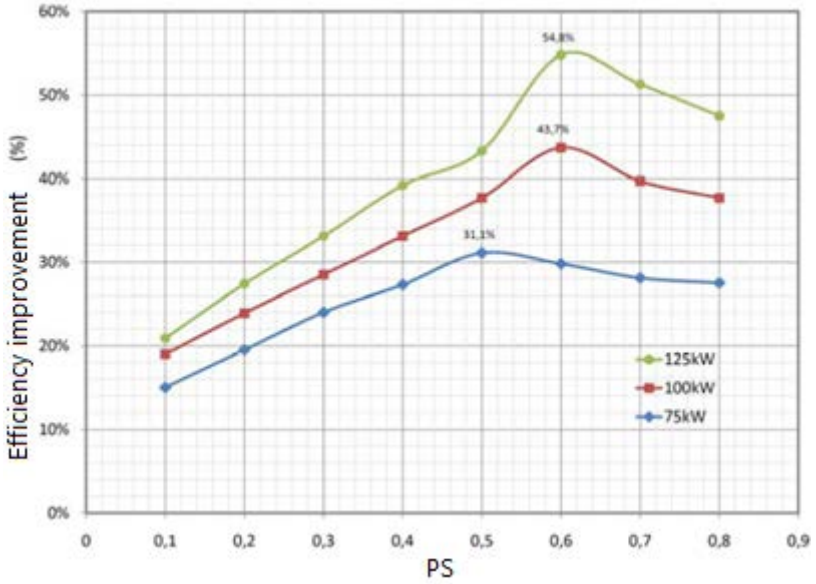

Figure 5.6 - Efficiency improvement as function of PS

This value is also compatible with drivability problem since it affects gas pedal sensitivity in a still acceptable way.
Implemented control strategy flow charts are reported; in particular, propulsion mode, recharging mode and regenerative braking mode are analyzed. Each mode is defined according to driver's intention analysis discussed in Chap.4 and results are shown in terms of fuel economy for real drive cycles.

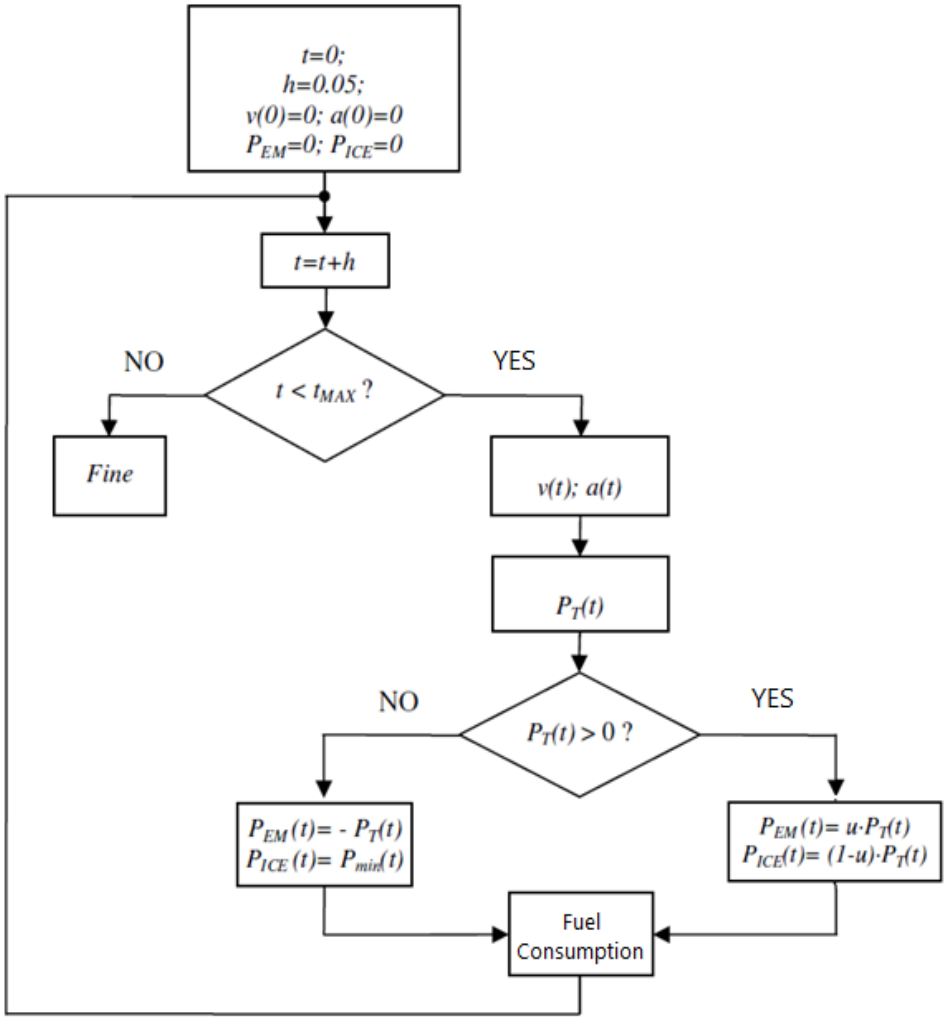

Figure 5.7 – Propulsion and regenerative braking mode flow chart

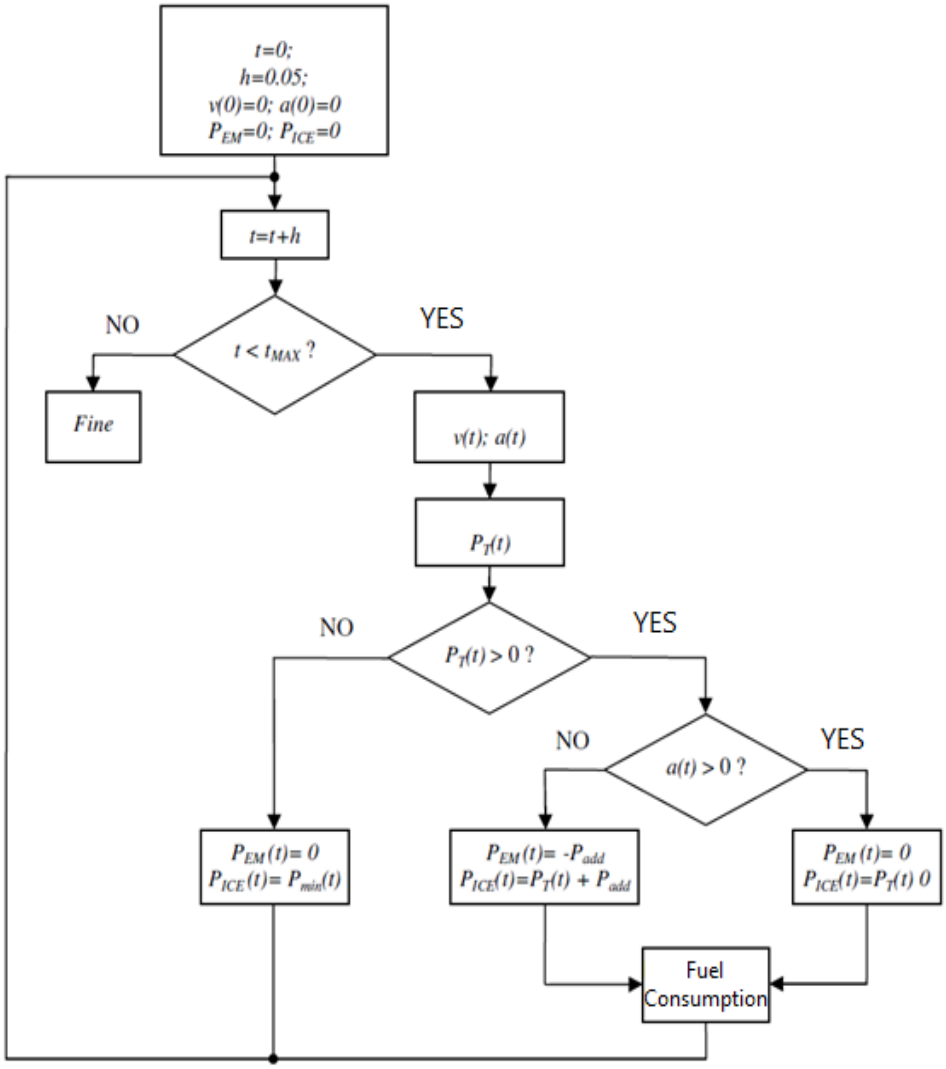

Figure 5.8 - Recharging mode flow chart

A road test has been designed in order to evaluate fuel consumption and economic savings for the implemented control strategy. The road test has been carried out on a 4 km circuit inside University of Salerno campus and considering three different scenario:

- Pure thermal driving mode
- Hybrid driving mode without regenerative braking (case 1)
- Hybrid driving mode without regenerative braking (case 2)

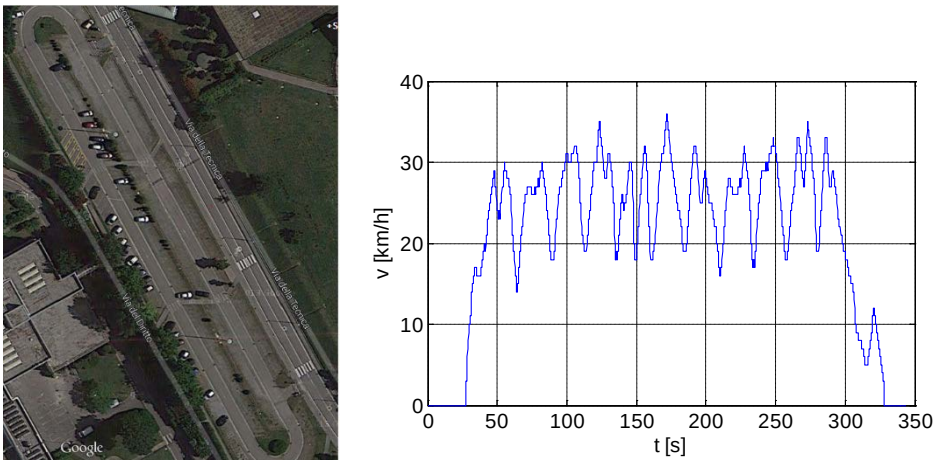

Figure 5.9 – Track and velocity profile for the road tests

For the total cost estimation and control strategy improvements evaluation, the electric power consumption has been evaluated through battery SOC model while fuel consumption has been calculate from engine maps. Fuel cost and electricity cost have been considered to be 1.25 €/l and 0.31 €/kWh respectively. Results are reported in Table 5.2.

Table 5.2 – Cost associated to each driving mode

Driving mode	Fuel consumption [l]	Electric consumption [kWh]	Fuel cost [€]	Electric cost [€]	Total cost [€/km]
Pure thermal	0.30	0	0.375	0	0.094
Hybrid case 1	0.26	0.08	0.325	0.025	0.088
Hybrid case 2	0.24	0.01	0.300	0.003	0.076

From Table 5.2 it is clear the importance of regenerative braking which allows to save a further 13% of the cost per km respect to hybrid mode without it and the 20% compared to pure thermal mode.
Because of this reason, regenerative braking and its control are the object of the following paragraph.

5.5 Regenerative braking control system

The control of regenerative braking starts from longitudinal dynamic described in. During deceleration phases it is possible to calculate the power/torque at wheel which has to be split between front and rear axles. Anyway, negative torque at wheel (which is supposed to be applied by braking system) has to be depurated from driveline passive torque in order to have a better estimation of it.

5.5.1. Driveline torque effect

Power at wheel calculate from longitudinal dynamic can be expressed in terms of torque dividing per wheels rotational speed:

$$T_{wheel} = T_{resw} + M_{eff}\frac{d\omega}{dt} \tag{5.14}$$

Where:

$$T_{wheel} = T_{comb} - T_{brake} - T_{dl}$$
$$T_{resw} = T_{aero} + T_{roll} + T_{mg} \tag{5.15}$$

T_{wheel} is the torque at wheels
T_{aero} is the aerodynamic torque
T_{roll} is the rolling torque
T_{mg} is the torque due to vehicle weight
T_{comb} is the propulsive part of engine torque
T_{brake} is the brakes torque
T_{dl} is the engine/transmission passive torque, which will be indicated as driveline braking torque hereafter. It is important noting that T_{dl} accounts for IWM passive torque due to internal friction too.
During braking phases, there is no propulsive torque from engine, so:

$$T_{brake} = -\left(M_{eff} * \frac{d\omega}{dt} + T_{resw}\right) - T_{dl} \tag{5.16}$$

In order to estimate the braking torque value and how it is split between rear and front axles, it is important to identify the driveline braking effect

(i.e. T_{dl}). Because of this reason, an experimental tests campaign has been carried out making the vehicle reach a target speed and releasing the gas pedal with gear engaged. These tests have been carried out for each gear starting from different target speed. In these conditions, during deceleration tests there is neither torque from engine nor from brakes, thus Equation (**5.16** can be simplified setting $T_{comb}=0$, $T_{brake}=0$, $T_{drive}=0$; furthermore being the road flat $T_{mg}=0$.

$$T_{dl} = -(M_{eff} * \frac{d\omega}{dt} + T_{resw}) \tag{5.17}$$

For each deceleration test, Equation (**5.17** describes driveline braking torque profile that can be expressed as function of velocity once gear is defined. This dependence is expressed for each gear as a polynomial function of vehicle speed. The parameters have been identified by minimizing the error between the driveline torque computed by using experimental data (i.e. velocity profile) according to the right hand side of Equation (**5.17** and the value provided by the polynomial model. Figure 5.10 shows the comparison between the driveline torque estimated by the polynomial regression and the experimental data for the third gear. In Figure 5.11 the driveline braking torque computed for different gear ratios is shown. It is worth remarking that the driveline torque increases by decreasing the gear ratio. This is mainly due to the engine passive torque that increases with engine speed, which is higher for lower gear ratio (once the car speed is fixed).

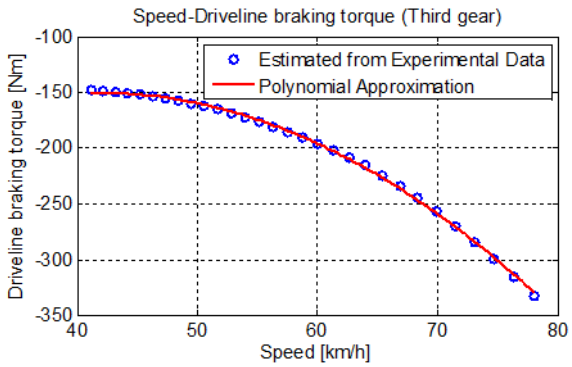

Figure 5.10 - Data-Polynomial approximation comparison

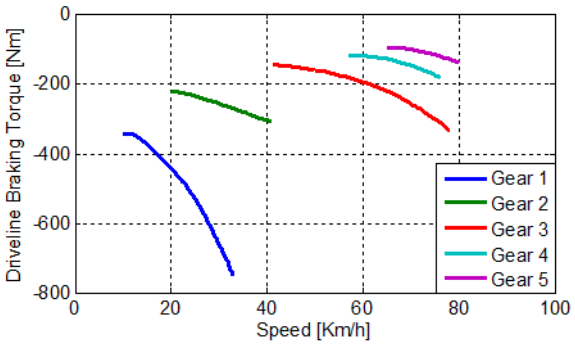

Figure 5.11 - Driveline torque computed for different gear ratio

Using these polynomial functions to identify driveline braking torque for each gear, it is possible to calculate braking torque profile (Figure 5.13) regarding to a real driving cycle through Equation (**5.16**. Speed profile of this driving cycle is shown in Figure 5.12.

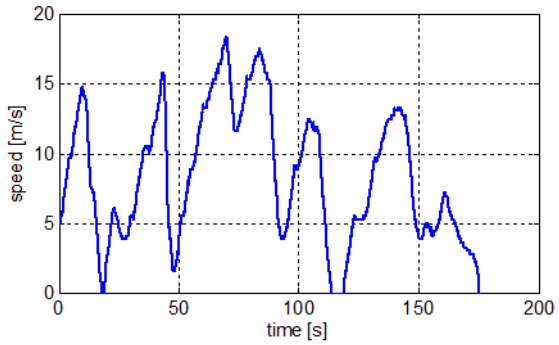

Figure 5.12 - Driving cycle speed profile

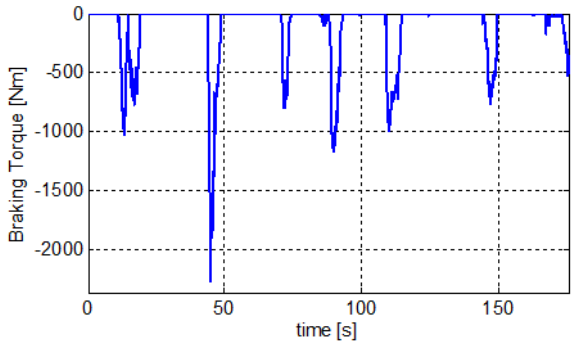

Figure 5.13 - Braking torque profile

5.5.2. Safety braking region definition

In order to analyze how braking torque can be split between front and rear axles, it is also necessary to define a safety-braking region referring to a simplified model of the forces acting on the vehicle described in [48].

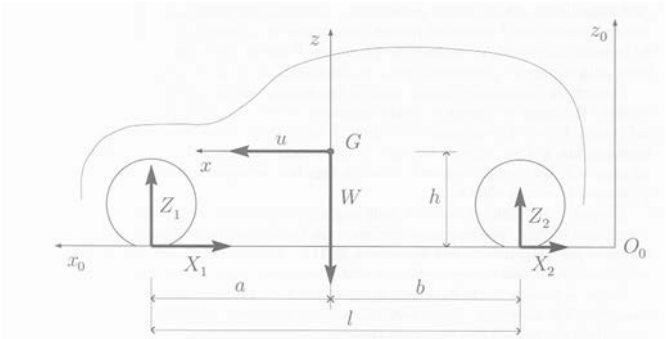

Figure 5.14 - Forces acting on the vehicle during braking

According to the scheme in Figure 5.14:

- X_1 e X_2 are longitudinal forces on front and rear axles respectively
- Z_1 e Z_2 are vertical forces on front and rear axles respectively
- u is the vehicle speed
- l is the distance between front and rear wheels
- a e b are distances between vehicle center of gravity and front and rear axles respectively
- h is the vehicle center of gravity height

- W = mg is the vehicle weight
- G is the vehicle center of gravity position
- X0-Z0 is the street reference system
- X-Z is the vehicle reference system

The proposed model is based on the following assumptions:

1. constant deceleration;
2. flat road;
3. absence of lateral forces;
4. equal adhesion conditions for the wheels on the same axle.

If these assumptions are satisfied, then it is possible to treat the vehicle during braking phases as a "plan system in uniformly decelerated motion" and it is possible to write the relative dynamic equations:

$$\begin{aligned} m\dot{u} &= -(X_1 + X_2) \\ 0 &= Z_1 + Z_2 - mg \\ 0 &= (X_1 + X_2)h - Z_1 * a + Z_2 * b \end{aligned} \tag{5.18}$$

At constant cruise velocity, W1 and W2 are static loads for both axles and can be defined as:

$$\begin{aligned} W_1 &= mg\frac{b}{l} \\ W_2 &= mg\frac{a}{l} \end{aligned} \tag{5.19}$$

During deceleration, load on front axle becomes greater than the rear one according to:

$$\begin{aligned} Z_1 &= W_1 + \Delta Z = W_1 - \frac{mh}{l}\dot{u} \\ Z_2 &= W_2 - \Delta Z = W_2 + \frac{mh}{l}\dot{u} \end{aligned} \tag{5.20}$$

The maximum possible deceleration is obtained when both axles are at grip limit:

$$\begin{aligned} X_1 &= \mu Z_1 \\ X_2 &= \mu Z_2 \end{aligned} \tag{5.21}$$

Substituting these values in the equations of the dynamics of the system:

$$|\dot{u}|_{max} = \mu g \tag{5.22}$$

Combining results, the maximum braking force applied on both axles without slip are:

$$\begin{aligned} X_{1p} &= \mu(W_1 + m\frac{h}{l}\mu g) \\ X_{2p} &= \mu(W_2 - m\frac{h}{l}\mu g) \end{aligned} \tag{5.23}$$

In case braking force is applied only on one axle:

$$\begin{aligned} X_{10} &= \frac{\mu W_1}{1 - \mu\frac{h}{l}} \\ X_{20} &= \frac{\mu W_2}{1 + \mu\frac{h}{l}} \end{aligned} \tag{5.24}$$

In this way it is possible to identify the feasible braking region on plane X2-X1, once defined grip coefficient and car specification.

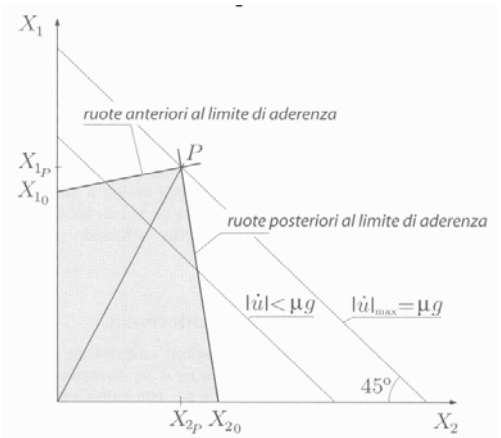

Figure 5.15 - Feasible braking region

The feasible braking region identifies an area where the vehicle brakes

without grip loosing; on the right side of this zone the rear wheels slip, above front wheels lose grip.

5.5.3. Braking control implementation

Once feasible braking region is identified, it is important to develop a control strategy that avoids grip loosing and maximize regeneration. In order to get this result, a regenerative brake controller has been developed; the operating scheme of the controller can be described through the following steps:

- Identifying a braking phase from negative value of T_{wheels}
- Considering the maximum braking torque of in wheel motor corresponding to operating speed in order to maximize regenerative effect
- Calculating mechanical braking torque by subtracting electric torque from T_{brake}
- Identifying feasible braking region and the position of the working point corresponding to the condition listed above
- Assigning this maximum value of in wheels motor control signal if the working point is inside the feasible region

In case this condition is not verified, the controller will assign the maximum value of in wheels motor control signal to set the working point on the right side of the feasible region edge line. Since the total braking torque required by driver must be kept constant, mechanical braking torque will increase and the working point will move upper as shown in Figure 5.16.

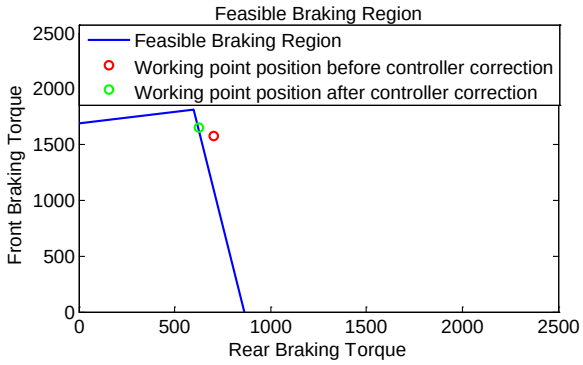

Figure 5.16 - Controller braking modulation effect

The approach explained above is consistent either in case on rear axle there is an electric brake only or mechanical and electric brakes are both installed.
In case of electric brake only, considering maximum in wheels motor control signal, x coordinate of the point is calculated using motor maps only while y coordinate is obtained per difference as already explained above.
On the other hand, considering mechanical braking torque too on rear axle, x coordinate of the point is obtained summing, to maximum electric braking torque from maps, a percentage of the remaining one depending on how mechanical braking is departed (usually 65% front axle, 35% rear axle). Y coordinate of the point is calculated per difference.
This means that the working point in the second scenario is positioned lower and further on the right side compared to the first one since the whole braking torque is constant. The second case is less stressful for front axle brakes since the whole system works on bottom right, but minimizes regenerative braking effect; on the other hand, the first one allows to maximize recovered energy. Unfortunately, when the controller modulates regenerative braking to move to the edge line in the first case scenario, this operation stresses front axle only with the possibility to cross over the top of feasible braking region. However, if that happens, the ABS will operate as in a conventional vehicle in order to avoid front wheels slipping.

5.5.4. Optimal mechanical braking torque distribution

The results of some tests performed on the hybridized prototype developed at the University of Salerno are presented; as previously mentioned, on the back axle of the prototype is not present the mechanical brake but only the regenerative one. The impact of regenerative braking has been evaluated using a real driving cycle whose characteristics are reported in Figure 5.12. Considering the percentage ratio between rear axle braking torque and total braking torque (Rear-Total Torque Ratio, RTTR) for the mentioned driving cycle, it is possible to notice its profile in Figure 5.17 and the comparison with the standard braking distribution (red line). In this case, RTTR is equivalent to the percentage ratio between electric braking torque and total braking torque (Torque Split Ratio, TSR). In this case, most of braking phases are completely covered by electric brakes because of their low magnitude. This means that TSR (RTTR) is often 100% or around this value so that TSR averaged on the whole cycle shows a very high value. In

order to have a better estimation of regenerative braking impact on the cycle, an index of incidence has been defined; this index represents the TSR weighted average (respect to braking torque magnitude).

$$TSR_{wa} = \frac{\sum \left(\frac{T_{brake,elettr}}{T_{brake}} * 100 \right)_n * T_{brake_n}}{\sum T_{brake_n}} \tag{5.25}$$

This configuration allows the maximum regenerative effect (TSR_{wa}=40,5%), however, it leads to a low RTTR during high magnitude braking phases due to limited power of in wheel motors. This means the working point on the feasible braking region moves above the upper edge line twice during the driving cycle and the ABS operates.

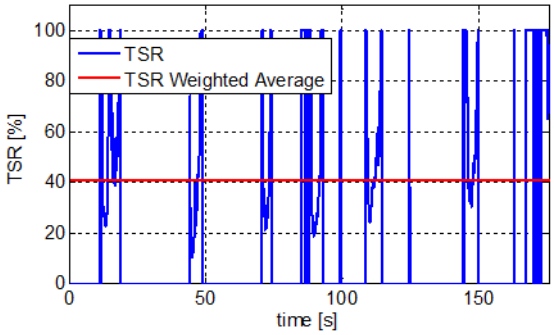

Figure 5.17 – RTTR compared to conventional distribution between front and rear axles (relative to the first case)

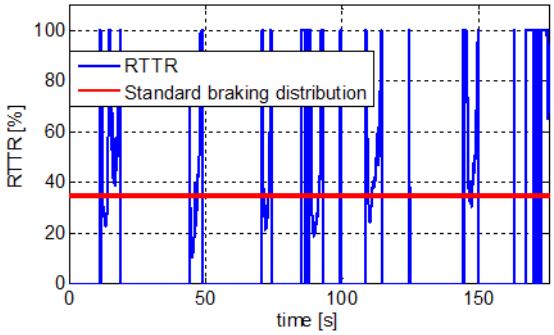

Figure 5.18 - TSR compared to TSR weighted average

To avoid this kind of problems, a configuration that takes into account

mechanical brakes on rear axle coupled with electric brakes is considered. The first case analyzed is the one with a conventional distribution of mechanical braking torque (65% front, 35% rear). Results are shown in Figure 5.19 and Figure 5.20. In this case, the working point is always inside the feasible braking region due to the action of the regenerative braking control system (15 times operating). Anyway, the TSR_{wa} is lower than in the first case as expected (39,8%). This moderate difference is coherent with the small power of IWM installed on the prototype. Increasing IWM maximum power, control system will operate more frequently and TSR_{wa} difference between first and second case will increase.

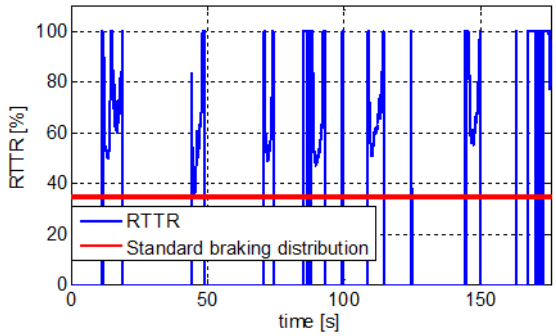

Figure 5.19 - RTTR compared to conventional distribution between front and rear axles (relative to the second case)

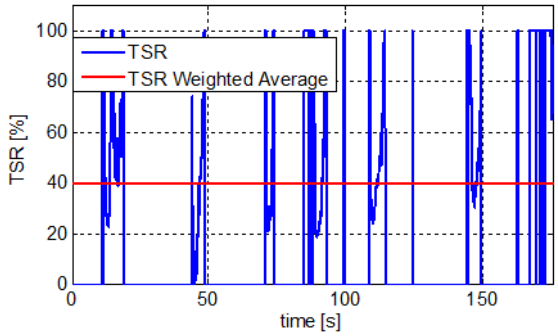

Figure 5.20 - TSR compared to TSR weighted average

In order to find the best solution that maximize TSRwa and keeps the working point into the feasible braking region, the optimization of

mechanical braking distribution has been performed. It comes up the best distribution is 80% on front and 20% on rear axle. Results are shown in Figure 5.21 and Figure 5.22.

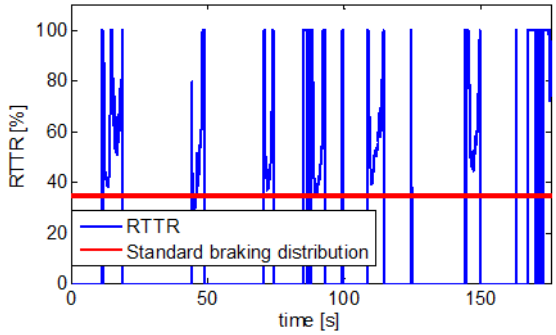

Figure 5.21 - RTTR compared to conventional distribution between front and rear axles (relative to the third case)

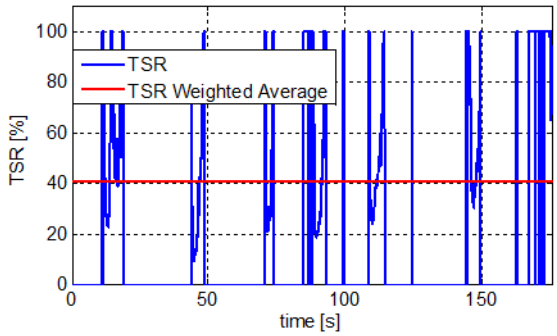

Figure 5.22 - TSR compared to TSR weighted average

In this case there is no grip loosing and the TSR_{wa} is equal to the one in the first case. This happens because it is possible to take advantage of the maximum power of in-wheel motors and, at the same time, the RTTR increases so that braking on front axle, which was critical in the first case, is properly reduced.

The developed model and control strategy can be used to analyze different braking strategies on real road tests, with and without mechanical brakes on rear wheels, in order to maximize the recovered energy by wheel motors and to prevent slipping conditions. The preliminary results show that the model is a useful tool to design real-time braking strategies, if properly combined with estimation of slipping coefficient and use of ABS systems.

CHAPTER 6

Predictive maintenance

The availability of a wide digital information flow from OBD gate coupled with the development and the installation on board of an additional control system (VMU) for the management of the hybridization kit pave the way for their potential use in terms of preventive and predictive maintenance. At this purpose, a methodology for predictive maintenance of vehicles based on telemetry technologies has been defined in order to predict failure events and suggest the actions needed to avoid them for the user safety improvement. The service, as it has been thought, will be able to:

- Acquire, process and analyze vehicle operating conditions data during its daily use by sensors installed on board
- Check the operating conditions, estimate breakdown risks and if maintenance is required
- Notify the user if and what kind of actions are need

The objective of the service is to manage custom maintenance policies, which are parameterized on the timing and the way in which the vehicle is used. Nowadays, the vehicle maintenance is carried out through regular check based on mileage and integrated with the elapsed time from vehicle purchasing. Anyway, they are both very incorrect variables for the estimation of the level of use and functionality of vehicle components since not necessarily related to the real use of the engine, suspensions and all the other vehicle individual parts. On the other hand, the detailed knowledge of the utilization profile of each vehicle makes it possible to predict the life cycles and replacement rates of the main components obtaining a better vehicle management compared to pre-defined maintenance profiles.

6.1 Methodology for predictive maintenance

The computing power and memory available on vehicles, despite its

considerable growth in last years, is by no means comparable to those of desktop computers used for research applications in order to develop models describing the complex mechanics and thermo-fluid dynamic phenomena during engine and vehicle operating conditions. Because of this reason, only black-box models or simplified physical models, which offer lack of precision and difficulty to use advanced diagnostic techniques or prognostic statistics, are implementable. Anyway, in order to improve and increase reliability of the models, it is possible to collect data from a vehicles fleet accessing to a significantly higher information content resulting from a single vehicle increasing, in this way, the probability to achieve acceptable significance thresholds for statistical inferences regarding the diagnostic processes and predictive maintenance. Breakdown events analyzed, technical knowledge from maintainers formalized, appropriate thermo-mechanical stress indexes based on phenomenological models from automotive state of the art defined, correlations between failure events and stress indexes identified and relative statistical significance indexes identified, it is possible to define "alarms" that forecast a failure to prevent the user from it and provide for its preventive repair.
Data detected by the additional control system have a high information content useful to predictive maintenance, as pointed out by the following considerations:

- The knowledge of engine operating variables (speed, torque, airflow, pressure in the manifold, throttle opening, gas pedal position) allows to define the trajectory of the operating conditions and the permanence time in each region of the torque/rpm plan. Starting from various complexity level physical models, it is possible to determine the time history of variables such as temperature of the cylinder wall, maximum temperatures and pressures in the cycle, detonation indexes, thermal flows towards the refrigerant system and the catalyst. In this way, it is possible to define and identify appropriate thermo-mechanical stress indexes in order to verify their correlation with several fault phenomena (valves burn or cylinder head gasket, sealing of the piston rings, water pump breakdown, the degradation of radiator, cooling system, catalyst etc. functionality).
- The knowledge of the vehicle speed signals also allows to go back to the frequency and intensity of the acceleration and deceleration transients and the related gearshift. This information can be related

to the functionality and durability of the transmission components (clutch, gearbox, axle shafts etc.) and the suspensions. Moreover, the braking power can be calculated from longitudinal dynamic and then the brakes and tires wear.

The flow chart of the proposed predictive maintenance methodology is shown in Figure 6.1.

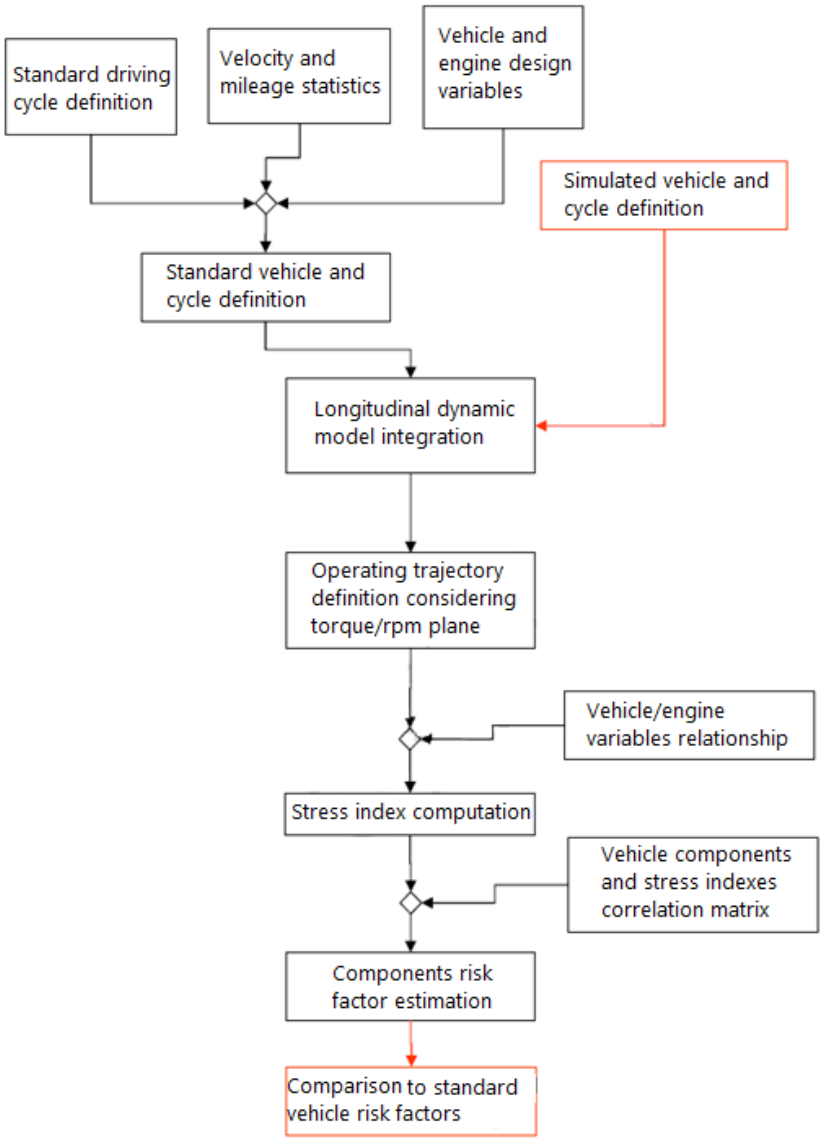

Figure 6.1 – Methodology flow chart

The methodology requires the definition of a suitable "standard vehicle" and its combination with an "average driving cycle", for which are assumed to be valid the maintenance requirements provided by the manufacturer. By affinity and natural integration with HySolarKit project, the Fiat Grande Punto has been chosen as standard vehicle, while, as for the driving cycle, the ECE-EUDC cycle has been selected. Anyway, the methodology can be adapted to the choice of an arbitrary driving cycle.
The variables and the stress indexes calculated for this cycle constitute the reference values with respect to whom the risk factors corresponding to simulated cycles are calculated.

6.2 Stress indexes and risk factors definition

Starting from a given driving cycle, whether simulated or measured, it is necessary to calculate the value of the most important vehicle and engine working parameters (torque, engine speed, vehicle acceleration...) through numerical integration of the longitudinal dynamic model of the vehicle (see paragraph 4.1). The knowledge of the vehicle working parameters for the considered driving cycle allows to define a set of stress indexes reported in Table 6.1.

Table 6.1 - Stress indexes definition

N.	Index	Description
1	Brake_energy	Brake energy
2	Traction_energy	Traction energy
3	Media_power	Mean power
4	Delta_power	Power variation
5	Energy_refrig	Cooling system energy
6	Num_frenate	brake events time number
7	Max_power_brk	Max braking power
8	Rpmeng_max	Max RPM
9	Uso_frizione	Clutch use time number
10	Changes_gear	Gearshift number
11	Index_gear_box	Clutch efficiency

These indexes contribute to the calculation of risk factors, and are related to the functionality of the different parts of the vehicle. The measurement on the field of the wear levels of the components and the knowledge of their respective stress indexes will allow to refine and validate the hypothesized correlation matrix (Table 6.2) and improve the robustness of the methodology.

Table 6.2 - Correlation matrix between stress indexes and vehicle components

	Brakes (1)	**Gearbox (2)**	**Clutch (3)**	**Limber (4)**	**Engine (5)**	**Cooling system (6)**
Brake_energy	0,5					
Traction_energy					0,25	
Media_power					0,25	
Delta_power				1	0,25	
Energy_refrig						1
Num_frenate	0,25					
Max_power_brk	0,25					
Rpmeng_max					0,25	
Uso_frizione			0,5			
Changes_gear		1				
Index_gear_box			0,5			

The stress indexes and the risk factors are expressed as time function and the last ones are assumed to be increasing variables. Through the time computing of stress indexes and using the correlation matrix shown in Table 6.2, it is possible to have an overview of the risk factors variability during the ECE-EUDC cycle. As can be noted from reported graphs (Figure 6.2 Figure 6.3), the stress indexes show an increasing but not uniform trend. Some of them vary continuously (IS2, IS3, IS4, IS5), while others have step variations (IS1, IS6, IS7, IS9, IS10) because related to discrete events (braking, gearshift). Consequently, the related risk factors show continuous variation (limber, engine and coolant system) or step increase (brakes, transmission and clutch).

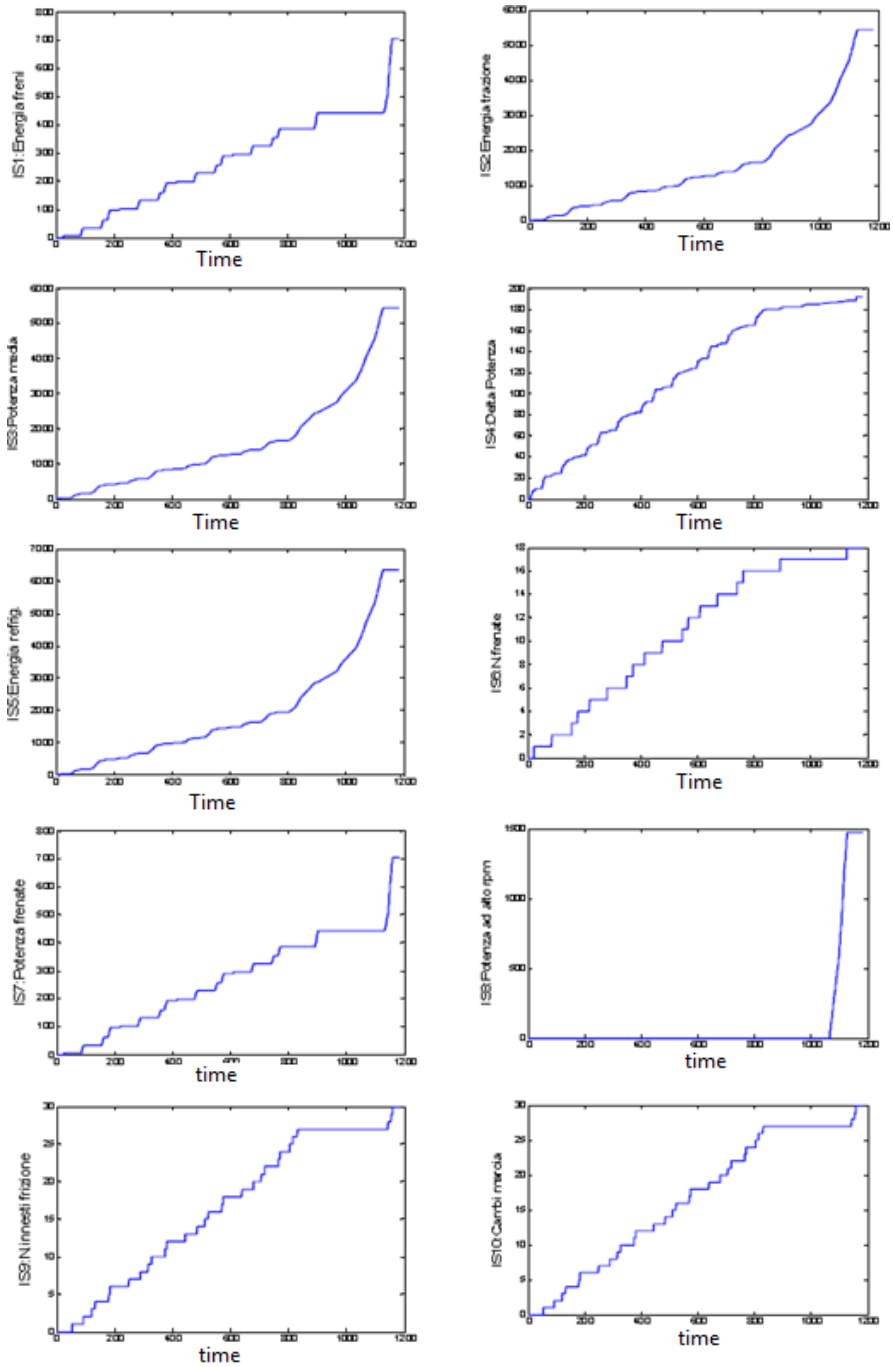

Figure 6.2 - Stress indexes for ECE-EUDC cycle

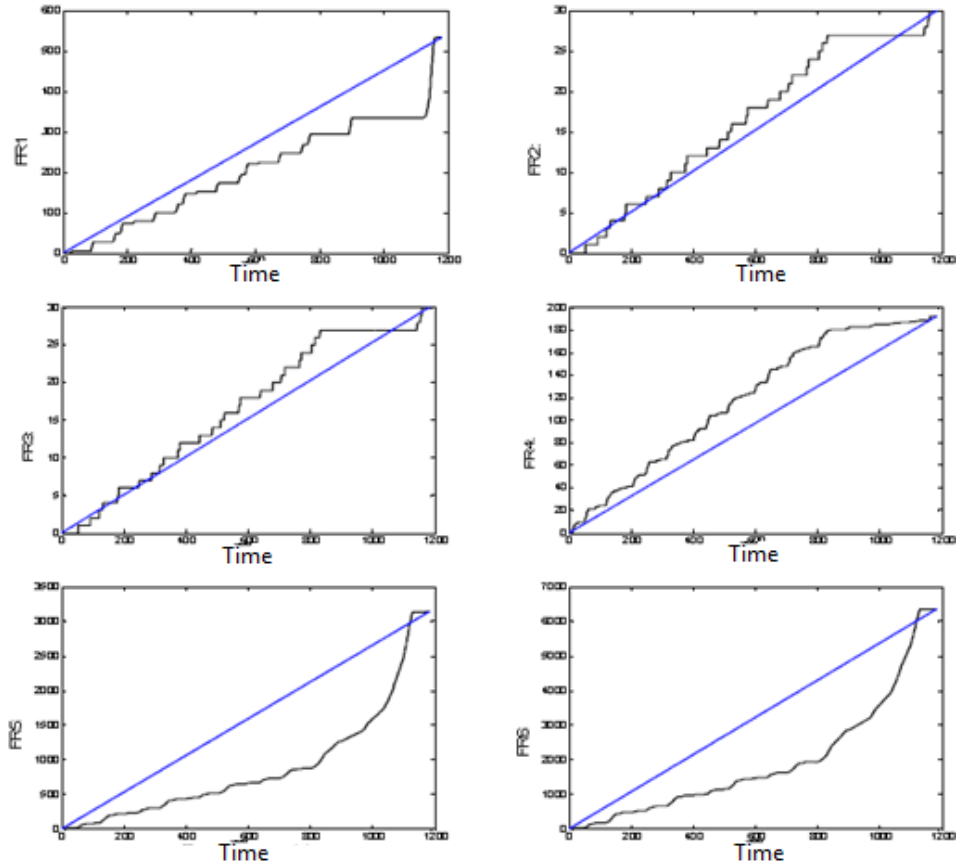

Figure 6.3 – Risk factors for ECE-EUDC cycle

In order to estimate the stress indexes variability, and the corresponding risk factors, it is necessary to calculate their statistical properties such as the mean value and the standard deviation (whose square is the variance) [49]. For a sample of n observation, the mean value is defined as:

$$\bar{x}_n = \frac{1}{n}\sum_{i=1}^{n} x_i \tag{6.1}$$

While the variance σ^2 can be calculated as:

$$\sigma_n^2 = \frac{1}{n-1}\sum_{i=1}^{n}(x_i - \bar{x}_n)^2 \tag{6.2}$$

These two equation, however, are not useful when it is necessary to periodically update such variables, because it would involve the necessity to store (or transmit) long measured data sequences with memory commitment. In such circumstances, it is preferable to use relationships that allow to calculate the mean value and variance recursively starting from the previous estimation and from the current observed value according to:

$$\begin{aligned} \bar{x}_n &= \frac{n-1}{n}\bar{x}_{n-1} + \frac{1}{n}x_n \\ \sigma_n^2 &= \frac{n-1}{n}\sigma^2{}_{n-1} + \frac{1}{n-1}(x_n - \bar{x}_n)^2 \end{aligned} \tag{6.3}$$

In this way it is necessary to store only 3 variable values:

$$n \;\; \bar{x}_n \;\; \sigma_n^2$$

The risk factors (FR) are calculated as the weighted average of the corresponding stress indexes IS_i through α_i coefficients:

$$FR = \sum_{i=1}^{k}\alpha_i IS_i \tag{6.4}$$

Because of linear functions properties [49], the average value and the variance of the risk factors may be calculated as a linear combination, starting from the corresponding mean and variance values of the stress indexes, according to following relations:

$$\begin{aligned} \overline{FR} &= \sum_{i=1}^{k}\alpha_i \overline{IS}_i \\ \sigma_{FR}^2 &= \sum_{i=1}^{k}\alpha_i \sigma_{IS_i}^2 \end{aligned} \tag{6.5}$$

As for the statistic variability index Δ, it is defined as the average value of the difference between the variable risk factor v_i (black line) and its trend value (blue line) reported in Figure 6.3.

$$\Delta = \frac{\sum_t |v_i - v_m|}{t_{ciclo}} \tag{6.6}$$

On the other hand, the relative variation index is expressed as the percentage ratio of Δ and the trend value v_m at the end of the cycle:

$$\Delta_p = \frac{\Delta}{v_m(t_{ciclo})} * 100 \tag{6.7}$$

The risk factors values and their upper and lower limits are estimated linearly extrapolating respect to the chosen time for forecasting:

$$V_t = \frac{v_m(t_{ciclo})}{t_{ciclo}} * t$$
$$V_{t,sup} = \frac{v_m(t_{ciclo}) + \frac{\Delta}{2}}{t_{ciclo}} * t \qquad V_{t,inf} = \frac{v_m(t_{ciclo}) - \Delta/2}{t_{ciclo}} * t \tag{6.8}$$

The extrapolation results obtained for a time corresponding to 15000 km are reported in Figure 6.4.

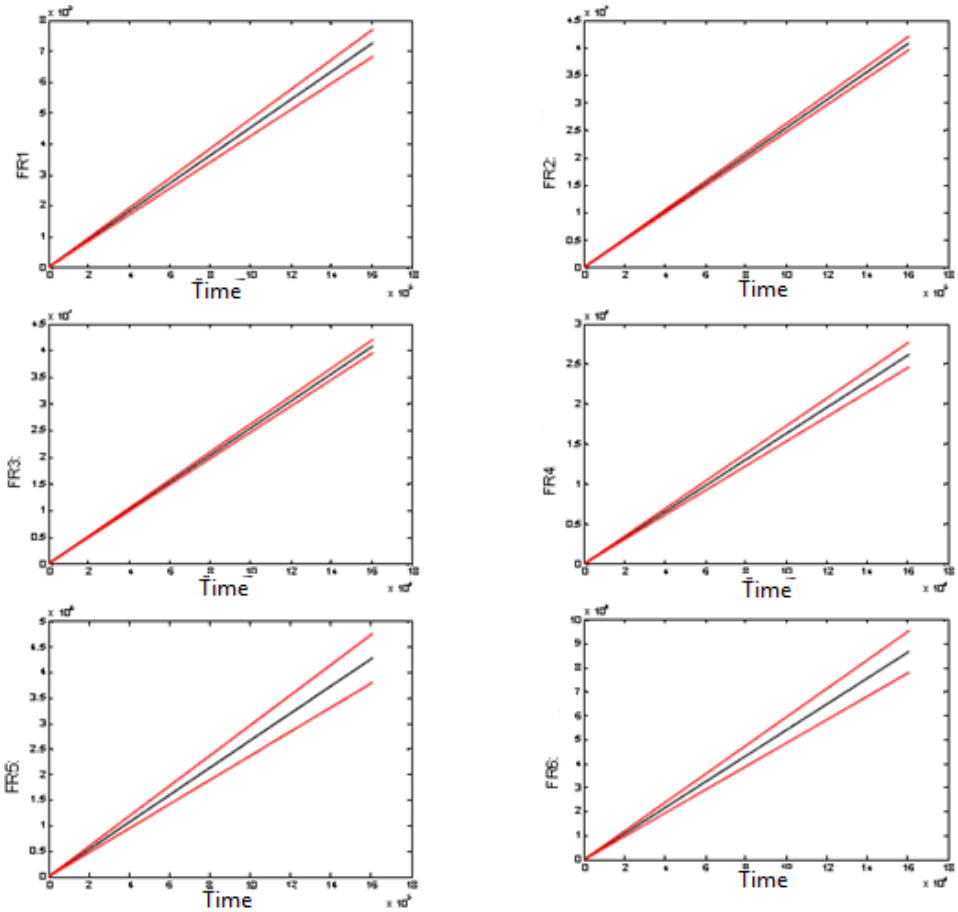

Figure 6.4 - Risk factors and variability estimation up to 15000 km

6.3 Methodology validation

In order to test and verify the proposed methodology, six different driving cycles have been defined, characterized by different speed, time and mileage to reflect the most common driving condition. In order to realistically simulate the vehicle use, it has been decided to carry out "on the road" tests to relieve necessary information. The defined driving cycles typology are: highway (1), city (2), traffic (3), mixed (4), sport (5) and track (6) and their characteristics in terms of duration, mileage and average speed

are reported in Table 6.3 and compared to ECE-EUDC cycle (Rif.).

Table 6.3 - Cycles characteristics

Cycle	Rif	1	2	3	4	5	6
Time	1180	1312	1133	900	1180	1180	480
mileage	11,43	43,74	18,91	6,00	19,66	35,77	16,12
Average speed	38,8	119,9	58,5	24,0	60,0	109,0	120,6

Data acquired for each driving cycle have been processed to calculate through the longitudinal dynamics model the related stress indexes (Table 6.1). Their values have been compared to the reference for the ECE - EUDC (assumed to be 1) obtaining, in this way, the relative stress indexes reported in Table 6.4.

Table 6.4 – Relative stress indexes for each driving cycle

Index	CYCLE						
	Rif	1	2	3	4	5	6
Brake_energy	1	0,88	0,22	1,62	5,33	1,39	0,21
Traction_energy	1	1,86	0,81	0,83	1,66	1,92	1,97
Media_power	1	1,19	1,37	1,36	6,82	2,07	1,16
Delta_power	1	0,25	-33,68	17,97	-32,78	1,54	-43,83
Energy_refrig	1	1,51	0,78	1,34	1,75	1,92	4,67
Num_frenate	1	0,15	1,14	1,27	2,26	0,57	0,16
Power1_max_	1	6,70	0,75	0,70	6,14	4,44	1,50
Rpmeng_max	1	0,83	0,71	0,47	0,82	1,17	0,93
Uso_frizione	1	0,14	0,36	3,05	1,43	0,68	0,19
Changes_gear	1	0,14	0,36	3,05	1,43	0,68	0,19

Starting from the correlation matrix (Table 6.2) the relative risk factors associated with different components of the vehicle engine and body have been calculated: brakes, gearbox, clutch, limber, engine and cooling system. As expected, the braking system is the most stressed in the "Mixed" cycle, while the "Traffic" cycle further urges the gearbox , the clutch and the limber (in terms of positive acceleration); the "Track" cycle , however, is most critical for decelerations regarding the limber, the engine and the cooling system. The results concerning the calculation of the risk factors for each cycle are shown in Table 6.5.

Table 6.5 - Relative risk factors for each driving cycle

Components	CYCLE						
	Rif	**1**	**2**	**3**	**4**	**5**	**6**
Brakes	1	0,87	0,23	1,61	5,29	1,38	0,21
Gearbox	1	0,14	0,36	3,05	1,43	0,68	0,19
Clutch	1	0,14	0,36	3,04	1,43	0,68	0,19
Limber	1	0,25	-33,68	17,97	-32,78	1,54	-43,83
Engine	1	1,86	0,81	0,83	1,66	1,92	1,97
Cooling system	1	1,51	0,78	1,34	1,75	1,92	4,67

During tests, no breakdown events have been registered to compare their occurrence to the model forecasting because of the short time last. Of course, for the complete model verification, considering its heuristic nature, a relevant tests campaign has to be designed. Furthermore, this operation will allow to verify and improve the initial hypothesis regarding stress indexes and risk factors correlation which, despite being based on physical grounds and engineering considerations, brings with it a certain degree of subjectivity. In this way, and considering the possibility to verify the components wear during maintenance and replacement operations, the estimation of the functional relationships between stress indexes and risk factors will occur with an adaptive methodology. Another question deal with the choice of the stress indexes which may be not unique. In order to remove variables that may not have sufficient information content, because strongly related to the others, a correlation analysis has been carried out. Finally, the application of the methodology on the vehicle requires the estimation of some variables such as the vehicle mass, the road slope, the wind speed and engaged gear. Appropriate identification techniques need to be developed for the estimation of these quantities from vehicle measured data as for the engaged gear detection described in 4.2.
In this chapter, the developed methodology and its partial validation has been reported while its calibration and optimization, online implementation and user interface development, because of the large amount of data to be processed, will be the object of future works.

CHAPTER 7

Turbo-compressor models for automotive engines

If hybrid electric vehicle development is currently the most followed trend in order to reduce CO_2 emissions and increase the powertrain efficiency, on the other hand, research on engine downsizing and super/turbocharging can be considered as the most important alternative to it. In particular, several charging technologies are being explored to improve the performance and transient response of the engine, including turbochargers, mechanical superchargers, electrically-assisted turbochargers and multi-stage systems. Numerous studies have focused on the opportunities and technical issues of engine downsizing and charging (for instance [50][51][52]) indicating fuel economy improvements of up to 10% over regulatory drive cycles [53][54][52]. A key challenge for achieving the desired fuel economy benefits lies in optimizing the design and control of the engine boosting system, which requires the ability to rapidly sort different design options and technologies in simulation, evaluating their impact on engine performance and fuel consumption. Design optimization studies are currently performed in the automotive industry by relying on high-fidelity engine system simulators, such as GT-Power. These models solve the 1D compressible flow equations in the air path systems to determine the pressure and flow rates at different steady-state and transient operating conditions. Simulation of turbocharged engines requires however to import the characteristic maps of compressor and turbines, which are usually provided by the suppliers and are considerably limited in the number of available data points. Therefore, for engine system simulation it is often necessary to develop models that reasonably extrapolated the available data and provide a representation of the turbocharger behavior at off-design conditions (such as at engine idle or low load points) [53][55]. The use of behavioral models to extrapolate the flow and efficiency maps of automotive turbochargers is a common practice and several approaches

have been proposed. On the other hand, the objective of developing virtual design studies, where the design of the engine air path system behavior is optimized in simulation, requires the ability to model the behavior of compressors and turbines while varying their key design parameters, typically related to the geometric features of the stator and rotor. Today, this is only possible if a large database of characteristic maps is available, which is not always possible. Furthermore, importing all of the different maps into an engine system simulator, and extrapolating the data outside of the experimental region is extremely time consuming. To this extent, a model-based approach to predict the characteristic maps of automotive turbocharger components when varying their most common design parameters has been developed. Specifically, the scalable modeling methodology relates the flow and efficiency of compressors and turbines to their key parameters such as the diameter, Trim and A/R ratio. This approach makes it possible to model the behavior of a family of several turbocharger configurations varying their geometry, starting from only a few sample characteristic maps.

7.1 Scalable modeling approach

The starting point for this study is a set of turbocharger maps that was made available by a leading automotive supplier for a family of compressors and turbines. The maps were obtained to cover a range of design parameters, particularly the rotor diameter, the Trim and the A/R ratio, which are defined in Equation (**7.1**) and Figure 7.1.

$$T = \frac{d}{D}$$
$$\frac{A}{R} = \frac{A_{cs}}{R_{cl}} \tag{7.1}$$

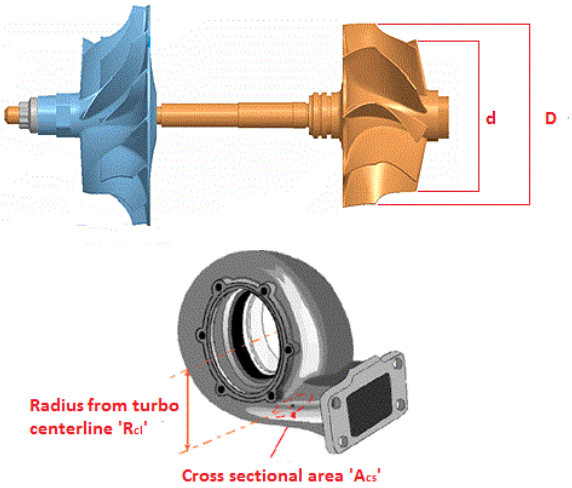

Figure 7.1 - Main Design Parameters Defining Turbocharger Compressors and Turbines

According to the dimensional analysis theory, it is possible to introduce dimensionless variables to reduce the number of overall variables representing a physical experiment. According to this theory, the general way to represent the (dimensional) performance of a centrifugal compressor or radial inflow turbine is given by:

$$p_{out} = f(\dot{m}, p_{in}, T_{in}, \gamma, N, \upsilon, D, l_1, l_2 \dots)$$
$$\eta = g(\dot{m}, p_{in}, T_{in}, \gamma, N, \upsilon, D, l_1, l_2 \dots) \quad (7.2)$$

where p is the pressure, $\dot{m}$ the flow rate, T the temperature, N the rotational speed, γ the specific heat ration, υ the kinematic viscosity, and D, l_1, l_2 represent design parameters that influence the performance. According to the π- theorem, if there are n variables and m fundamental units, the equation relating the variables can be expressed in terms of n-m dimensionless groups, leading to:

$$\frac{p_2}{p_1} = f\left(\frac{\dot{m}\sqrt{\gamma R T_1}}{p_1 D^2}, \frac{ND}{\sqrt{\gamma R T_1}}, \gamma, \frac{ND^2}{\upsilon}, \frac{l_1}{D}, \frac{l_2}{D}, \dots\right)$$

$$\eta = g\left(\frac{\dot{m}\sqrt{\gamma RT_1}}{p_1 D^2}, \frac{ND}{\sqrt{\gamma RT_1}}, \gamma, \frac{ND^2}{\upsilon}, \frac{l_1}{D}, \frac{l_2}{D} \dots\right) \quad (7.3)$$

The equation above can be further simplified considering that geometrically similar turbomachinery where the last two terms are nearly constant, by neglecting the influence of the working fluid and Reynolds number on the characteristic curves, and by assuming that only one specific machine is modeled (hence, removing the dependence of the π-terms containing the design parameters). These approximations lead to the well-known dimensionless representation of the characteristic curves for compressors and turbines [50].
These equations define the starting point to study the influence of design parameters on the characteristic maps, specifically through the analysis of different characteristic maps of compressors and turbines. The proposed approach for developing a scalable model starts from a set of semi-physical models predicting compressors and turbine maps. These models, illustrated in the following sections, have been proposed in literature and are generally well accepted for engine system simulation and control-oriented applications. The developed control-oriented models have been first calibrated on the maps of different compressors and turbines. Then, the models have been converted to dimensionless form to extract the influence of the π-terms related to the design parameters on the calibration parameters of the models. The outcome of this process is a set of analytical and empirical correlations that scale the flow and efficiency maps based upon dimensionless groups depending on the A/R, Trim and Diameter.

7.1.1. Compressor mass flow rate model

The scalable compressor flow rate model developed is based on the control-oriented model proposed by Jensen and Kristensen [56][57], which will be referred to as the JK model in the following discussion. According to this model, the compressor flow rate is predicted through a semi-empirical correlation expressed in terms of dimensionless variables, namely the head parameter Ψ, the flow parameter Φ and the blade Mach number Ma:

$$\Psi = \frac{K_1 + K_2 \Phi}{K_3 - \Phi}$$

$$K_i = K_{i1} + K_{i2} Ma + K_{i3} Ma^2 \quad (i = 1,2,3) \tag{7.4}$$

The dimensionless parameters are defined as:

$$\Psi = \frac{c_p T_{ref} (\beta^{\frac{\gamma-1}{\gamma}})}{\frac{u_2^2}{2}}; \quad \Phi = \frac{\dot{m} R T_{ref}}{\frac{\pi}{4} p_{ref} D_2^2 u_2^2}; \quad Ma = \frac{u_2}{\sqrt{\gamma R T_{ref}}} \tag{7.5}$$

where D_2 is the impeller diameter and u_2 the impeller blade speed. The parameters K_{ij}, are identified on the compressor flow maps through a least-square fitting [56]. The JK model is used as a starting point to define a scalable model for the compressor flow maps. To this extent, the model has been identified on 6 different compressors, whose key design data are listed in Table 7.1. The remaining compressor maps (listed in Table 7.2) have been later used for model validation. As an example Figure 7.2-Figure 7.4, show the result of the identification of the JK model on the characteristic map of one compressor, illustrating the agreement with the experimental data, as well as the functional relation of the three parameters with the Mach number. As evident from Equation (**7.4**)-(**7.5**, the JK model depends only on the impeller diameter, through the definitions of the dimensionless variables. The influence of the other parameters (A/R and trim), which is not immediately evident in the above model, could be elucidated by analyzing the structure of the above model, and how it correlates with the operation of a centrifugal compressor at limit conditions.

Table 7.1- Data of the six compressors used for model calibration

Compressor	***Diameter***	***TRIM***	***A/R***
C1	56	50	56
C2	52	55	52
C3	52	50	52
C4	52	45	52
C5	60	55	60
C6	60	45	60

Table 7.2 - Data of the three compressors used for model validation

Compressor	*Diameter*	*TRIM*	*A/R*
C7	60	50	60
C8	56	55	56
C9	56	45	56

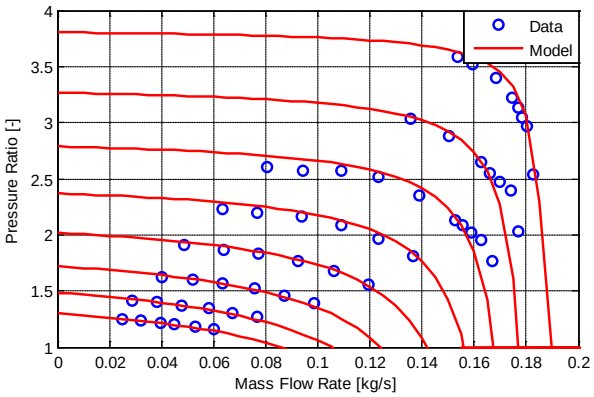

Figure 7.2 - Results of JK Model identified on a compressor map (Data from compressor C1).

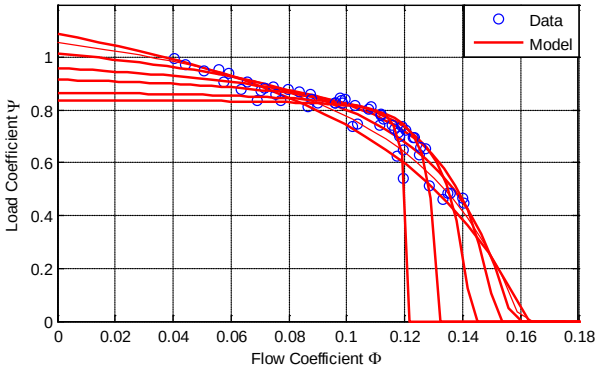

Figure 7.3 - Results of JK Model identified on the dimensionless compressor map corresponding to Figure 7.2.

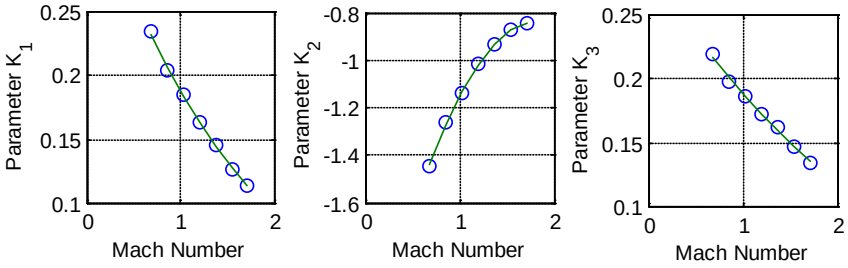

Figure 7.4 - Parameters of JK Model (Data from compressor C1)

Recalling the similarity theory, two compressors that are geometrically, kinematically and dynamically similar should have the same characteristic curves, and should be represented by the same model and relative parameters. In other words, differences in the parameters of the JK models describing two compressors could be attributed to the influence of dimensionless groups formed by corresponding design parameters. It is evident that this theory only leads to approximate results, as several other factors are inevitably neglected. For instance, the effects on the characteristic curves caused by the Reynolds number and other design parameters (such as the blade angles) have been not included in this study. As a starting point for the analysis, Figure 7.5 shows the normalized characteristic curves obtained for 6 different compressors at the same blade Mach number (Ma=1.4), obtained from the JK models calibrated on each compressor.

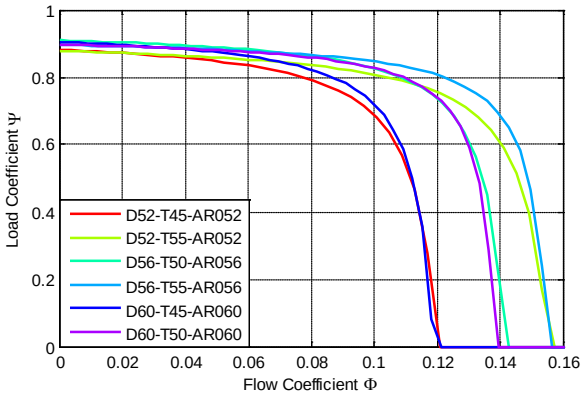

Figure 7.5 - Extrapolated dimensionless flow characteristic curves for 6 different compressors, at constant Mach number

The curves in Figure 7.5 have been extrapolated to the two axes. The trend exhibited by the characteristic curves suggests that two limit conditions could be imposed to the JK model, leading to explicit analytical expressions for the model parameters. At zero flow condition (Φ=0) all of the characteristic curves approximately tend to the same value. This limit behavior could be described as a condition where the work done by the blades is entirely spent to increase the kinetic energy of the volume of fluid contained in the compressor casing, and overcome friction losses. This condition can be represented mathematically through the radial equilibrium theory, based upon the conservation of energy and the Euler equation [51]:

$$c_p T_{ref}\left(\beta^{\frac{\gamma-1}{\gamma}}-1\right)=u_2c_2-u_1c_1-f\frac{c_2^2}{2} \tag{7.6}$$

where c_1 and c_2 are the absolute velocity at the inlet and outlet of the impeller, u_1 and u_2 the corresponding blade speed values, and f is a friction coefficient function of the mean flow velocity. Under zero flow conditions, the velocity of the fluid in the casing is assumed equivalent to the blade speed u_2. Further, the velocity at the inlet of the impeller can be neglected. Introducing the blade-loading coefficient and blade Mach number, Equation (**7.6** results into:

$$\Psi_0\frac{u_2^2}{2}=u_2^2-f(Ma)\frac{u_2^2}{2} \tag{7.7}$$

leading to the following expression that determines the value of the load coefficient at zero flow condition:

$$\Psi_0=2-f(Ma) \tag{7.8}$$

where the parameter f is identified as a linear function of the blade Mach number based upon the data obtained from the JK model extrapolated at zero flow conditions.

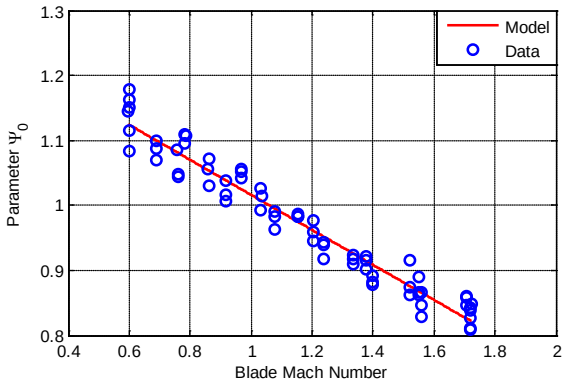

Figure 7.6 - Result of identification of the load coefficient at zero flow condition

Note that the model obtained above is dimensionless, and does not show analytical dependence with any design parameter. Figure 7.6 compares the model described by Equation (**7.8** to the limit condition Ψ_0 calculated from the JK models identified on the 6 compressors models, for different Mach numbers. The model agrees generally well with the data, confirming that the above assumptions constitute a reasonable approximation. Furthermore, the JK model presents a vertical asymptote at $\Phi=K_3$. This property could be exploited to qualitatively describe the behavior of a centrifugal compressor approaching the choking at the inducer. For this limit condition, a mass and energy balance can be formulated to produce an analytical expression for the choking mass flow rate [51]:

$$\dot{m}_{choke} = \rho_1 c_1 A_t \left(\frac{2}{\gamma+1} + \frac{\gamma-1}{\gamma+1}\frac{u_1^2}{c_1^2}\right)^{\frac{\gamma+1}{2(\gamma-1)}} \tag{7.9}$$

where ρ_1 and c_1 are the density and absolute velocity at the inducer, and A_t the corresponding throat area. Applying the dimensional analysis to Equation (**7.9** and introducing the Trim as a design parameter for the impeller, the flow coefficient at the choking condition results as follows:

$$\dot{\Phi}_{choke} = k_1 \frac{T}{Ma}\left(\frac{2}{\gamma+1} + k_2 T Ma^2\right)^{\frac{\gamma+1}{2(\gamma-1)}} \tag{7.10}$$

where T is the compressor Trim and the parameters k_1 and k_2 are identified

from the parameter K_3 (vertical asymptote) of the JK model for the 6 compressors. Note that the above expression contains explicitly the Trim, and should therefore be suitable to describe the choking behavior of different compressors in geometric similarity.

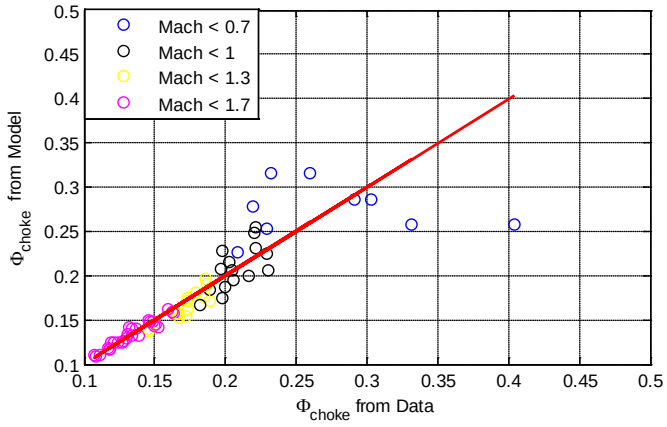

Figure 7.7 - Verification of the φchoke model for various compressors at different values of the blade Mach number

This can be verified by observing the results of the model identification shown in Figure 7.7, where Φ_{choke} is calculated for different Mach numbers and represented against the data for different compressors (characterized by different design parameters). Equation (**7.10** reasonably predicts the choking condition described by the JK model calibrated on the different compressors. In particular, the accuracy of the model is higher for high Mach numbers, namely when the compressor characteristics curves become steeper at high flow rate conditions, validating the assumption that the parameter K_3 in the JK model approximates the choking limit Φ_{choke}. The JK model described by Equations (**7.4**- (**7.5** can be modified by inserting the limit conditions Ψ_0 and Φ_{choke}, resulting into:

$$\Psi = \Psi_0 \frac{1 + p\Phi}{1 - \dfrac{\Phi}{\Phi_{choke}}} \tag{7.11}$$

$$\Psi_0 = \Psi_0(Ma); \quad \Phi_0 = \Phi_0(Ma, T)$$

The above equation modifies the JK model by introducing an explicit dependence of the model parameters on the impeller design features (Trim and diameter). Note that the dependence on the diameter is given by the Mach number, flow and load coefficient definitions, according to Equation (**7.5**. The last parameter p can be calculated based upon the parameters K_1, K_2, K_3 of the original JK model. Note that the JK model parameters must be constrained so that the model correctly predicts the negative slope of the compressor speedlines in the stable operating region. For this to happen, K_1, K_2, K_3 must obey the following condition:

$$K_1 K_3 + K_1 < 0 \tag{7.12}$$

Expressing the above parameters in terms of p, Φ_0 and Φ_{choke} results into:

$$K_3 = \Phi_{choke}; \quad \frac{K_1}{K_3} = \Psi_0; \quad \frac{K_2}{K_1} = p \tag{7.13}$$

And ultimately:

$$p\Phi_{choke} + 1 < 0 \tag{7.14}$$

To facilitate the definition of a tunable parameter, the above constraint can be conveniently expressed as follows:

$$p = -\frac{k}{\Phi_{choke}}; \quad k > 1 \tag{7.15}$$

where k is expressed as a quadratic function of the Mach number, since the presence of Φ_{choke} in Equation (**7.15** indicates that the parameter p is also correlated to the compressor Trim. The final expression of the modified JK model is given by:

$$\Psi = \Psi_0 \frac{1 + k\dfrac{\Phi}{\Phi_{choke}}}{1 - \dfrac{\Phi}{\Phi_{choke}}} \tag{7.16}$$

$$\Psi_0 = \Psi_0(Ma); \quad \Phi_0 = \Phi_0(Ma, T); \quad k = k(Ma)$$

Figure 7.8 shows the identification of the parameter k against the blade Mach number, using data from the six compressors considered in the calibration set.

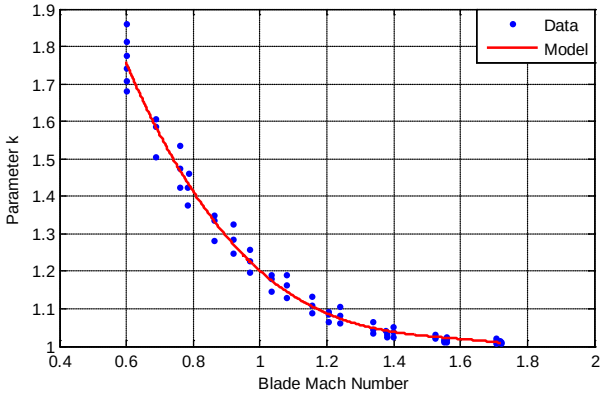

Figure 7.8 - Identification of the parameter k using data from different compressors

Since the above model is formulated analytically and contains explicitly two key design parameters, namely the impeller diameter and Trim, this makes it possible to extend this model to predict the characteristic maps of different compressors, by simply varying the design parameters. Note that the above model does not contain any explicit dependence with the A/R ratio. This is consistent with the behavior of centrifugal compressors, whose performance is comparatively insensitive to changes in the A/R parameter. Figure 7.9 shows compares the prediction of the scalable compressor flow model against the maps of two different compressors included in the calibration data set summarized in Table 7.1- Data of the six compressors used for model calibration Table 7.1. The model requires the diameter and trim as inputs, together with the flow rate and rotational speed of the compressor, and is used to predict the corresponding pressure ratio values

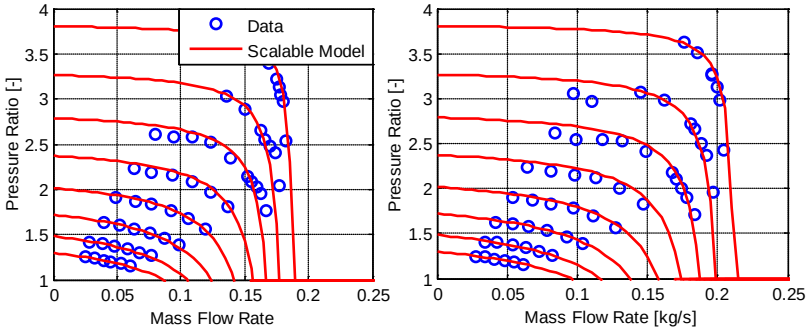

Figure 7.9 - Verification of the scalable compressor flow model against data of two different compressors (left: compressor c2, right: compressor c3).

7.1.2. Compressor efficiency model

Several empirical or semi-empirical models for the compressor efficiency have been proposed in the context of control-oriented modeling of turbocharged engines [56][58][59]. A possible approach to predict this variable hinges upon characterizing its losses [60]:

$$\eta = \frac{\Delta h_s}{\Delta h_s + \Delta h_{loss}} \tag{7.17}$$

where Δh_s is the isentropic enthalpy rise defined as:

$$\Delta h_s = c_p T_{ref} \left(\beta^{\frac{\gamma-1}{\gamma}} - 1 \right) \tag{7.18}$$

and the enthalpy loss Δh_{loss} includes four different terms, namely the incidence and friction losses through the impeller and the diffuser:

$$\Delta h_{loss} = \Delta h_{ii} + \Delta h_{if} + \Delta h_{di} + \Delta h_{df} \tag{7.19}$$

The objective is to express the above losses using semi-empirical correlations, where their dependence on the design parameters of the compressor is made explicit. According to the NASA Shock Loss theory [61], the incidence losses can be expressed by assuming that the kinetic energy associated with the tangential component of the relative velocity wu1 is lost as the fluid adapts to the blade direction. Thus, the energy loss

due to incidence is given by [53]:

$$\Delta h_{ii} = \frac{1}{2}(u_1 - \frac{\dot{m}cot\beta_{1b}}{\rho_1 A_1})^2 \quad (7.20)$$

where A_1 is the area and β_{1b} the blade angle at the impeller inlet.
While the blade angle is normally not readily available (hence its influence must be simplified from the model), the area A_1 can be approximated by introducing the trim and impeller diameter. Expanding Equation (**7.20** and lumping the unknown parameters into calibration coefficients, the incidence losses can be expressed as:

$$\Delta h_{ii} = k_1 TMa^2 + k_2 \frac{\dot{m}Ma}{D_2^2\sqrt{T}} + \frac{\dot{m}^2}{D_2^4 T^2} \quad (7.21)$$

The friction losses through the impeller can be approximated by assuming analogy to losses due to turbulent flow in a pipe [60]:

$$\Delta h_{if} \cong C_{hi} \frac{l}{D_h} \frac{w_1^2}{2} \quad (7.22)$$

where C_h is a friction coefficient (calibration parameter), l the channel length, D_h the hydraulic diameter, and w_1 the relative flow velocity at the inlet of the impeller, which can be approximated as a function of the mass flow rate and blade Mach number. The hydraulic diameter and channel length are approximated as functions of the impeller design parameters as follows:

$$D_h \cong \frac{D_1 + D_2}{2} = \frac{D_2(\sqrt{T} + 1)}{2} \quad (7.23)$$

Since the diffusers for automotive centrifugal compressors are typically vaneless, the corresponding incidence losses can be neglected, while friction losses are accounted for with the following approximated expression:

$$\Delta h_{df} = C_{hd} \frac{\dot{m}^2}{2} \tag{7.24}$$

The above model contains five empirical parameters, namely k_1, k_1, k_3, C_{hi}, C_{hd}, which can be calibrated based on the characteristic curves of a sparse set of compressors. Figure 7.10 shows the calibration of the above parameters based upon the efficiency data of a single compressor, and illustrates their dependence with the Mach number.

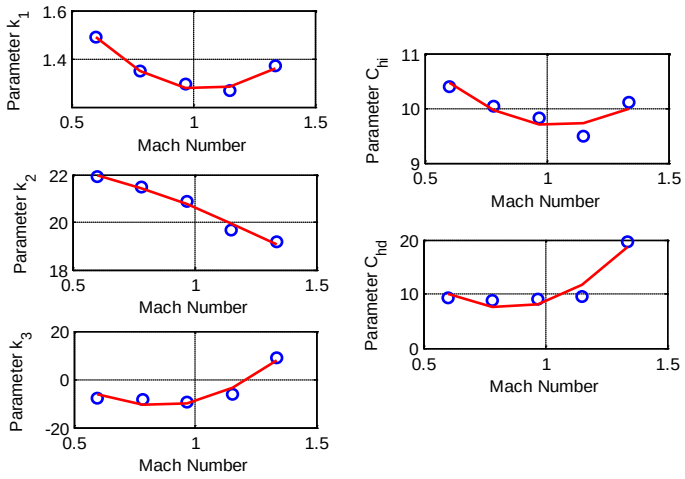

Figure 7.10 - Parameter identification of the efficiency model from data of a single compressor (c5).

While the above model is in principle able to predict the influence of the design parameters, it relies on significant approximations. For this reason, a calibration on a set of different compressor efficiency maps is necessary to improve the predictive ability of this model. In this case, the 6 compressor maps listed in Table 7.1 have been used as a data set for model calibration. First, the efficiency map of each compressor is used to calculate the enthalpy loss, which allows one to identify the parameters k_1, k_1, k_3, C_{hi}, C_{hd} using a simple linear least-square method. Then, the five parameters obtained for the different compressors are approximated as functions of the Mach number and Trim using a simple linear regression model. Figure 7.11 shows the outcome of the identification procedure, and illustrates the agreement of the compressor efficiency model with the data of a single compressor map. Both the enthalpy loss and the isentropic efficiency are

predicted reasonably well by the model in the entire range of available data.

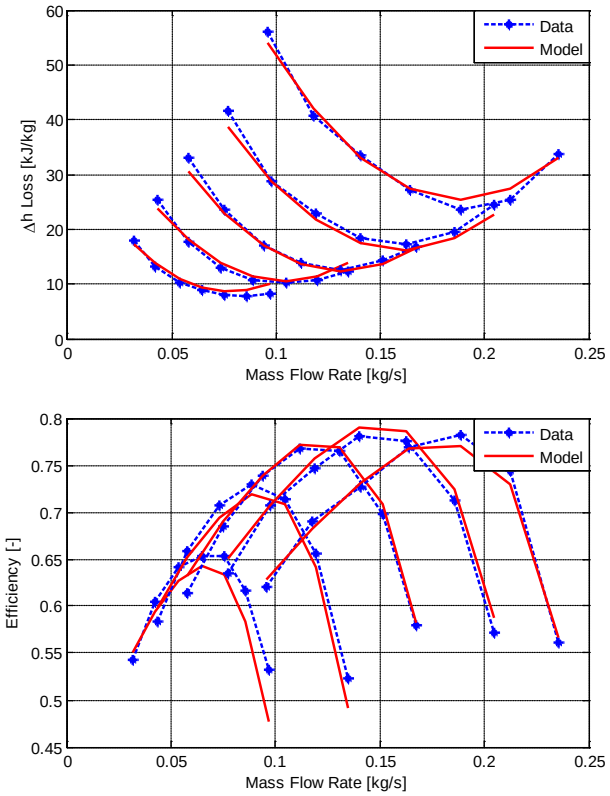

Figure 7.11 - Verification of the scalable compressor efficiency model on the data of one compressor (c5).

7.1.3. Turbine mass flow rate model

The available data set for turbines includes 74 set of flow and efficiency maps, relative to machines from the same family. In order to calibrate parameters of the models described below, 45 turbines have been randomly chosen, and the remaining 29 have been selected for verification.

Table 7.3 – Variation range for the design parameters of the available turbine maps

Diameter	44-50 mm (3 different values)
Trim	67-84 (8 different values)
A/R	0.34-0.88 (13 different values)

The starting point to define the turbine flow model is the modified orifice equation, which is a generally accepted approach for modeling the turbine flow rate [54][56]. Among others, the modified orifice equation presented in [62] exhibits high accuracy in predicting the turbine mass flow rate in a wide range of operating conditions. This model characterizes the turbine flow rate as a non-isentropic expansion process through an orifice, based upon the equation:

$$\dot{m}_{corr} = C_d A \frac{p_{in}}{\sqrt{RT_{in}}} \sqrt{\gamma} f(\varepsilon)$$

$$f(\varepsilon) = \begin{cases} \sqrt{\frac{2}{\gamma - 1}\left(\varepsilon^{\frac{2}{m}} - \varepsilon^{\frac{m+1}{m}}\right)} & if \ \frac{1}{\varepsilon} \geq \left(\frac{2}{m+1}\right)^{\frac{m}{m-1}} \\ \left(\frac{2}{m-1}\right)^{\frac{1}{m-1}} \sqrt{\frac{2}{\gamma - 1}\frac{m-1}{m+1}} & otherwise \end{cases} \quad (7.25)$$

where the polytropic coefficient m and the equivalent area C_dA are tunable parameters, and p_{in}, T_{in} are reference values provided by the manufacturer. Generally, the parameters m and C_dA are directly identified on the turbine flow maps. In this sense, Figure 7.12 shows an example where the parameters of the model described by Equation (**7.25** have been calibrated to match the flow rate data of a specific turbine.

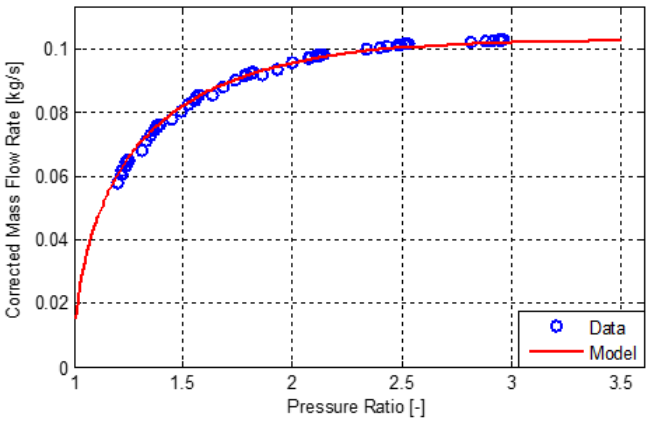

Figure 7.12 - Standard orifice equation applied to a single turbine. Parameters are calculated on turbine data set.

On the other hand, Equation (**7.25** indicates that the two calibration parameters must be determined through a nonlinear least-square fitting, the identification of the parameter *m* could be significantly affected by the choice of initial conditions and constraints. To avoid such problems, the parameter identification is conducted by noting that the polytropic coefficient directly affects the critical pressure ratio:

$$\varepsilon_{crit} = (\frac{2}{m+1})^{\frac{m}{m-1}} \tag{7.26}$$

which represents the limit conditions at which the flow through the turbine reaches sonic speed, resulting into the well-known choking phenomenon. From Equation (**7.26**, the critical pressure ratio can be well approximated as a linear function of the coefficient *m* without loss of accuracy. In this sense, the polytropic coefficient can be interpreted as a scaling factor that linearly influences the choking limit of the turbine. This can be useful to simplify and automate the turbine flow model calibration process. Once the turbine flow model is identified on a specific set of data (in terms of finding constant values for C_dA and ε_{cr}), the next step is to determine how the turbine design parameters affect the two calibration coefficients. The equivalent area C_dA in Equation (**7.25** generally relates to the throat area and the exit area of the turbine. Assuming that geometric similarity holds true, the throat area can be considered proportional to the turbine diameter and the A/R ratio, while the exit area can be assumed proportional to the diameter and Trim. This leads to the following expression:

$$C_dA \cong a_1\left(\frac{A}{R}D\right) + a_2(D^2T) + a_3 \tag{7.27}$$

where the coefficients a_1, a_2, a_3, can be calibrated on maps from turbines of different design.

Since the critical pressure ratio ε_{cr} can not be immediately related with the turbine design, a regression analysis is conducted. Specifically, a set of dimensionless parameters is defined considering different combinations of A/R, Trim and diameter, and their influence on ε_{cr} is evaluated until a statistically representative model is found as follows:

$$\varepsilon_{cr} \cong b_1 \left(\frac{A}{R}\frac{1}{D}\right) + b_2 T \tag{7.28}$$

At this point, the complete model can be explained, wherein Equation (**7.25** the equivalent area C_dA is obtained through Equation (**7.27** and $f(\varepsilon)$ is expressed as function of m, being this term calculated as function of ε_{crit} defined in Equation (**7.28**. Results of the model are shown in Figure 7.13 and Figure 7.14.

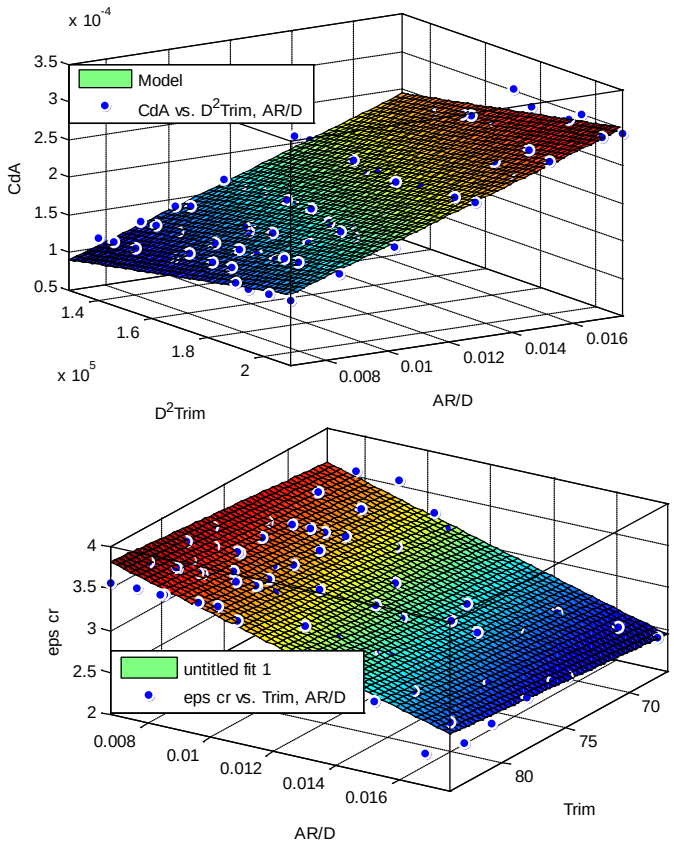

Figure 7.13 - Identification of the parameter C_dA and ε_{cr} using data from different turbines

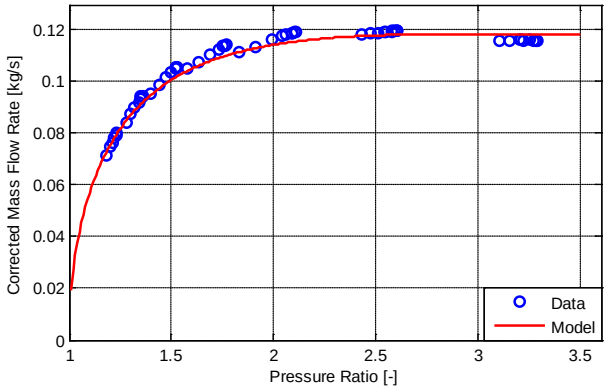

Figure 7.14 - Verification of the scalable turbine mass flow rate model on the data of one turbine (calibration set)

7.1.4. Turbine efficiency model

The turbine efficiency model has been developed starting the approach proposed in [52], which is based on the definition of corrected power:

$$P_{corr} = \eta_t \dot{m} c_p T_{ref} (\varepsilon^{\frac{\gamma-1}{\gamma}} - 1) \tag{7.29}$$

The above equation can be manipulated to obtain a dimensionless expression:

$$P_{corr,dl} = \frac{P_{corr}}{\dot{m} c_p T_{ref}} = \eta_t (\varepsilon^{\frac{\gamma-1}{\gamma}} - 1) \tag{7.30}$$

According to [52], the dimensionless power can be reasonably approximated using a power law:

$$P_{corr,dl} = a(\varepsilon - \varepsilon_0)^b \tag{7.31}$$

where the parameters a, b and ε_0 are generally calibrated based upon the flow and efficiency maps of a given turbine.

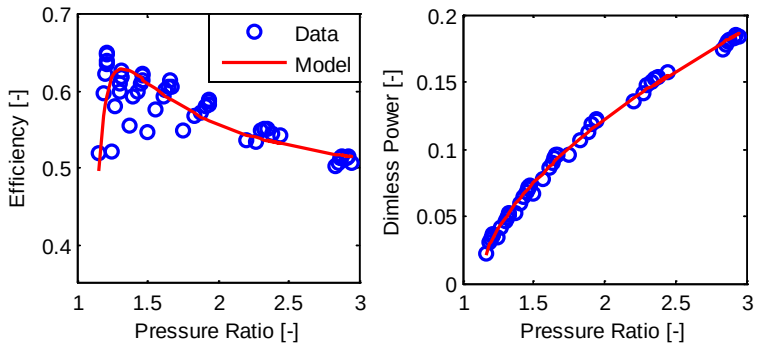

Figure 7.15 - Example of application of turbine efficiency model to the data of a single turbine

Figure 7.15 illustrates an example of how Equation(7.31 can be used to fit turbine data. As can be observed, the dependence of turbine efficiency on the shaft speed is sometimes neglected for simplicity, hence only one curve is used to represent the points on the different speedlines. To make the above model scalable, the tuning parameters are optimized to the data of different turbines using a least-squares method. While the parameter ε_0 does not immediately correlate to the turbine design, it can be expressed as suggested in [52]:

$$\varepsilon_0 = \left[1 + \frac{\gamma - 1}{2\gamma} \frac{1}{RT_{ref}} \left(\frac{\pi}{30}\right)^2 N_0^2 \left(\frac{D_{in}^2 - D_{out}^2}{4}\right)\right]^{\frac{\gamma}{\gamma-1}} \tag{7.32}$$

The above equation can be manipulated to introduce the Trim and a new dimensionless group c:

$$\varepsilon_0 = \left[1 + \frac{\gamma - 1}{2\gamma} c \left(\frac{1 - T}{4}\right)\right]^{\frac{\gamma}{\gamma-1}}$$
$$c = \frac{1}{RT_{ref}} \left(\frac{\pi}{30}\right)^2 N_0^2 D_{in}^2 \tag{7.33}$$

The term c contains a tuning parameter (N_0), which theoretically represents the shaft speed at which the turbine has zero power output. While this

parameter can be calibrated based on data from different turbines, Equation**(**7.33 indicates that there is an explicit dependence of the term ε_0 on the runner diameter and Trim. The remaining parameters in Equation (**7.31** are then correlated to data from turbines of different designs. To understand how a and b influence the expression in Equation (**7.31** in relation to the turbine design parameters, a sensitivity analysis was conducted using the data from the calibration set. This analysis shows that:

- The A/R ratio has a directly influence power curve shape;
- The runner diameter does not have a significant influence on the parameters a and b, while it affects ε_0 as seen above;
- The Trim has different influence on the dimensionless power based upon the value of the other design parameters, with higher sensitivity for larger A/R values.

While the validity of the above statements is obviously limited to the family of turbines considered in this study, it is possible to identify approximated expressions linking the parameters a and b to the turbine design. In particular, the following correlations are found through a linear regression:

$$a = a_1 \frac{A^2}{R^2}\frac{1}{D^2}T + a_2 \frac{A^2}{R^2}\frac{1}{D^2}T^2$$
$$b = b_1 T + b_2 \frac{A}{R}\frac{1}{D}T \tag{7.34}$$

At this point, the whole model can be defined as:

$$P_{corr,dl} = a(\varepsilon - \varepsilon_0)^b$$
$$a = f\left(\frac{A}{R}, D, T\right); \quad b = f\left(\frac{A}{R}, D, T\right); \quad \varepsilon_0 = f(T, c); \quad c = f(T) \tag{7.35}$$

The above model has been calibrated using data from the efficiency maps of 45 different turbine designs, and then applied to predict the efficiency data used in Figure 7.16. The agreement of the scalable model with the data point is shown in Figure 7.17. Note that the scalable model has virtually no differences from the model used in Figure 7.15, which has been specifically calibrated on the data of a single turbine.

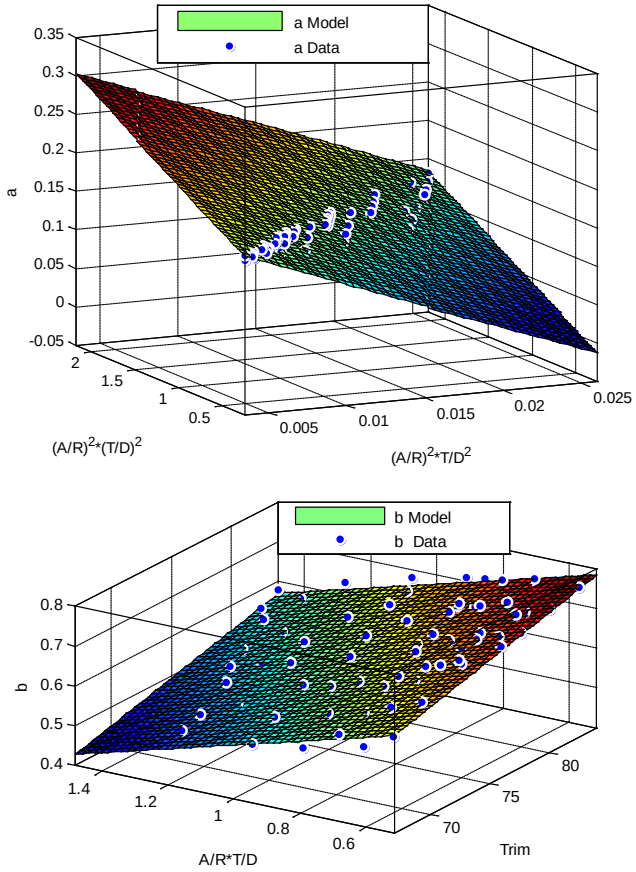

Figure 7.16 - Identification of the parameter *a and b*

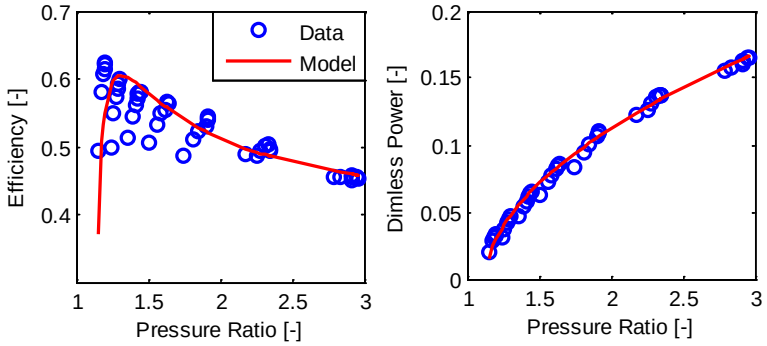

Figure 7.17 - Verification of the scalable turbine efficiency model on turbine data

7.2 Model validation

As previously mentioned, the scalable turbocharger model described above was calibrated using the flow and efficiency maps of several compressors and turbine, namely data from 6 different compressors indicated in Table 7.1 and 45 different turbines chosen among the ones listed in Table 7.3. To verify the ability to predict maps of compressors and turbines of the same family but different design, the model has been applied to another set of data, including the three compressors listed in Table 7.2 and 29 turbine maps among the ones summarized in Table 7.3. Note that these maps have not been previously used to calibrate the model. The compressor model requires the mass flow rate and shaft speed as inputs, together with values of diameter, A/C and Trim. The pressure ratio and efficiency are then predicted by the model. Conversely, the turbine model requires the pressure ratio and design parameters as inputs, and outputs the flow rate and efficiency. Figure 7.18 shows the validation results for the scalable compressor model, where the model has been used to predict the pressure ratio and efficiency of the three compressors whose design data are listed in Table 7.2. Similarly, Figure 7.19 shows the same validation conducted using data from three different turbines. The design data of the compressors and turbines considered in the figures are specified in the captions. It can be observed that the scalable model is able to predict the compressor and turbine behavior quite well. In particular, very good results are obtained for the compressor mass flow rate and efficiency, for which errors below 2% have been obtained on all the tested maps. The analytical form of the compressor flow model, developed by combining dimensional analysis and physical considerations, leads to a high fidelity, and ability to extrapolate the system behavior to compressors of different designs. Although the compressor efficiency model is only in part defined analytically, the analysis shows a good agreement as well, particularly for low speed conditions.

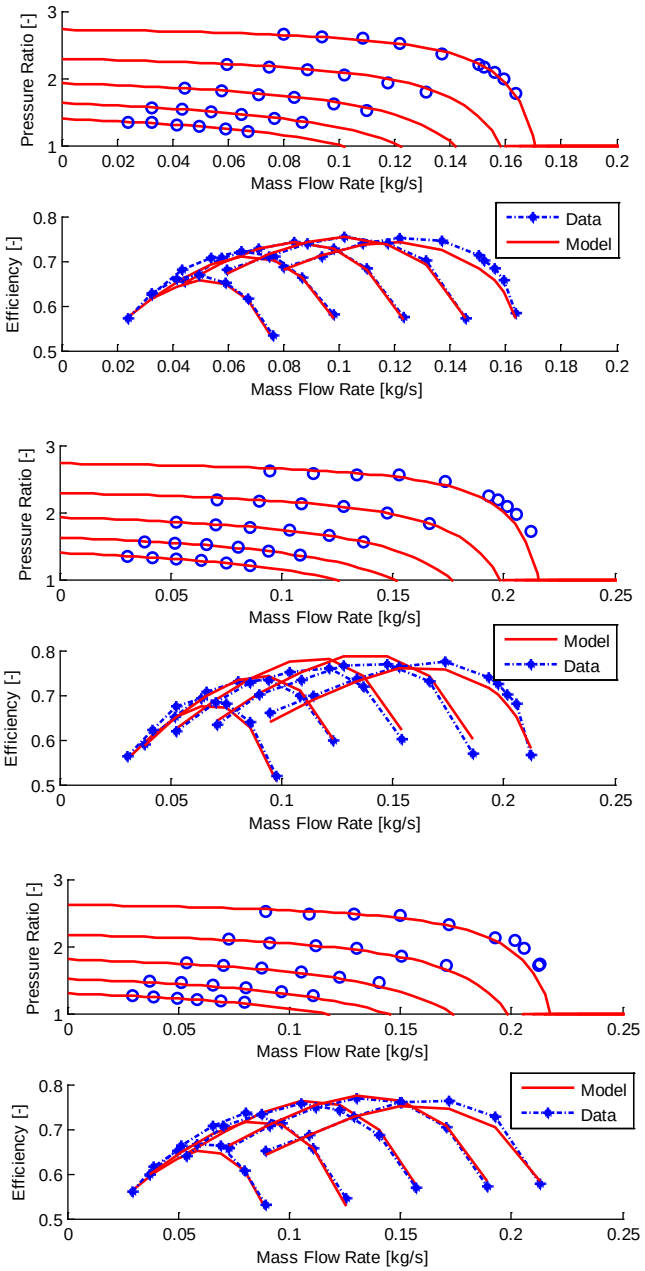

Figure 7.18 - Validation of the scalable compressor model on the data of three different compressors not used for calibration (Top: D=56, A/R=0.45, TRIM=56; Middle: D=56, A/R=0.55, TRIM=56; Bottom: D=60, A/R=0.50, TRIM=60).

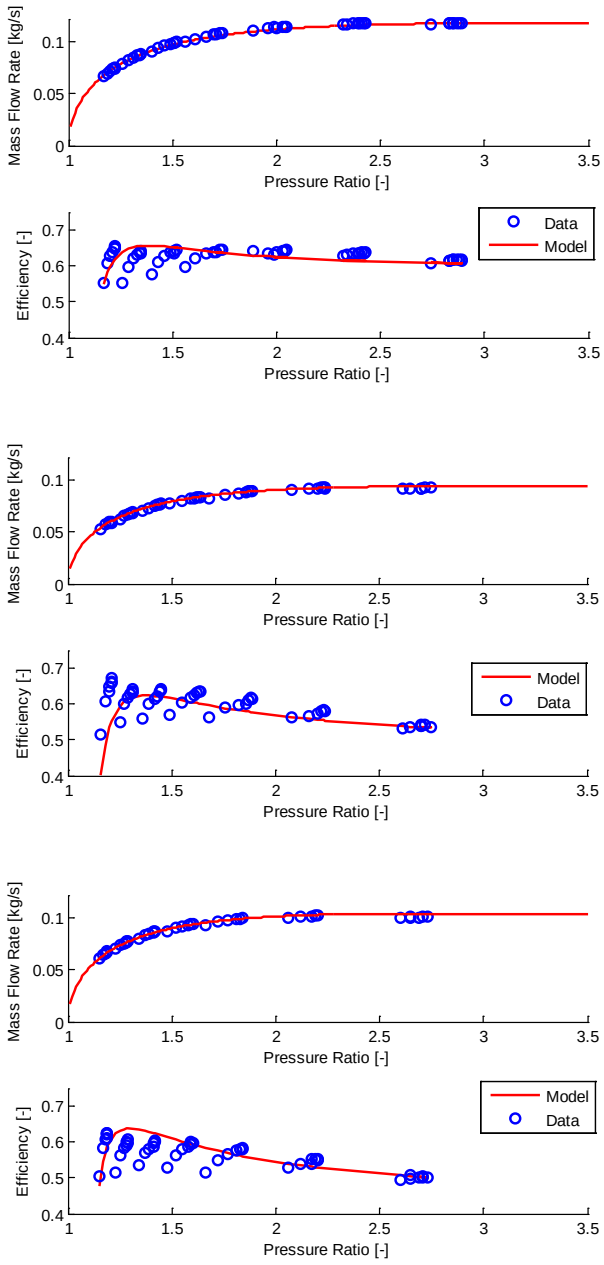

Figure 7.19 - Validation of the Scalable Turbine Model on the Data of Three Different Turbines Not Used for Calibration (Top: D=50, A/R=0.64, TRIM=84; Middle: D=44, A/R=0.62, TRIM=74; Bottom: D=44, A/R=0.76, TRIM=80).

Similarly, the turbine mass flow rate model shows good agreement with the data in the three cases considered, although the parameters relating the model to the turbine design have not been derived from physical considerations, but rather dimensional analysis and data regression. On the other hand, the turbine efficiency model performs less reliably due to the approximation of considering only one power curve to interpolate the behavior of the different speedlines, hence neglecting the effect of the shaft speed. As a further verification of the model capabilities, a sensitivity analysis has been conducted to illustrate how the impeller diameter and Trim influence the shape of the characteristic maps of the compressor. The flow and efficiency maps are represented for shaft speed ranging from 40,000rpm to 90,000rpm at intervals of 10,000rpm.

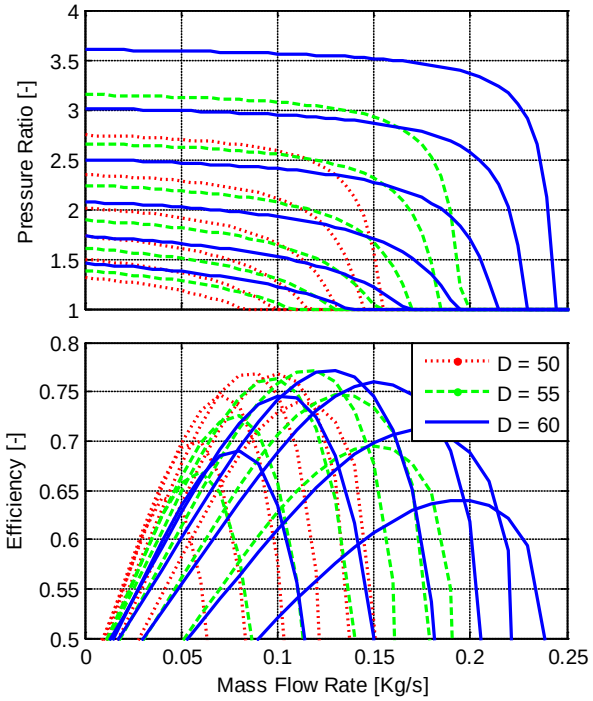

Figure 7.20 - Influence of impeller diameter on compressor flow and efficiency maps (trim=50).

The influence on the impeller diameter on the compressor flow rate is evident from the dimensionless expression of the JK model, shown in Equations (**7.4**-(**7.5**). Decreasing the diameter affects the blade Mach

number (for a given shaft speed), causing a quadratic reduction of the limit pressure ratio at zero flow condition. At the same time, the choking limit decreases significantly, hence reducing the stable operating region of the compressor. For a small reduction of the impeller diameter, the efficiency curves tend to shift towards lower flow rate conditions, while the peak efficiency values do not change significantly. It is well known that the impeller Trim has a significant influence on the compressor performance by shifting the airflow capacity. This effect is correctly captured by the scalable model through the choking limit, which depends on the cross-sectional area of the inducer. This effect is shown in Figure 7.21. Conversely, the model shows that the Trim does not influence significantly the characteristic curves at low flow rate conditions, which is consistent with the fact that the pressure ratio is generally limited by the blade stall phenomenon. Unlike the impeller diameter, the Trim has an evident effect on the peak efficiency values, due to the marked influence of this parameter on the impeller incidence losses. Furthermore, the Trim influences the flow rate condition at which the peak efficiency is reached for each speedline.

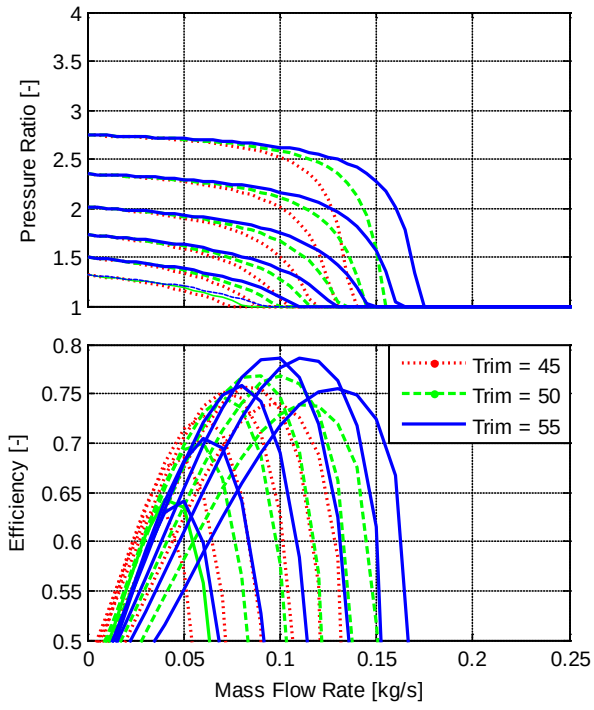

Figure 7.21 - Influence of trim on compressor flow and efficiency maps (d=50).

Conclusions

By now, it is evident the need to differently exploit the available energy sources and reduce the oil use; this is a problem that can no longer be avoided. The current transport system is deeply linked to fossil fuels and considering the continuous increase in vehicle registrations and economic development of other countries, in a few decades the CO_2 emissions and environment pollution could reach intolerable levels. On this scenario, the sales of hybrid vehicles gain strength as a solution in a short to medium term for road transport. However, the cost of a hybrid vehicle is high compared to that of conventional vehicles and not all companies are willing to convert their production plant or invest on hybrid technology before it will occupy a significant share of the market; The HYSOLARKIT project tries to work around these problems.

Upgrading conventional vehicles to mild-solar-hybrid could have a relevant and short-term impact on fuel consumption and carbon dioxide emissions due to transportation, since it may potentially be applied to most of the today fleet, and without requiring expensive reconversion of production lines for cars. A prototype of the hybridization kit has been developed and installed on a FIAT Grande Punto at the University of Salerno demonstrating the feasibility of the project. Anyway, the benefits in terms of fuel savings are lower than on a native hybrid, due to the constraints posed by the TTR structure, and to the absence of downsizing effects. In this regard, the contribution of photovoltaic source is significant. However, the comparison with the original vehicle is somewhat misleading, since the addition of two wheel motors significantly enhances vehicle power and performance, in particular acceleration. Moreover, the presence of two additional propulsion devices offers interesting potentialities in terms of driveability, due to the possibility to adopt advanced vehicle control schemes. The prototype represents a successful proof-of-concept, having allowed to test and to verify possible critical issues related to in wheel motors, battery, photovoltaic panels and control system.

Different methodologies have been used to address on-line energy management of the proposed hybridization kit, as well as offline investigation of maximum fuel economy: fuzzy logic, for instance, has been adopted to detect driver intention facing the complex interaction

between the driver and vehicle management unit. A set of mathematical models for the Driver Intention, utilizing only data measured from OBD gate, has been developed. The experimental validation, performed over different sets of data measured on the prototype has demonstrated the models capability in properly detecting different driving conditions, also overcoming some problems related to data accuracy, and in defining the correct decision for torque deliver in rear wheel motors. The models, integrated in a fuzzy set of rules, are able, for instance, to detect the active gear and to identify the gearshift or null gear conditions. The active gear and engagement conditions represent important additional variables to identify the Driver Intention on a vehicle with manual gearbox and the real-time detection of active gear plays therefore an important role for the control of a hybridized vehicle. A mathematical model for the identification of active gear, utilizing only data measured on OBD port, has been developed. A suitable mix of filtering algorithms and rules has allowed overcoming the problems due to uncertainty and discretization error in OBD velocity data. Moreover, a study on the effects of the actuation delays has been performed, in order to check the drivability degradation due to different design and control solutions. A simulation with a forward longitudinal vehicle dynamic model, including driver behaviour, has analysed the effects played by the delays of actuation in the main control loop, related to the frequency of data acquisition from OBD or from CAN bus, and by the delays associated to electrical and mechanical response of the wheel motors. It has been evidenced that these delays have little effects on drivability until 0.2 s, and that the delay on VMU is more critical. The study of combined effects has also shown that delays tend to offset each other, and that for realistic values of the delays the increase in the irregularity index with respect to the ideal case is very limited. Extensive road tests have evidenced the absence of critical issues in terms of drivability for the currently used hardware, so confirming the outcomes of the simulation model.

The implemented control strategies with a constant power split have shown an important fuel and cost savings on urban cycles of 20% roughly. The most important part of these results is obtained because of energy harvested from solar panels and recovered during braking phases. A model able to estimate the vehicle braking torque, considering aerodynamics, vehicle friction and engine passive losses in different gears, has been developed and identified over road tests, for the hybridized vehicle. The model has

been used to analyse different braking strategies, with and without mechanical brakes on rear wheels, in order to maximize the recovered energy by wheel motors and to prevent slipping conditions. Preliminary results have shown the model being a useful tool to design real-time braking strategies if properly combined with estimation of slipping coefficient and use of ABS systems. On the other hand, an advanced dynamic programming optimization tool has been also used to evaluate the potential offered by the proposed hybridizing kit, and to providing a useful fuel savings benchmark. Dynamic Programming results will be used as guidelines to improve implementable control strategies object of future works.

The opportunity of collecting data via OBD port to monitor real-world performance of engine and vehicle in order to make the hybridization kit work together with the original vehicle control system has led to the development of a model for the implementation of predictive maintenance strategies, which constitutes an additional value to the project and kit desirability. A methodology for the definition of check times for six different vehicle subsystems (brakes, engine, limber, gearbox, clutch, and cooling system) has been developed. The methodology is based on the calculation of some stress indexes starting from elaboration of OBD data through the longitudinal dynamics model of the vehicle. The stress indexes are then correlated to the risk factors via a correlation matrix whose values can be upgraded by an adaptive methodology based on components wear registered during maintenance operations. The estimated time for vehicle maintenance and its variability around a mean value, is carried out using recursive estimation techniques through the comparison between the actual risk factor for the vehicle and those calculated for a standard vehicle type, operating on a reference driving cycle, for which manufacturer indication in terms of maintenance are assumed the same as stated.

Finally, in order to optimize the design and control of turbocharged systems, which represent the most effective alternative to hybrid vehicles for fuel consumption and cost reduction, a model-based methodology to predict the characteristic maps of a family of compressors and turbines as functions of their most common design parameters, namely the diameter, Trim and A/R ratio has been developed. Starting from the basic theory of dimensional analysis for turbomachinery and a set of well-known analytical models for turbocharger control applications, an analysis has been conducted to elucidate how the key design parameters of the rotor

influence the flow and efficiency performance of compressors and turbines. The analysis has been developed by combining analytical and data-driven methods, based upon experimental data obtained from a family of centrifugal compressor and radial inflow turbines. A scalable modeling approach has been then developed to correlate the key design parameters of compressors and turbines to the parameters of the flow and efficiency models. The scalable model, validated on a large database of automotive turbochargers, showing the ability to correctly predict the characteristic curves of compressors and turbines when imposing input and design parameters, makes it possible to predict the flow and efficiency maps of compressors and turbines by specifying their key design parameters (diameter, Trim, A/R). To ensure physical consistency and validity, the models require a relatively simple calibration process that relies only on a few sample characteristic maps.

Further works are still needed, anyway, the developed hybrid prototype and its control system have demonstrated, through simulations and on road tests, to guarantee a reasonable payback times and a considerable energy saving. Because of these reasons, the hybridization kit configures itself as a better alternative to other non conventional propulsion systems (see LPG or natural gas systems) that found their convenience only on the lower fuel price compared to diesel or gasoline. Some problems still need to be fixed like integrating the IWM with the vehicle braking system or receive the authority approval, however, who has been working on the project and well know its potential is confident a solution will be found by time. On the other hand, the proposed scalable modeling approach constitutes a powerful tool enabling the opportunity to conduct virtual design studies, using a simulation environment to rapidly evaluate the influence of different compressor and turbine sizes on the performance of a turbocharged engine air path system, and optimize the charging system in a fast and cost effective way.

To conclude, the author of this PhD thesis hopes his work could serve as a useful resource to researchers who work on hybrid vehicles and turbocharged systems and may be another step, however small, towards the Earth, environment and life quality care that should always be our unavoidable duty.

Acknowledgements

Thanks to my friends, my colleagues and my professors who have helped me to improve my knowledge and myself.
I am also grateful to people who gave me the possibility to study in the US and those who lived with me thousands adventures during that period.
Thanks to my parents for their true and priceless support and thanks to my brother and sister, I feel very proud of you.
Thanks to myself for never give it up also when everything was going wrong, this makes this work, for me, the proof of my strength.
Finally and most importantly, thanks to you, Carmen, this thesis is for you, for being always close to me despite everything has happened during these years…I will never forget!

Publications

1. G Rizzo, C Pisanti, M D'Agostino, M Naddeo (2013). "Driver Intention Analysis for a Through-the Road Solar Hybridized Car" In: ICE2013-11th International Conference on Engines & Vehicles, Capri (Italy), September 15-19, 2013

2. I Arsie, M D'agostino, M Naddeo, G Rizzo, M Sorrentino, "Toward the Development of a Through-The-Road Solar Hybridized Vehicle" In: 7th IFAC Symposium on Advances in Automotive Control, September 4-7, 2013, National Olympics Memorial Youth Center, Tokyo.

3. G Rizzo, V Marano, C Pisanti, M D'Agostino, M Naddeo, M Sorrentino, I Arsie (2013). "A Prototype Mild-Solar Hybridization Kit: Design and Challenges". In: 68th Conference of the Italian Thermal Machines Engineering Association, ATI2013, September 11-13, 2013, Bologna (Italy)

4. G. Rizzo, D'Agostino, M. Naddeo (2014). "Development and validation of a model to detect active gear via OBD data for a Through-the Road Hybrid Electric Vehicle" In: IFAC world congress, August 2014, Cape Town.

5. G Rizzo, V Marano, C Pisanti, M D'Agostino, M Naddeo, I Arsie (2014). "Analysis of actuation delay in control system of hybridized vehicle" In: ATI 2014

6. M Naddeo, Y Liu, J Zhou, M Canova (2015). " A Scalable Modeling Approach for the Simulation and Design Optimization of Automotive Turbochargers". SAE International Journal of Engines 8, no. 4, 12

7. M Grandone, M Naddeo, D Marra, G.Rizzo (2016) "Development of a regenerative braking control strategy for hybridized solar vehicle" In: IFAC AAC 2016

References

[1] C. C. Chan , “The state of the art of electric and hybrid vehicles.” Proceedings of the IEEE, 90, 2, 2002

[2] Sciarretta, A., Guzzella, L. (2007). Control of Hybrid Electric Vehicles. IEEE Control Systems Magazine, Vol. 27, No. 2, pp. 60-70.

[3] C. Samaras et al., “Life Cycle Assessment of Greenhouse Gas Emissions from Plug-in Hybrid Vehicles: Implications for Policy.” Environmental science & technology, 42, 9, 3170 - 3176, 2008

[4] European Commission – Climate Action, online http://ec.europa.eu/clima/policies/transport/vehicles/index_en.htm

[5] Wakefield, E. H. (1998), History of the electric automobile: Hybrid electric vehicles, Society of Automotive Engineers.

[6] Trummel, M. and Burke, A. (1983), ‘Development history of the hybrid test vehicle’, Vehicular Technology, IEEE Transactions on 32(1), 7 – 14

[7] Donitz, C., Vasile, I., Onder, C. and Guzzella, L. (2009), ‘Modelling and optimizsing two and four stroke hybrid pneumatic engines’, Proceedings of the Institution of Mechanical Engineers, Part D 223(2), 255–280.

[8] Arsie, I., Rizzo, G. and Sorrentino, M. (2006), ‘Optimal design and dynamic simulation of a hybrid solar vehicle, in ‘SAE World Congress’. 2006-01-2997.

[9] Ambuhl, D., Sciarretta, A., Onder, C., Guzzella, L., Sterzing, S., Mann, K., Kraft, D., K¨usell, M.: A causal operation strategy for hybrid electric vehicles based on optimal control theory. In: Proc. of the 4th Braunschweig Symposium on Hybrid Vehicles and Energy Management, Braunschweig, Germany (2007)

[10] I. Arsie, M. Cacciato, G. Petrone, G. Rizzo, A. Senatore, M. Sorrentino, G. Spagnuolo, " Development of a Prototype of Hybrid Solar Vehicle". (n.d.).

[11] Christensen, L. (2014). Designing In-Hub Brushless Motors. Machine Design.

[12] Anderson, M., & Harty, D. (2010). Unsprung Mass with InWheel

Motors, Myths and Realities. 10th International Symposium on Advanced Vehicle Control.

[13] Ballon, Massie Santos (14 October 2008). "Electrovaya, Tata Motors to make electric Indica"

[14] M. D'Agostino Master thesis, 'Studio e verifica funzionale e strutturale di ruote motorizzate per un sistema di ibridizzazione di autoveicoli'.

[15] Terrell Croft and Wilford Summers (ed), American Electricans' Handbook, Eleventh Edition, McGraw Hill, New York (1987) ISBN 0-07-013932-6 page 7-124

[16] Seyedmahmoudian, Mohammadmehdi; Mekhilef, Saad; Rahmani, Rasoul; Yusof, Rubiyah; Shojaei, Ali Asghar (2014-03-01). "Maximum power point tracking of partial shaded photovoltaic array using an evolutionary algorithm: A particle swarm optimization technique". Journal of Renewable and Sustainable Energy .

[17] Rajesh Rajamani (2012), "Vehicle Dynamics and Control", Springer, Second Edition.

[18] Guzzella, L., & Sciarretta, A. (2013), "Vehicle Propulsion System", Springer.

[19] White, & Korst. (1972). The determination of vehicle drag contributions from coast-down tests. SAE Papers.

[20] Novák, V., Perfilieva, I. and Močkoř, J. (1999) Mathematical principles of fuzzy logic Dodrecht: Kluwer Academic.

[21] Ahlawat, Nishant, Ashu Gautam, and Nidhi Sharma (International Research Publications House 2014) "Use of Logic Gates to Make Edge Avoider Robot." International Journal of Information & Computation Technology (Volume 4, Issue 6; page 630)

[22] Arsie I., Filippella F., Pianese C., Rizzo G., (2000), "A Model for Vehicle Dynamic Simulation with PID and Fuzzy Logic Drive Controllers", Symposium on Advanced Vehicle Control, AVEC 2000, Ann Arbor (MI), USA, August, 2000.

[23] K.Tanaka, "An Introduction to Fuzzy Logic for Practical Application", Springer, 1991.

[24] Allen R.W. et al., "Modeling and Simulation of Driver/Vehicle Interaction", SAE paperNo. 960177, 1996.

[25] Rosen, C. (1974), 'Hybrid powertrain', United States Patent 3791473

[26] Bose, B. K., Somuah, C. B. and Sutherland, H. A. (1984), 'A microcomputerbased propulsion control system of a hybrid electric vehicle', IEEE Transactions on Industrial Electronics IE-31(1), 61 –68.

[27] Drozdz, P. and Yip, D. (1999), 'Control system for a hybrid vehicle', United States Patent 5898282.

[28] Kawakatsu, S. and Honda, S. (1983), 'Control apparatus and method for engine/electric hybrid vehicle', United States Patent 4407132.

[29] Buntin, D. and Howze, J. (1995), A switching logic controller for a hybrid electric/ice vehicle, in 'American Control Conference', pp. 1169 –1175.

[30] Jalil, N., Kheir, N. and Salman, M. (1997), Rule-based energy management strategy for a series hybrid vehicle, in 'American Control Conference', pp. 689–693.

[31] Adhikari, S., Halgamuge, S. and Watson, H. (2010), 'An online powerbalancing strategy for a parallel hybrid electric vehicle assisted by an integrated starter generator', IEEE Transactions on Vehicular Technology 59(6), 2689–2699.

[32] Hochgraf,C., Ryan, M.and Weigman,H.(1996), "Engine control strategy for a series hybrid electric vehicle incorporating load-leveling and computer controlled management", in 'SAE International Congress & Exposition'. 960230.

[33] Baumann,B.,Washington,G.,Glenn,B.andRizzoni,G.(2000),'Mech atronic design and control of hybrid electric vehicles',IEEE/ASME Transactions on Mechatronics 5(1), 58–72.

[34] Schouten,N.,Salman,M.andKheir,N.(2002),'Fuzzy logic control for parallel hybrid vehicles', IEEE Transactions on Control Systems Technology 10, 460– 468.

[35] Rajagopalan, A., Washington, G., Rizzoni, G. and Guezennec, Y. (2003), 'Development of fuzzy logic and neural network control and advanced emission modelling for parallel hybrid vehicles', NREL Technical Report. NREL/SR540-32919.

[36] Dorri, M. and Shamekhi, A. (2011), Design of an optimal control

strategy in a parallel hybrid vehicle in order to simultaneously reduce fuel consumption and emissions, in 'SAE World Congress'. 2011-01-0894.

[37] Paganelli,G.,Delprat,S.,Guerra,T.,Rimaux,J.andSantin,J.(2002),Eq uivalent consumption minimization strategy for parallel hybrid powertrains, in 'Vehicular Technology Coference', pp. 2076–2081.

[38] Sciarretta, A., Back, M. and Guzzella, L. (2004), 'Optimal control of parallel hybrid electric vehicles', IEEE Transactions on Control Systems Technology 12(3), 352–363

[39] Pisu, P. and Rizzoni, G. (2007), 'A comparative study of supervisory control strategies for hybrid electric vehicles', IEEE Transactions on Control Systems Technology 15(3), 506–518.

[40] Ambuhl, D. and Guzzella, L. (2009), 'Predictive reference signal generator for hybrid electric vehicles', IEEE Transactions on Vehicular Technology 58(9), 4730–4740.

[41] Maciejowski, J. (2000), Predictive Control with Constraints, Prentice Hall.

[42] Jeon, S., Kim, K., Jo, S. and Lee, J. (2001), "Driving simulation of a parallel hybrid electric vehicle using receding horizon control", in IEEE International Symposium on Industrial Electronics, pp. 1180–1185.

[43] Markel, T., Brooker, A., Hendricks, T., Johnson, V., Kelly, K., Kramer, B., OąŕKeefe, M., Sprik, S. and Wipke, K. (2002), 'ADVISOR: a systems analysis tool for advanced vehicle modeling', Journal of Power Sources 110.

[44] Bellman, R.E.: Dynamic programming. Princeton University Press, Princeton (1957)

[45] Bertsekas, D.P.: Dynamic programming and optimal control. Athena Scientific, Nashua NH (2007)

[46] Sundstrom O. and Guzzella L., A Generic Dynamic Programming Matlab Function, 18th IEEE International Conference on Control Applications, Saint Petersburg, Russia, July 8-10, 2009

[47] C. Hoder, J. Gover, "Optimizing the hybridization factor for a parallel hybrid electric small car"

[48] Guiggiani, M. (1998). *Dinamica del veicolo*. Torino: CittàStudiEdizioni.

[49] T. Hastie, R. Tibshirani, J. Friedman, “The Elements of Statistical Learning: Data Mining, Inference, and Prediction”, Second Edition (Springer Series in Statistics) 2nd ed. 2009. Corr. 7th printing 2013 Edition

[50] Budugur Lakshminarayana, “Fluid dynamics and heat transfer of turbomachinery”

[51] S. A. Korpela, “Principles of Turbomachinery”

[52] M. Canova: “A Development and Validation of a Control-Oriented Library for the Simulation of Automotive Engines”, International Journal of Engine Research, Vol. 5, No. 3, 2004.

[53] M. Taburri, F. Chiara, M. Canova, Y. Y. Wang, “A Model-Based Methodology to Predict the Compressor Behavior for the Simulation of Turbocharged Engines”,

[54] L. Eriksson, “Modeling and Control of Turbocharged SI and DI Engines,” Oil Gas Sci. Technol., vol. 62, pp. 523–538, 2007.

[55] M. Canova, P. Fiorani, A. Gambarotta, and M. Tonetti, “A Real-time Model of a Small Turbocharged Multijet Diesel Engine : Application and Validation,” SAE Tech. Pap. 2005-24-065, 2005.

[56] P. Moraal, I. Kolmanovsky, “Turbocharger Modeling for Automotive Control Applications”. International Congress and Exposition Detroit, Michigan March 1-4, 1999

[57] Jensen, J., Kristensen, A., Sorenson, S., Houbak, N. et al., "Mean Value Modeling of a Small Turbocharged Diesel Engine," SAE Technical Paper 910070, 1991

[58] K. Stricker, L. Kocher, and G. Shaver, “Turbocharger Map Reduction for Control-Oriented Modeling,” in Proceedings of the ASME 2011 Dynamic Systems and Control Conference, 2011.

[59] G. Martin, V. Talon, P. Higelin, A. Charlet, and C. Caillol, “Implementing Turbomachinery Physics into Data Map-Based Turbocharger Models,” SAE Int. J. Engines, vol. 2, no. 1, pp. 211–229, 2009.

[60] J. T. Gravdahal, O. Egeland, “Centrifugal Compressor Surge and Speed ontrol”. IEEE Transactions on Control System Technology, 5-September 1999

[61] N. Watson, M. S. Janota, “turbocharging the Internal Combustion Engine”.

[62] M. Canova, S.M. Mohler, Y. Guezennec, G. Rizzoni, “Mean Value Modeling and Analysis of HCCI Diesel Engines With External Mixture Formation”, Journal of Dynamic Systems Measurement and Control-transactions of The Asme - J DYN SYST MEAS CONTR 01/2009; 131(1). DOI: 10.1115/1.2977465